

Structural Health Monitoring Strategies Using Traditional Sensors and Computer Vision

By

© 2020

Abdulaziz Almarshad
M.S., The University of Kansas, 2017
B.S., Qassim University, 2012

Submitted to the graduate degree program in Civil Engineering and the Graduate Faculty of The University of Kansas in partial fulfillment of the requirements for the degree of Doctor of Philosophy in Civil Engineering.

Chair: Prof. Jian Li

Co-Chair: Prof. Andrés Lepage

Prof. Rémy Lequesne

Prof. William N. Collins

Prof. Guanghui Wang

Date Defended: October 23, 2020

The dissertation committee for Abdulaziz Almarshad certifies that
this is the approved version of the following thesis:

Structural Health Monitoring Strategies Using Traditional Sensors and Computer Vision

Chair: Prof. Jian Li

Co-Chair: Prof. Andrés Lepage

Date Approved: October 23, 2020

Abstract

The vibration-based condition assessment of structures is the predominant method in structural health monitoring. The condition assessment of structures can be determined through the response of structures (i.e., peak displacement and acceleration), or through change characterization (i.e., system and damage identification). This dissertation presents three improved strategies for structural health monitoring using traditional sensors and computer vision. One strategy uses data fusion of acceleration and strain to estimate the displacement of building structures subjected to nonstationary wind load. In particular, this study presents two methods (data fusion A and B) that can accurately estimate both components of the displacement—the pseudo-static and the dynamic components. The two methods are validated numerically using a 20-story structure and experimentally using a small-scale 6-story structure. The second strategy is based on a computer vision method for system identification using consumer-level cameras and small structural motions. The Kanade-Lucas-Tomasi (KLT) and the Phase-Based Motion Processing (PBMP) methods are adopted in the proposed method. The method is validated experimentally using two small-scale steel structures: a 6-story building and a single-span truss bridge. The third strategy relies on the use of computer vision in damage identification by means of the Damage Locating Vector (DLV) method. This study also investigated the impact of using aliased modes in damage identification. The small-scale truss bridge was used for numerical and experimental evaluations of computer vision in system and damage identifications.

Acknowledgments

First, I should express my great appreciation and thanks to my advisor, Prof. Jian Li, for his support and advice while completing my Ph.D. degree. Dr. Li has been a great mentor for me to advance my knowledge. His high skills and knowledge have helped me in developing my research and academic skills. I am grateful to have him as a mentor during the completion of this research.

My profound thanks should also be extended to my co-advisor, Prof. Andrés Lepage, for his great support. Dr. Lepage has been directing me to the most powerful source of knowledge. His experience has helped me in developing my research and academic skills. It is my pleasure to have him as a mentor while working on my degree.

I also want to thank my committee members Prof. Rémy Lequesne, Prof. William Collins, and Prof. Guanghui Wang. I am glad to have them on my committee, and I appreciate their time and helpful feedback.

I must express my gratitude and my love to my family: my parents Marshad and Fatimah, my wife Areej, and my sibling Ziad. Without their help and love, this work would not be completed. Thank you for standing with me during the past years. My lovely daughters Holall, Rouwd, and Rouwh, have been the joy of my life.

I also want to express my appreciation to my sponsor Qassim University. Their support and funding are highly acknowledged. Thank you for providing me the chance to complete my degree.

I should also thank all the CEAE laboratories staff, especially Kent Dye and David Woody, for their help in the experimental part of this research.

Table of Contents

CHAPTER 1:	Introduction	1
CHAPTER 2:	Background And Literature Review	5
2.1.	Displacement estimation methods.....	5
2.1.1.	Acceleration-based methods	5
2.1.2.	Strain-based methods	10
2.1.3.	Data fusion methods	12
2.2.	System identification.....	13
2.3.	Computer vision methods.....	14
2.4.	Damage identification	19
2.5.	Summary	20
CHAPTER 3:	Displacement Estimation Using Traditional Sensors	22
3.1.	Introduction and background	22
3.2.	Methodology	23
3.2.1.	Data fusion method A	23
3.2.2.	Data fusion method B	25
3.3.	Numerical investigation	26
3.3.1.	Model description (20-story building structure).....	26
3.3.2.	Wind load simulation.....	28
3.3.3.	Numerical results	29

3.4.	Experimental investigation.....	31
3.4.1.	Model description and test setup (small-scale 6-story structure).....	31
3.4.2.	Experimental results.....	33
3.5.	Summary	37
CHAPTER 4:	System Identification Using Computer Vision.....	38
4.1.	Introduction and Background.....	38
4.1.1.	Traditional sensors vs. computer vision.....	39
4.2.	Methodology	40
4.2.1.	Kanade-Lucas-Tomasi (KLT) feature tracker	41
4.2.2.	Phase-based video motion processing (PBMP) method	42
4.2.3.	Proposed framework	44
4.3.	Experimental Investigation	50
4.3.1.	Small-scale 6-story structure.....	51
4.3.2.	Experimental truss bridge	65
4.4.	Summary	78
CHAPTER 5:	Damage Identification Using Computer Vision	79
5.1.	Introduction and background	79
5.2.	Methodology	81
5.2.1.	Motivation of Flexibility-based methods.....	81
5.2.2.	Damage locating vector (DLV) method	82

5.2.3.	Framework	83
5.3.	Numerical investigation	85
5.3.1.	Model description and damage simulation	85
5.3.2.	Numerical results	88
5.3.3.	Practical challenge: temporal-aliasing for computer vision.....	99
5.4.	Experimental investigation.....	103
5.4.1.	Model description and test setup.....	103
5.4.2.	Experimental results.....	104
5.5.	Summary	111
CHAPTER 6:	Conclusions And Future Studies	113
6.1.	Conclusions	113
6.2.	Future Studies.....	115
REFERENCES.....		117

List of Figures

Figure 1: Typical X-direction elevation and floor plan of the 20-story building structure	27
Figure 2: Generated wind load forces profile for the SAP2000 model	28
Figure 3: Comparison of building drift estimates using various methods: (a) Full record (b) Partial record	30
Figure 4: Front and side view of the small-scale 6-story structure.....	32
Figure 5: Test setup for the 6-story structure and wind load	32
Figure 6: Measured acceleration under wind load: (a) Sixth story (b) First story	33
Figure 7: Measure strain under wind load: (a) Sixth story (b) First story	34
Figure 8: Comparison of the roof displacement using various methods	35
Figure 9: Comparison of the roof displacement using various methods: (a) Full record (b) Partial record	36
Figure 10: Displacement tracking using the KLT.....	42
Figure 11: Processes of the phase-based motion processing (PBMP).....	44
Figure 12: Proposed framework for system identification using computer vision.....	48
Figure 13: The process of obtaining mode shapes using Option B shown in Figure 12	48
Figure 14: Test setup for the small-scale 6-story structure.....	52
Figure 15: (a) The tracked displacements at each story (the resolution is 1080p with 120 fps, downsampled to 30 Hz). (b) The PSDs of displacement measurements in (a). (c) The PSDs using the double derivative of displacement measurements in (a).....	54
Figure 16: (a) Accelerometers measurements at each story (downsampled to 30 Hz). (b) The PSDs of measurements in (a). (c) The average of PSDs in (b) using a logarithmic scale for the y-axis	55

Figure 17: Identified six bending modes of the small-scale 6-story structure using measurements from accelerometers.....	56
Figure 18: (a) Normalized average PSDs using displacements from computer vision (1080p video used in Figure 15) and accelerations from accelerometers. (b) Normalized average PSDs using accelerations from computer vision and accelerometers measurements. (c) Similar to (b) but using a logarithmic scale for the y-axis	57
Figure 19: Identified mode shapes using computer vision (1080p video that is used in Figure 15) vs. accelerometers	59
Figure 20: Extracted example frames from the magnified videos, one magnified video per mode.	60
Figure 21: (a) The tracked displacements at each story (the resolution is 4K with 30 fps. (b) The PSDs of measurements in (a). (c) The PSDs using the double derivative of measurements in (a)	62
Figure 22: (a) Normalized average PSDs using displacements from computer vision (4K video used in Figure 21) and accelerations from accelerometers. (b) Normalized average PSDs using accelerations from computer vision and accelerometers measurements. (c) similar to (b) but using a logarithmic scale for the y-axis	63
Figure 23: Identified mode shapes using computer vision (4K video used in Figure 21) vs. accelerometers.....	65
Figure 24: Layout of the 3-D truss bridge	66
Figure 25: The experimental truss bridge	67
Figure 26: Joints labels of the front panel (monitored 11 joints are circled).....	67
Figure 27: Test setup of the experimental truss bridge.....	68

Figure 28: (a) The tracked displacements of the bottom chord of the front panel (the resolution is 1080p with 120 fps). (b) The PSDs of measurements in (a).....	70
Figure 29: (a) Accelerometers measurements at the bottom chord of the front panel (downsampled to 120 Hz). (b) The PSDs of measurements in (a).....	71
Figure 30: (a) Normalized average PSDs from computer vision (1080pi video Figure 28) and accelerations from accelerometers (b) Normalized average PSDs using accelerations from computer vision and accelerometers measurements (using a logarithmic scale for the y-axis) ..	72
Figure 31: Identified first mode shape using computer vision (1080pi and 120 fps) vs. accelerometers (120 Hz)	73
Figure 32: Before magnification.....	74
Figure 33: After magnification	74
Figure 34: (a) The tracked displacements of the bottom chord of the front panel (the resolution is 4K with 30 fps). (b) The PSDs of measurements in (a).....	75
Figure 35: (a) Accelerometers measurements at the bottom chord of the front panel (downsampled to 30 Hz). (b) The PSDs of measurements in (a).....	76
Figure 36: Normalized average PSDs from computer vision (4K video) and accelerometers	77
Figure 37. Identified first mode shape using computer vision (4K and 30 fps) vs. accelerometers (30 Hz)	77
Figure 38: A 2-D truss example with 45 elements	81
Figure 39: Flexibility matrix construction	82
Figure 40: Processes of damage identification using the DLV method.....	83
Figure 41: The framework of damage identification for the numerical and the experimental investigations	84

Figure 42: The 3-D truss bridge model in SAP2000	85
Figure 43: (a) Input force record (b) The PSD of record in (a)	85
Figure 44: The 3-D truss model in SAP2000 with elements labels	86
Figure 45: PSDs from numerical outputs from SAP2000 (a) no noise (b) with noise	87
Figure 46: Mode shapes from the 3-D truss model in SAP2000	88
Figure 47: Example case where the damaged element is number 7 by 50%	89
Figure 48: The location of the included 11 vertical DOFs (shown in circles) and the labeled damage locations	89
Figure 49: Mode shapes for case 1 (element 37 is damaged by 40%).....	91
Figure 50: Results for case 1 using acceleration without noise including: (a) Two modes (b) Three modes	91
Figure 51: Case 1 using acceleration with 5% RMS noise and including: (a) Two modes (b) Three modes	92
Figure 52: Case 1 using displacement with 5% RMS noise and including: (a) Two modes (b) Three modes	92
Figure 53: Mode shapes for case 2 (element 33 is damaged by 30%).....	93
Figure 54: Case 2 using acceleration without noise and including: (a) Two modes (b) Three modes	94
Figure 55: Case 2 using acceleration with 5% RMS noise and including: (a) Two modes (b) Three modes	94
Figure 56: Case 2 using displacement with 5% RMS noise and including: (a) Two modes (b) Three modes	94
Figure 57: Mode shapes for case 3 (element 33 is damaged by 50%).....	95

Figure 58: Case 3 using acceleration with 5% RMS noise and including: (a) Two modes (b) Three modes 96

Figure 59: Case 3 using displacement with 5% RMS noise and including: (a) Two modes (b) Three modes 96

Figure 60: Mode shapes for case 4 (element 7 is damaged by 50%)..... 97

Figure 61: Case 4 using acceleration without noise and including: (a) Two modes (b) Three modes 97

Figure 62: Case 4 using acceleration with 5% RMS noise and including: (a) Two modes (b) Three modes 98

Figure 63: Case 4 using displacement with noise and including: (a) Two modes (b) Three modes 98

Figure 64: Damage identification for element 33 where: (a) Two actual modes are included. (b) Five actual modes are included. (c) One actual mode and one aliased mode are included. (d) One actual mode and four aliased modes are included. 100

Figure 65: Damage identification for element 2 where: (a) Two actual modes are included. (b) Five actual modes are included. (c) One actual mode and one aliased mode are included. (d) One actual mode and four aliased modes are included. 101

Figure 66: Damage identification for (a) Damaged element 33 and (b) Damaged element 2. Actual modes: included from 1 to 20 actual modes. Aliased modes: included from 1 to 20 aliased modes, where the first mode is actual, and the remaining 19 modes are aliased. 102

Figure 67: Test setup for damage identification (the locations of the substituted damaged elements are labeled)..... 103

Figure 68: Substituted element 9, which has a 30% reduction in cross-sectional area 104

Figure 69: Mode shapes for case 5 from measured acceleration (element 9 is damaged by 27%)
..... 106

Figure 70: Case 5 using measured acceleration and including: (a) Two modes (b) Three modes
..... 106

Figure 71: Mode shapes for case 6 from measured acceleration (element 33 is damaged by 45%)
..... 107

Figure 72: Case 6 using measured acceleration and including: (a) One mode (b) Two modes . 107

Figure 73: Mode shapes for case 7 from measured acceleration (element 7 is damaged by 27%)
..... 108

Figure 74: Case 7 using measured acceleration and including: (a) Two modes (b) Three modes
..... 109

Figure 75: Mode shapes for case 8 from measured acceleration (element 7 is damaged by 45%)
..... 110

Figure 76: Case 8 using measured acceleration and including: (a) Two modes (b) Three modes
..... 110

List of Tables

Table 1: Building design parameters	27
Table 2: Designed cross sections of the members in the moment frame	27
Table 3: Peak error and FDE for the estimated displacement	30
Table 4: Peak error and FDE for the estimated displacements	37
Table 5: EMAC and MAC values for mode shapes in Figure 19	59
Table 6: EMAC and MAC values for mode shapes in Figure 23	65
Table 7: Summary of the numerically investigated cases	90
Table 8: Actual and aliased first five modal frequencies of the truss bridge	103
Table 9: Summary of the experimentally investigated damage cases	105

CHAPTER 1: INTRODUCTION

Structural health monitoring (SHM) is an active field in civil engineering that aims to assess the condition of structures and to detect damage using measured structural response [41, 82, 110]. For example, SHM is essential for structural design validation, damage identification, in-situ-load characterization, emergency response, construction efficiency, construction safety, maintenance efficiency, and more [112]. Condition assessment of structures can be implemented through non-destructive testing or vibration-based methods. Non-destructive testing focuses on the member level without considering the global behavior of the structure (i.e., acoustic emission, ultrasonic) [56]. On the other hand, condition assessment using vibration-based methods considers the global behavior of the structure. These methods have the advantage of using discrete locations to characterize the global behavior of structures. Visual inspection and vibration-based are commonly used methods for condition assessment of structures.

In practice, visual inspection has been one of the major ways to evaluate the condition of structures. The main issues associated with the visual inspection are that it is prone to error since it relies on the visual ability of the inspector, is time-consuming, is labor-intensive, and is ineffective in terms of cost [2, 67, 72, 78]. For example, the tragic collapse of the I-35 W bridge in Minnesota in 2007 happened after it passed the visual inspection only a year earlier. Besides, visual inspection is usually limited to maintenance and integrity evaluation purposes and does not benefit other goals of SHM, such as structural design validation and actual load characterization.

Vibration-based methods are becoming more common due to their ability to benefit all SHM goals, their high efficiency, and their high reliability. Also, vibration-based SHM methods allow continuous monitoring, provide higher accuracy, reduce the labor needed, and increase time

efficiency [2, 22, 24]. These advantages allow the maintenance strategy to shift to predictive condition-based rather than preventive time-based [94].

Vibration-based methods are common for bridges and tall-buildings structures in different locations of the world. For example, Tsing Ma Bridge in Hong Kong is instrumented with about 600 sensors for SHM purposes [39]. Other long-span bridges in Hong Kong, such as the Kap Shui Mun Bridge, the Ting Kau Bridge, have installed SHM systems [126]. Some of the large-scale bridges in the United States have installed SHM systems such as the I-40 bridge [40] and the Commodore Barry Bridge [9, 96].

The tallest building globally, Burj Khalifa in Dubai, used a temporary SHM system during construction, and it also has a permanent SHM system. These systems include different sensors types such as accelerometers and Global Position System (GPS) systems [1, 7, 52]. Other examples of tall-buildings that installed SHM systems are the Shanghai tower and Guangzhou TV tower in China [7, 84, 135].

The vibration-based assessment can rely directly on evaluating the response measurements, such as residual displacement, peak displacement, and peak acceleration [42, 98, 100]. It also can use the response measurements to perform change characterization (i.e., system identification and damage identification) [6, 24, 38, 95]. Accurate displacement estimation is essential in assessing the condition of structures by evaluating the response or using the displacement in change characterization. Displacement is commonly measured indirectly by converting acceleration measurements to displacement [69, 108]. This approach can provide an accurate estimation of the displacement in some cases. However, in other cases, such as estimating pseudo-static displacements (or the low-frequency displacement) and residual displacements, the acceleration measurements cannot accurately estimate the displacement [90, 108]. The pseudo-static

displacement is critical in some cases, such as structures subjected to nonstationary wind. In this case, the pseudo-static displacement cannot be estimated using acceleration measurements.

Furthermore, the change characterization using traditional sensors requires excessive instrumentation and physical contact with the structure [76]. Computer vision methods can overcome these challenges and can be more effective in terms of cost and labor compared to traditional sensors [36]. However, computer vision methods face the difficulty of using the small motion of structures or the need for impractical procedures (i.e., high-speed cameras or specific lighting conditions). These challenges limit the applicability of computer vision in system identification and damage identification.

The objective of this research is to improve the use of traditional sensors and computer vision in SHM. This research improves the estimation of structural displacement under nonstationary load by using sensor data fusion. Additionally, this research proposes computer vision methods for system identification and damage identification. In particular, this research addresses inaccurate displacement estimation under nonstationary wind by proposing two data fusion methods. This research also addresses some of the existing limitations and challenges of using computer vision in system identification and damage identification. Computer vision methods for system identification and damage identification are proposed in this research. These methods use consumer-level cameras and are able to rely on small structural displacements.

Chapter 2 includes a background and literature review of the related previous studies to this dissertation's presented research. This chapter includes a general overview of displacement estimation methods—acceleration-based, strain-based, and data fusion—, system identification focusing on computer vision, and damage identification.

Chapter 3 discusses the two proposed methods for displacement estimation for building structures using data fusion, which eliminates the need to use mass-normalized mode shapes. This chapter includes the theoretical formulation of the proposed methods, numerical investigation, and experimental validation.

Chapter 4 proposes a method for system identification using computer vision that uses consumer-level cameras and is able to rely on a small structural motion. This chapter includes detail of the proposed framework procedures along with experimental validation. It also provides guidelines and details for pre-recording and post-processing steps. The experimental validation examines the proposed framework using two structures: a small-scale 6-story building structure and a 3-D experimental truss bridge. The obtained results from computer vision are compared with the obtained results from the reference acceleration measurements.

Chapter 5 investigates computer vision for damage identification. This chapter adopts a damage localization method that relies on measured flexibility matrices (before and after the damage). This chapter discusses the numerical and experimental investigations using the 3-D experimental truss bridge. This chapter also explores the possibility of including temporal-aliased modes for damage identification using computer vision.

Chapter 6 summarizes the main findings from the presented research. Additionally, it provides some remarks for future studies.

CHAPTER 2: BACKGROUND AND LITERATURE REVIEW

This chapter provides a literature review and a general background of the previous studies related to the topics presented in this dissertation. This chapter includes a general overview of displacement estimation methods using: acceleration, strain, and data fusion. It also provides a review of system identification, with a focus on computer vision. This chapter also discusses damage identification methods, including methods that use dynamically measured flexibility matrix.

2.1. Displacement estimation methods

For vibration-based SHM methods, the structural displacement is an important measurement and indicator of structural damage and integrity. Building codes limit the maximum allowable story drift based on the occupancy category of the building structure. However, measuring structural displacement is usually a challenging task. Meanwhile, direct measurements using displacement sensors such as Linear Variable Differential Transformers (LVDT), string pots, and dial gauges require a fixed reference point, which is unlikely to be available in the field [69]. As a result, other methods use indirect measurements to measure the structural displacement. These methods can be based on acceleration, strain, or data fusion that combines multiple types of measurements.

2.1.1. Acceleration-based methods

Acceleration-based methods are common in estimating structural displacement. This popularity is due to their reasonable accuracy in general, their simplicity, and their economic effectiveness when compared to direct methods [69, 108, 109]. Additionally, acceleration-based methods are more practical in most cases since they do not require a fixed reference point, while direct methods do require a fixed reference point [69, 122].

Several issues have been identified, based on experience, with acceleration-based methods. Double integration of acceleration is a commonly applied method in estimating structural displacements [108]. This method involves some issues that usually lead to an unrealistic estimation of the velocity and displacement records [48, 55]. There is a tremendous effort in different studies to identify the sources of the unrealistic values that result from double integration of acceleration. Other studies provide multiple solutions, or correction schemes, to overcome this issue.

One of the early studies that discussed the unrealistic displacement estimation from double integrating the acceleration was in 1947 by Housner [55]. He computed ground displacement by double integrating the acceleration records and compared it to the measured ground displacement, which was obtained using displacement meters during the 1933 Los Angeles earthquake at the Subway Terminal station [55]. Housner observed an unrealistic drift in the estimated displacement from double integration of acceleration, which he attributed to two reasons. The first reason is the late triggering, which results in missing the ground motion's initial shock. The second reason is the inaccurate baseline on the accelerograph. Housner suggested establishing a baseline correction to improve estimated displacement accuracy from double integrating the acceleration [55].

Berg and Housner proposed a method in 1961 to estimate velocity and displacement by double integrating acceleration records during strong motion and applying correction processes [48]. In this method, they assumed zero initial velocity and zero initial displacements. The method also used a "temporary straight baseline," which is calculated from the measured acceleration. They used the acceleration records from the California Institute of Technology for the Pasadena earthquake of July 21, 1952, to compute the displacement using their method. The displacement is then compared to the measured displacement from the same location. A reasonable agreement

was found between the estimated and the measured displacements. The deviation between the two displacements was attributed to the instruments' limitations [48].

Other researchers identified other sources that can lead to an unrealistic estimation of displacement by double integrating the acceleration. For example, measurement noise can cause an unrealistic drift in the estimated displacement. In 1971, Trifunac proposed a correction process that applies a baseline correction and applies a high pass filter to the uncorrected digitized acceleration [119]. By comparing his method with the classical parabolic baseline correction, Trifunac argues that his method produces accurate estimation regardless of the record length, and that the accuracy of the classical parabolic correction is directly affected by the record length [119].

Another method that involved correction processes in estimating displacement by double integrating the acceleration was proposed by Iwan et al. in 1985. They proposed a baseline correction method that removes two baselines from the record at two different time steps [59]. Boore then adopted this method and argued that the derived velocities from the corrected acceleration records from the 1999 Chi-Chi earthquake showed a linear trend for systems that have long periods of vibrations [17]. According to Boore, structures with periods of less than 20 sec should not be sensitive to the applied baseline correction method. Two years later, Boore published another study that discussed other unrealistic drift sources in the double integrated acceleration [16]. According to Boore, converting analog data to digital data can introduce pulses in the output. Additionally, the offset in the acceleration baseline can cause a deviation in the calculated displacement [16].

In 2006, Yang et al. [129] proposed an alternative baseline correction method. The method applies the correction to the acceleration measurements in the time domain before the integration processes. The least-square curve fitting technique was used combined with further processing in

the frequency domain, where window filtering was applied to remove the sources of the low-frequency components. They compared their method with the proposed method by Trifunac (1971) [119], and their method yielded better results within the included case studies [129].

In 2007, Gindy et al. published a study that examined two correction methods to estimate bridge displacement from acceleration measurements [50]. They estimated the displacement using the velocity estimation method (VEM), which estimates the initial velocity through an iteration process, and the baseline correction method (BCM). The experimental investigation was conducted on a three-span continuous bridge with a controlled live load. From the measured acceleration, they estimated the displacement using the two methods and then compared it to the measured displacement. The BCM method yielded a more reasonable displacement profile than the VEM method for various loading patterns [50].

Baseline correction is not the only correction that can be applied to improve displacement estimated from acceleration. Filtering the acceleration is another widely used technique to enhance the estimated displacement. In general, filtering is applied to remove high-frequency or low-frequency components using low-pass or high-pass filters [119]. Filtering alone can yield a significant improvement in the estimated displacement. Combining baseline correction with filtering enhances the estimated displacement from acceleration [69].

In 2010, a comprehensive study was published by Skolnik and Wallace about the assessment of the story drift (SD) measurements [108]. The study concluded that calculating story drift by double integrating acceleration measurements is challenging due to the associated issues with the involved signal processing procedures and instrumentation limitations. They argue that calculating displacement from acceleration involves subjective signal processing procedures. These procedures include the band-pass filtering, assuming zero value at the end of the signal, and

the applied baseline correction method. Skolnik and Wallace suggest improving the quality of the signal by applying an initial baseline correction and low-pass filtering before the integration process. The low-pass filtering is applied to reduce the amplitude of the noise. They also suggest subtracting the constant value from the raw acceleration that results from the surrounding conditions, such as a change in temperature [108]. They have stated that the error in the estimated displacement from acceleration can be as low as 5% for linear response. However, for a nonlinear response, the residual displacement will be eliminated and the error can be higher than 12% [108].

These discussed studies to estimate and correct displacement from acceleration assumed the displacement has zero-mean [16, 17, 48, 55, 59, 119], which is valid for some cases such as linear structural response during an earthquake. However, in other situations, the structural displacement response may not have a zero-mean. For example, the nonlinear response of structures and the nonlinear ground displacements contain residual displacements [21, 66, 71, 100], which are eliminated by the correction process when using acceleration to estimate displacement [108, 118]. The structural displacement response of bridges due to moving load or wind load could have fluctuating displacement component (or pseudo-static displacement) [51, 70, 79, 113, 136], which is also eliminated by the correction process in estimating displacement from acceleration [90]. Similarly, the displacement response of building structures subjected to nonstationary wind load contains pseudo-static components [15, 32, 57, 65, 111, 115], which is also eliminated when applying the correction process to estimate displacement from acceleration. The third chapter of this research addresses this issue by combining acceleration and strain measurements to estimate displacement for building structures under nonstationary wind.

2.1.2. Strain-based methods

Strain measurements have also been used to estimate dynamic displacement in different fields, such as airplanes' wing deflection and bridges' deflection [44, 90]. This section presents some of the key studies about strain-based methods to estimate structural displacement.

In 1995, Foss and Haugse published a study that discusses some major issues in using strain measurements [44]. For example, the low amplitude level that can be reached from modal excitation sources, which could lead to low-quality frequency response function (FRF) estimation. The study also compared the signal-to-noise ratio (SNR) in acceleration and strain measurements, where the SNR in acceleration was better compared to those of strain measurements. Foss and Haugse also stated that it is challenging to obtain accurate strain measurements if the strain is less than ten microstrains, where the strain level usually varies from microscale to almost nonexistent [44]. This study stated other issues that might affect strain measurements' accuracy, such as the change in the surrounding temperature or the quality of strain gauge attachment [44]. Foss and Haugse proposed a method that uses a transformation matrix to convert strain to displacement. This transformation matrix can be derived from mass-normalized displacement and strain mode shapes. They conducted an experimental validation of the proposed method on a cantilever plate [44].

In 1995, Pisoni et al. also published a study that discusses strain-to-displacement conversion [97]. The proposed method relies on performing modal analysis to identify the displacement mode shapes. In addition, they estimated some parameters from the transfer function to define the displacement as a function of mode shapes and strain. Experimental validation was conducted using a clamped-end beam's free vibration to calculate the displacement from strain using the proposed method. A reasonable agreement was found between the calculated

displacement and measured displacement only after the high-frequency died out of the strain measurements [97]. However, this method overestimated the displacement calculation from the strain before the strain's high-frequency components died out. According to the study, the reason for the overestimation is the high dynamic sensitivity in strain measurements compared to displacement measurements. A low-pass filter was applied to filter frequencies higher than 200 Hz, which enhanced the calculated displacement from strain [97].

Kang et al. (2007) published a study to investigate the accuracy of converting strain measured by Fiber Bragg Grating (FBG) sensors to dynamic structural displacement [64]. The selection of the FBG strain sensors was due to their multiple abilities. Different loading scenarios were applied to two different beam specimens —aluminum and acryl— for the experimental investigation. The mass-normalized mode shapes were obtained by performing a shaker test. In the study, the displacement was accurately estimated using the FBG sensors [64].

In 2014, Wang et al. proposed a method to estimate the beam's displacement using strain measurements [124]. This method is based on the relationship between the strain and displacement and the use of displacement and strain mode shapes. In this study, the strain mode shapes were estimated using the cross-correlation function of the measured strain. Numerical and experimental tests were conducted using a simply supported beam subjected to earthquake and impulse loads to validate the proposed method. According to the study, the method was able to estimate the beam's displacement at any location using strain measurements with about 7% error [124].

From these presented studies, strain-based methods have the potential to estimate structural displacements. However, the strain-to-displacement conversion relies on the use of the mass-normalized displacement and strain mode shapes. Identifying accurate mass-normalized mode shapes of structures is challenging, and it is not possible in some cases. It is challenging because

it requires knowing the input excitation force, which is impossible for operational modal analysis that uses ambient excitation [14, 30, 47, 68, 73]. Other methods can obtain the mass-normalized mode shapes by modifying the structure's modal parameters, such as mass-change or stiffness-change strategies [18, 19, 29, 73, 74, 92]. Although these strategies overcome the need for requiring artificial excitation, these methods require significant modifications to the modal parameters by changing the structure's mass or stiffness, which are also challenging tasks.

Besides the challenge of the need for mass-normalized mode shapes, strain measurements are known for their relatively low accuracy in estimating the dynamic displacement components, and they can overestimate the calculated displacement [90, 97]. This challenge of using the strain-based method can be overcome by using data fusion methods, such as combining acceleration and strain in the displacement estimation.

2.1.3. **Data fusion methods**

Multiple researchers also investigated the use of both acceleration and strain measurements to estimate displacement. In 2013, Park et al. proposed a method that combines acceleration and strain measurements to estimate the displacement of bridge structures [90]. The objective of the study was to preserve the pseudo-static displacement components of bridges under traffic loading. This method was motivated by the fact that acceleration can accurately estimate the dynamic part of the displacement, discussed in section 2.1.1. On the other hand, the strain can capture the pseudo-static components. The proposed method estimates nonzero mean dynamic displacement by fusing acceleration and strain measurements. The reason for combining strain with acceleration measurements is acceleration measurements alone cannot estimate nonzero mean displacement [90]. Traditionally, the acceleration-to-displacement conversion passes through different

correction methods, such as high-pass filtering and baseline correction, which lead to the elimination of the pseudo-static displacement component as it was discussed in section 2.1.1.

On the other hand, estimating displacement from strain measurements only has some difficulties, especially for high-frequency modes. According to Park et al., fusing the acceleration and the strain measurements improves estimating nonzero mean displacement. The validity of this method was supported by conducting numerical and experimental investigations [90].

In 2015, Cho et al. [28] proposed an improvement to Park et al.'s method by using mode shapes from a finite element model [90]. According to Cho et al. (2015), the method proposed by Park et al. is limited to a beam-like structure because it uses analytically assumed mode shapes (sinusoidal mode shapes). The improved method was validated numerically and experimentally using bridge structures [28].

The discussed studies of data fusion methods confirm the advantage of combining acceleration and strain measurements to estimate non-zero mean displacement accurately. However, the use of assumed mode shapes limits the applicability of the method. In addition, using mode shapes from a finite element model might be challenging and time-consuming. The third chapter proposes two data fusion methods for building structures. These methods use mode shapes that are derived from measurements, and it overcomes the need for mass-normalized mode shapes.

2.2. System identification

For structural health monitoring, system identification is an essential tool to establish a solution for a broad range of problems. For example, system identification is essential for damage identification, model updating, structural control, among others, and is also beneficial for design validation [54, 94]. System identification uses measured data from a dynamic system to build a

representative mathematical model. System identification also includes the experimental modal analysis, which usually aims to identify the natural frequencies, damping ratios, mode shapes, and modal participation factors of the structure [94]. Several methods have been developed to perform system identification for structures. In general, system identification methods are classified into two major categories, which are parametric and nonparametric methods [72]. This classification is determined by whether the method is based on assuming a parameterized model of the original system.

Parametric methods are mainly time-domain methods such as the Eigensystem Realization Algorithm (ERA) method proposed by Juang and Pappa in 1985 [61]. The ERA method can perform modal parameter identification and modal reduction of dynamic systems using the structure measurements. Another example of parametric methods is the Stochastic Subspace Identification (SSI) proposed by Overschee and Moor in 1996 [86].

Nonparametric methods are mainly frequency-domain methods, and they are generally more efficient; however, they are less accurate than parametric methods. Besides, nonparametric methods generally require relatively a large amount of data to achieve acceptable accuracy. A standard nonparametric method for system identification is the Peak-Picking method that has been used by different studies [12, 20, 43]. The following section 2.3 discusses some of the key studies that use computer vision for system identification.

2.3. Computer vision methods

This section discusses the key computer vision studies for displacement tracking, motion magnification, and system identification. Some of these studies only track the displacement response, while other studies use the tracked response for extended applications. This section

focuses on identifying the abilities and limitations of these related previous studies that use computer vision.

In 1981, Lucas and Kanade proposed an iterative method that makes image registration faster than the traditional methods [75]. This method approximates the second derivative of an image to reduce the computational time. Tomasi and Kanade later adopted this method. In 1991, Tomasi and Kanade proposed a method to track features in the images that are suitable for the tracking algorithm [117]. Tomasi and Kanade's method selects feature points based on a defined threshold for the gradient matrix and eigenvalues. These two papers yielded the Kanade-Lucas-Tomasi (KLT) feature tracker that is widely used to measure displacement. In 1994, Shi and Tomasi proposed to examine the quality of the tracked feature points in the KLT method [103]. This examination measures feature dissimilarity between the current frame and the reference frame [103].

In 2002, Patsias and Staszewski published a study that discussed using optical measurements with wavelet transform for damage detection using a simple cantilever beam experiment [93]. The used vision system for damage detection was a high-speed camera system from Kodak, which support a wide range of frame rate from 40 to 600 frames per second and a resolution range from 160×60 to 640×240 pixels. The results showed that the proposed method successfully detected the damage in the simple cantilever beam. According to Patsias et al., the major limitation of the method is that it requires significant deflections [93].

In 2011, Caetano et al. investigated the use of computer vision for vibration monitoring of civil structures [23]. This study discussed two experiments on two bridges in Portugal: the Coimbra footbridge and a movable cable-stayed footbridge located in Viana do Castelo. Both experiments investigated the ability to use computer vision to measure the responses of the cables and the

bridges, and use these measurements to identify the parameters of the system. The vision system was located 100 meters from the object and used a camera with a resolution of 800×600 pixels and a frame rate of 30 frames per second. A special lens was also utilized along with a unique feature called progressive scanning to use half of the resolution and double the frame rate. For both experiments, the results showed that it could measure the velocity of an object in the order of 0.01 m/s. In addition, the result showed the possibility of identifying the structures' frequencies using computer vision measurements [23]. However, the study did not attempt to identify the mode shapes of the structure.

In 2013, the Phase-Based Video Motion Processing (PBMP) method was proposed by Wadhwa et al. [121]. This method introduced the ability to manipulate small motions in videos with low sensitivity to noise. The PBMP method is based on analyzing the motion in complex-valued pyramids [105]. In the PBMP method, the motion is manipulated by amplifying or attenuating the phase variation of the complex steerable pyramids over time using temporal filtering. In this study, Wadhwa et al. (2013) also compared their magnification methodology and their results with Linear Eulerian Video Magnification (LEM) method [127]. The PBMP method can support about four times the magnification factor than the LEM method. In addition, the PBMP showed much less sensitivity to noise than the LEM method. The noise is translated in the PBMP method rather than amplified linearly as in the LEM method [121]. The PBMP method was adopted by several studies to perform structural system identification, such as the following studies.

Yang et al. (2017) adopted the PBMP method [121] and the complexity pursuit (CP) algorithm [114] to blindly identify the structure's modal parameters using computer vision [133]. The experimental investigation of the method used a small-scale three-story structure. The free

vibration response of the structure is recorded using Sony NXCAM with a special lens that reaches a sampling rate of 480 fps placed close to the structure. The method was able to identify the natural frequencies of the structure and validated them with the identified frequencies from the attached accelerometers. The method used edge detection to produce a few temporal frames for each mode shape. According to Yang et al., edge detection may require manual adjustment to remove the non-structural components from these frames [133]. The method did not explain how to extract the mode shapes from these frames for extended applications, such as damage identification. Also, this study did not provide a validation of the mode shapes with any other experimental measurements.

Chen et al. (2018) published a study that discusses measuring the response of the World War I Memorial Bridge in Portsmouth, New Hampshire, using a camera-based vibration measurement method [27]. The objective of the study is to measure the displacement and perform system identification of the WWI Memorial Bridge using camera-based measurements. The vertical-left middle span is used to impact the bridge, and the response is measured using a camera that is 80 meters away from the structure. The average displacement measurements was about $1/100^{\text{th}}$ pixel, and the resolution of the camera was 800×600 pixels with a frame rate of 30 frames per second. This study adopted the Phase-Based Video Motion Processing (PBMP) method and used phase variation to track the structure's motion. An acceptable agreement was found between the measured displacement using the camera and the integrated displacement from the acceleration measurements. The results showed the potential of using camera-based measurements to identify the structure's natural frequencies [27]. The study also provided mode shapes as phase images, but it did not provide a way to extract these mode shapes for extended applications. Besides, the study did not validate these mode shapes images with any other experimental measurements.

In 2019, a 3D-structural identification method through computer vision was proposed by Harmanci et al. [53]. The method is named Magnified Tracking (MT), which adopted the PBMP method by Wadhwa et al. (2013) [121] and a motion tracking method using Particle Tracking Velocimetry (PTV) by Virant and Dracos (1997) [120]. The MT method performs system identification through multiple stages, including image acquisition, calibration, magnification, high-pass filtering, particle detection, coordinates extraction, and linking [53]. The experimental part of the study was conducted on a small shear frame with a total height of 60 centimeters, which was illuminated using high-power LED spotlights accompanied by flat mirrors and an image splitter. The computer vision measurements were collected using an exceptional camera named Fastcam SA5 high-speed camera (Photron, Tokyo, Japan), which is capable of recording a video with a frame rate of 7,000 frames per second and a resolution of 1,024×1,024 pixels (Harmanci et al., 2019). According to Harmanci et al., the MT method showed the potential for using computer vision measurements for system identification. However, the requirement of having a specific contrast between the tracked object and the background for the PTV is a limitation for outdoor implementations [53].

In summary, the existing limitations in the related computer vision studies can be classified into two categories. First are the limitations of these studies' experimental setup, which require: large deflections, special impact loading, special illumination conditions, indoor applications, or exceptional computer vision systems. The other limitations are related to the extended applications of the identified modal parameters, which are mainly the challenge of extracting and validating the mode shapes from some of these studies. The fourth chapter of this dissertation proposes a computer vision method for system identification that addresses these limitations and challenges.

2.4. Damage identification

A damage in a structure changes its dynamic characteristics, leading to a change in the modal parameters (or vibration modes) [87, 88, 102]. The vibration-based methods for damage identification rely on the fact that the structure's global dynamic characteristics are affected by local stiffness change [128]. Therefore, a change in the structure's modal parameters can be a sign of damage in the structure [104, 128]. Damage identification is often classified using three levels: detection, localization, quantification [101].

Damage detection using only the change in the frequency of structures is challenging because it requires very precise measurements or a significant damage level [34, 94]. Additionally, a slight change in the structural frequency does not necessarily indicate that the structure has damage. Other factors can result in frequency change, such as a change in temperature. Damage localization has traditionally been based on the difference in the mode shapes or derivative of the mode shapes without requiring a detailed model of the structure [45, 77, 88, 99, 125]. Other methods are based on updating the modal parameters, which tend to be complicated because these methods modify the structural model matrices [10, 26, 33, 62, 85]. For example, in the FEM updating methods, the damage-related parameters are updated, meaning that the model's dynamic characteristics are updated to correspond to the measurements [46]. The FEM updating method usually requires a smaller number of sensors, but it needs an analytical model.

Alternatively, damage identification methods that use a static model with dynamically measured flexibility matrices. These methods require only the first few modes of the structure to be measured, making it more practical than the other methods [3, 11, 13, 34, 35, 87, 116].

In 2002, Bernal proposed a method to localize damage in structures by assuming the structure is linear in the pre-damage and post-damage states [13]. This method localizes the

damage by computing a set of damage locating vectors (DLVs), which induce zero stress in the damaged elements. In the presence of measurement noise and approximation, the DLVs will induce relatively small stress in the damaged elements. The DLVs are computed as the null space of the change in measured flexibility and are associated with measurement locations. This method requires a representative model for static analysis in the undamaged state [13]. The concept behind the DLV method is that it produces identical deformation in the damage and the undamaged states, which allows the method to use the change in the flexibility matrices (between the damaged and the undamaged states) to localize the damage [13]. The DLV method is adopted in this study as a part of the proposed framework for damage identification using computer vision in Chapter 5.

2.5. Summary

This chapter reviewed and gave a general overview of some fundamental studies related to the presented research topics in this dissertation. The gaps in knowledge in these topics were identified in this chapter. Displacement of building structures subjected to nonstationary wind cannot be estimated accurately using acceleration measurements. The third chapter of this dissertation addresses this issue by proposing two data fusion methods that combine acceleration and strain measurements without the need for mass-normalized mode shapes.

The system identification of structures using traditional sensors (i.e., accelerometers) requires physical contact, is time-consuming, is labor-intensive, and is ineffective in terms of cost. The system identification using computer vision can overcome these challenges. However, as was discussed earlier, there are existing limitations in the computer vision studies related to the test setup or the extended applications. The test setup limitations include requiring large deflections, special illumination conditions, indoor applications, among other limitations that limit the applicability of computer vision. The fourth chapter of this dissertation proposes a computer vision

method for system identification that overcome these challenges. Also, the proposed method uses consumer-level cameras and can rely on small structural motions.

Damage identification of structures using traditional sensors faces similar challenges as the system identification because it requires identifying the system before and after the damage. The fifth chapter investigates the use of computer vision in damage identification and discusses its advantages and limitations. This chapter also investigates the impact of temporally aliased modes on damage identification. To the best of the author's knowledge, this is the first study to investigate the impact of aliased modes on damage identification.

CHAPTER 3: DISPLACEMENT ESTIMATION USING TRADITIONAL SENSORS

3.1. Introduction and background

Measuring displacements of structures is a challenging task. Direct measurement approaches using displacement sensors such as Linear Variable Differential Transformers (LVDTs), dial gauges, and string potentiometers require a stationary fixed reference point for installing these sensors, which is likely unavailable in the field [69, 122]. Non-contact measurements such as Global Position System (GPS) and laser-based methods may also be used, which can be expensive if high accuracy is desired [60, 70, 122].

Displacements can be calculated from acceleration measurements. One common approach to calculate displacement is to use double integration of the acceleration record. However, this approach does not typically provide a reliable solution due to the inaccuracy in the numerical integration itself, measurement noise, and the unknown initial conditions [129]. Many correction processes, such as baseline correction, are likely to remove some critical information, such as the low-frequency components of structural displacement [90]. These missed components might dominate the displacement in some cases, such as under nonstationary wind events.

To provide a reliable estimation of zero-mean displacements from acceleration measurements, Lee et al. (2010) proposed a displacement reconstruction method using approximated accelerations (from a second-order central finite difference of displacements) [69]. The displacements are then optimized by minimizing the least-squared errors between the measured accelerations and calculated accelerations from displacements. This method can be considered as a Finite Impulse Response (FIR) filter formulated in the time domain, and is therefore referred to as the time-domain FIR filter method in this study. It is designed to work with

a moving-time window, which leads to missing parts of the reconstructed displacements at the boundaries (start and end) of the record. The missing parts might be critical, especially the initial part, because in some events the peak displacement happens early in the record.

On the other hand, strain measurements have also been used to reconstruct displacements. The process relies on the displacement mode shapes and strain mode shapes, which are both mass-normalized, to convert strain to displacement. However, in practical applications, identifying mass-normalized mode shapes is challenging in large-scale structures mainly because of the need to measure the output at the same location of the input [30].

This chapter proposes two methods for estimating dynamic displacements with pseudo-static components using acceleration and strain measurements. The first method (Data fusion method A) uses acceleration measurements for scaling and uses strain measurements to calculate the displacement; however, this method does not require mass-normalized mode shapes. The second method (Data fusion method B) combines strain and acceleration measurements for better accuracy. Both proposed methods are validated numerically and experimentally. The numerical validation uses an idealized 20-story building structure subjected to nonstationary wind loading. The experimental validation uses a small-scale 6-story structure subjected to wind load generated by two large fans.

3.2. Methodology

3.2.1. Data fusion method A

One of the main challenges in converting strains to displacements is the need to obtain the mass-normalized mode shapes. It requires at least one output to be measured at the same location of the input excitation in experimental modal analysis, which can be challenging to do for large-scale

building structures [30]. To avoid the need for mass-normalized mode shapes, the displacements can be estimated from strain measurements using equations (3-1) through (3-5) [5, 58, 90].

$$\{u\} = S_F (\Gamma_{n \times n} \widehat{\Phi}_{n \times r} \widehat{\Psi}_{r \times m}^+ \{\varepsilon\}_{m \times 1}) \quad (3-1)$$

$$S_F = \frac{\sqrt{Sd_{acceleration}}}{\sqrt{Sd_{strain}}} \quad (3-2)$$

$$\Gamma = \frac{\bar{L}}{\hat{m}} \quad (3-3)$$

$$\bar{L} = \phi^T M \bar{r} \quad (3-4)$$

$$\hat{m} = \phi^T M \phi \quad (3-5)$$

Where S_F is a scaling factor that can be calculated based on equation (3-2). The matrix Γ contains the modal participation mass ratios that can be obtained from an assumed mass matrix, as shown in equation (3-3). $\widehat{\Phi}$ and $\widehat{\Psi}$ are the displacement and strain mode shapes, respectively, both normalized to have the maximum value of each mode shape vector equal to one. Vector ε contains the strain measurements. $Sd_{acceleration}$ is the amplitude of the power spectral density (PSD) of the displacements estimated using acceleration measurements, Sd_{strain} is the amplitude of the PSD (at the same frequency of $Sd_{acceleration}$) from the estimated displacements using strain measurements.

The modal participation mass ratios Γ can be calculated using the generalized mass matrix M and the displacement mode shapes ϕ as shown in equations (3-3) through (3-5) [58]. Where \bar{r} is an influence vector that represents displacements of the masses if a unit ground displacement was applied statically.

In the above formulation, the mass matrix can be estimated based on the structure geometry and known material properties. For building structures, a simplified uniform mass distribution can be assumed. Therefore, a diagonal lumped mass matrix $M_{n \times n}$ can be designated as a unit matrix,

where n is the number of modes considered. The modal participation mass ratios Γ can be estimated with satisfactory accuracy using the assumed mass matrix $M_{n \times n}$.

3.2.2. Data fusion method B

Combining acceleration and strain measurements can potentially lead to a more realistic displacement estimation than using a single type of measurements. For example, for vertical deflections of bridges under traffic and for high-rise buildings under nonstationary wind load, the pseudo-static displacements can be significant. Estimating displacements using only acceleration data may lose the pseudo-static component due to the necessary post-processing. The pseudo-static displacement can be preserved by incorporating strain data. The total displacement can be estimated using the fusion of acceleration and strain data, as shown in Equation (3-6) [90]:

$$\underset{u}{\text{Min}} \Pi = \frac{1}{2} \|L_a(L_c u_i - \Delta t^2 \bar{a}_i)\|_2^2 + \frac{\lambda^2}{2} \|u_i - D_i\{\varepsilon\}\|_2^2 \quad (3-6)$$

The solution of Equation 3-6 is shown in Equation (3-7):

$$u_i = (L^T L + \lambda^2 I)^{-1} (L^T L_a \bar{a}_i \Delta t^2 + \lambda^2 D_i\{\varepsilon\}) \quad (3-7)$$

$$D\{\varepsilon\} = S_F (\Gamma_{n \times n} \widehat{\Phi}_{n \times r} \widehat{\Psi}_{r \times m}^+ \{\varepsilon\}_{m \times 1}) \quad (3-8)$$

Where Δt is the sample time of the measured data, $L = L_a L_c$, L_a is a diagonal weighting matrix with a dimension of $(2k+1)$ by $(2k+1)$, where k is the number of data points, with all diagonal entries of 1 except the first and last entries, which are equal to $1/\sqrt{2}$. L_c is the second-order differential operator matrix of the discretized trapezoidal rule with dimensions of $(2k+1)$ by $(2k+3)$ [69]. λ is a regularization factor for the minimization problem. Lee et al. (2010) suggest using an optimal regularization factor of $\lambda = 46.81 N_d^{-1.95}$, where N_d is the number of data points in the time window [69]. The number of data points in the moving-time window is suggested to be

three times the fundamental period of the structure of interest. To overcome the issue of the missing data points of the reconstructed displacement at the start of the record, zero-padding is proposed. It recovers the missing part by adding imaginary data points before the record, with the number of points equal to half of those in the moving-time window [5].

Equation (3-7) is expressed in terms of both strain and acceleration measurements [90]. It is important to emphasize that to estimate displacements from strains, which is the second term of equation (3-7), does not require mass-normalized mode shapes. Instead, equation (3-8) is used to estimate displacements from strains with mode shapes normalized to have the maximum value equal to one.

3.3. Numerical investigation

3.3.1. Model description (20-story building structure)

A 20-story building structure was modeled numerically in SAP2000 [31] to conduct the numerical investigation of the proposed method. The structural layout and dimensions are shown in Figure 1. The general design assumptions were based on ASCE 7-16 [8], as shown in Table 1. The lateral-force-resisting system of the structure in the X-direction consists two perimeter steel moment frames. For the numerical investigation, only one frame is modeled in SAP2000, which resists half of the lateral load. The participation of the shear walls was neglected in the X-direction.

The beams and columns sizes of the structure are shown in Table 2. These sizes were selected to comply with wind drift limits shown in Table 1. The fundamental period of the structure is 3.8 seconds. The numerical investigation included the first three modes of vibration. The combined modal mass participation of the first three modes adds up to 95.1% of the building's total mass.

Table 1: Building design parameters

Location	Corpus Christi, Texas
Risk category	III
Exposure type	B
Dead load	120 psf
Live load	50 psf
Wind event	50-year event
Design wind speed	110 mph
Story Drift Ratio	$\leq 1/300$

Table 2: Designed cross sections of the members in the moment frame

Member	Size
Beams	W 18x130
Columns 1st-5th	W 14x233
Columns 6th-10th	W 14x193
Columns 11th-15th	W 14x176
Columns 16th-20th	W 14x145

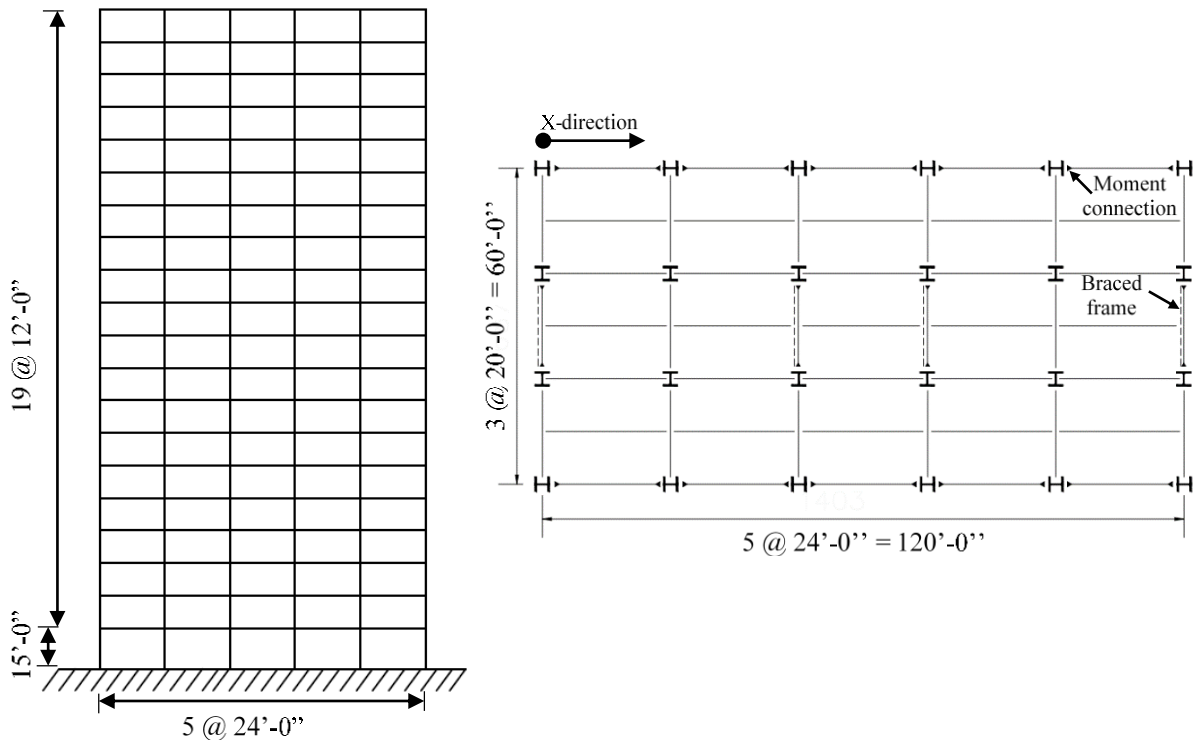


Figure 1: Typical X-direction elevation and floor plan of the 20-story building structure

3.3.2. Wind load simulation

To generate realistic nonstationary wind forces applied to the 20-story building, the two components of the wind force, low-frequency (pseudo-static) load and high-frequency (fluctuating) load were simulated separately. The high-frequency load was generated through a numerical procedure that uses a velocity spectrum [123]. Twenty different wind velocity records (one per story) with different frequency characteristics were generated. The low-frequency part was extracted from real-world field measurements exhibiting varying mean wind speed. The low-frequency load for each floor was scaled following the power-law relationship of the wind profile. The total wind load for the numerical model is the summation of these two parts (see Figure 2). The ratio between the amplitudes of the low-frequency and high-frequency components in the total wind force was determined based on the observation from field measurements.

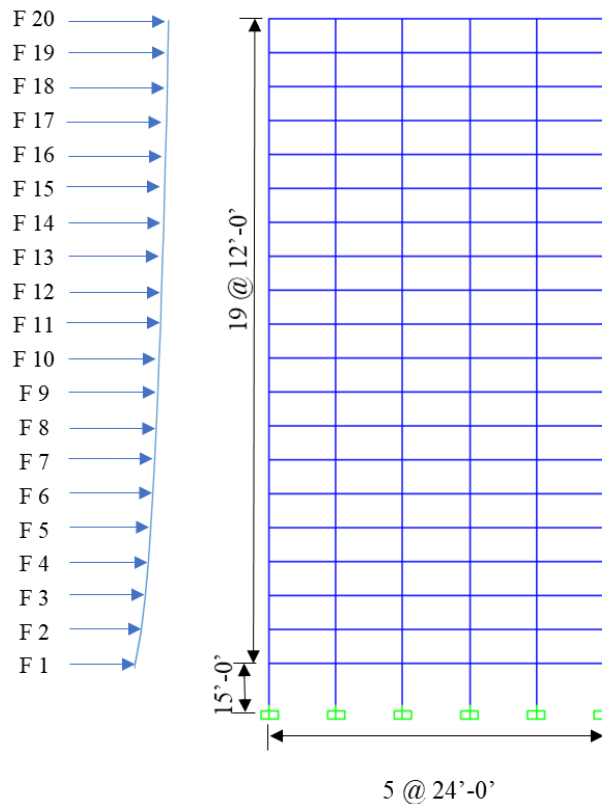


Figure 2: Generated wind load forces profile for the SAP2000 model

3.3.3. Numerical results

The numerical model of the 20-story structure presented in section 3.3.1 is used to validate the proposed methods. The generated wind loads in section 3.3.2 are used as input forces to the numerical model applied to each story. The lateral drift of each story is then estimated using the two proposed methods.

Noises were added to the simulated measurements and mode shapes to account for the measurement noise and uncertainty in mode shape identification. The simulated acceleration and strain responses were subjected to a 20% zero-mean Gaussian noise (RMS amplitude). The mode shapes, including the displacement and strain mode shapes, were also subjected to a 20% noise. The roof displacements were estimated with three methods: acceleration only, data fusion method A, and data fusion method B. These estimates and the full reference record are shown in Figure 3 (a), with a partial record shown in Figure 3 (b).

To quantify the error of the results in Figure 3, the frequency domain error (FDE) index [37] was evaluated. The FDE index varies between 0 and 1, with 0 indicating no error. The FDE index accounts for both the amplitude error and the phase error between two signals (estimated versus reference). The FDE index for the estimated displacements using the proposed methods compared with the reference roof displacement from SAP2000 are shown in Table 3. The errors of the displacements obtained using the proposed methods (for the period of 35 seconds shown in Figure 3b) are small compared to the acceleration-only method, especially when we consider the relatively high noise ratio in the measurements and mode shapes.

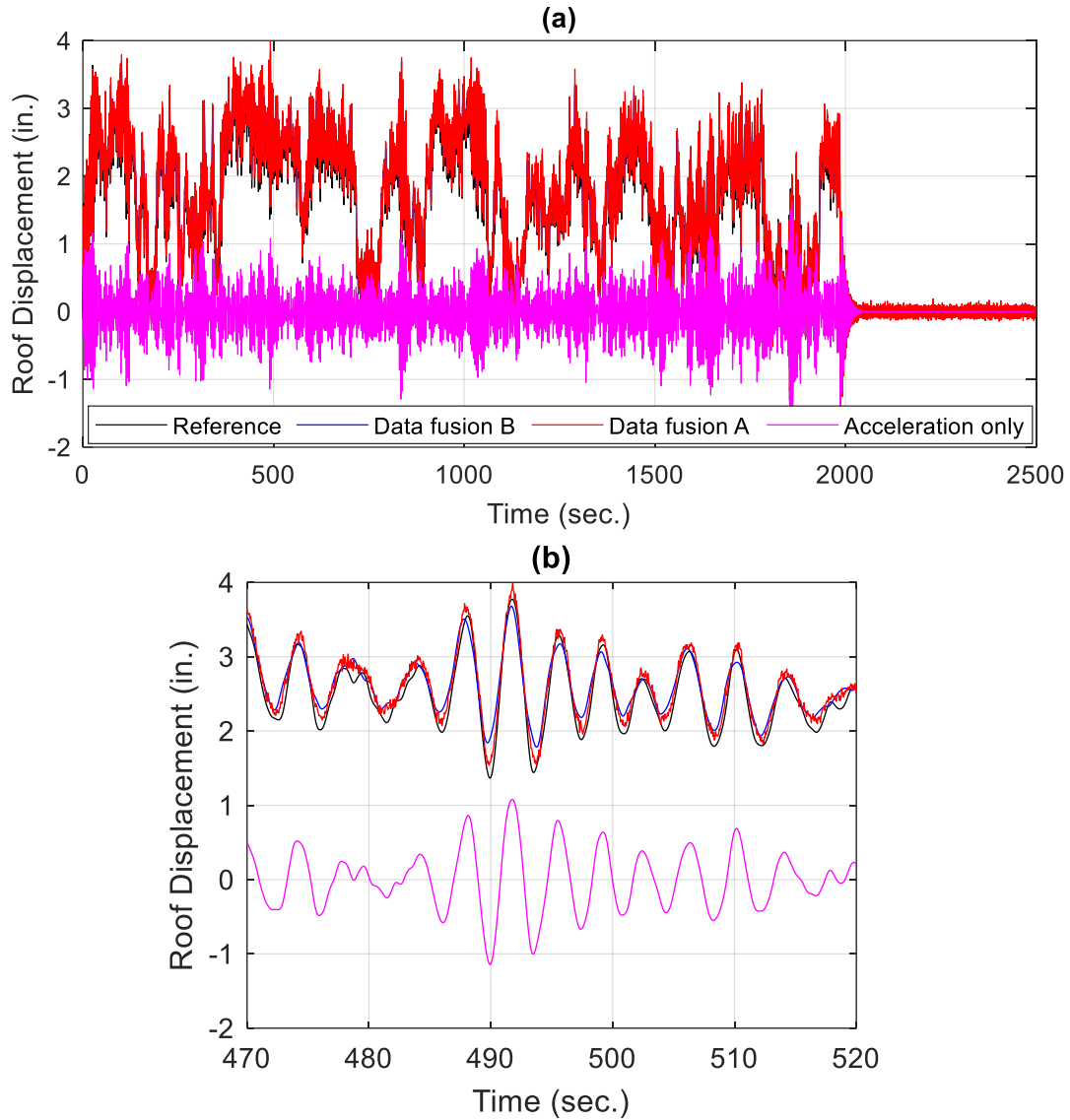


Figure 3: Comparison of building drift estimates using various methods: (a) Full record (b) Partial record

Table 3: Peak error and FDE for the estimated displacement

Measurements type	Peak displacements (in.)	Error in the peak displacement	FDE-Amp.	FDE-Phase	FDE-Total
Acceleration only	1.62	-57%	69.7%	4.1%	73.8%
Data fusion A	3.99	+5.6%	4.9%	2.1%	7.0%
Data fusion B	3.68	-2.5%	4.2%	1.1%	5.3%
Reference (SAP2000)	3.77	Reference			

The data fusion method B showed noticeable improvement in terms of amplitude and phase errors in comparison with the data fusion method A. However, it is important to notice the difference in complexity and computational time between the two proposed methods. The data fusion method A is a strain-based method with a scaling factor obtained from acceleration, and it does not involve a moving-time window. However, the data fusion method B uses both acceleration and strain measurements, and it requires the application of a moving-time window.

3.4. Experimental investigation

3.4.1. Model description and test setup (small-scale 6-story structure)

For the experimental investigation of this study, a small-scale 6-story steel structure is used. The structure is assembled by angles, bolts, and nuts. The structure has a total height of 74.25 inches with a one-foot typical story height and a total weight of 267 pounds (Figure 4). The structure is excited using two large fans simulating wind load (see Figure 5).

Acceleration measurements are collected using seven accelerometers, one per story in addition to the ground level. The strain measurements are also collected using six strain gauges, one per story, as shown in Figure 5. The acceleration and strain measurements are sampled at 2048 Hz and then downsampled to 30 Hz. These measurements are used to calculate the structural displacement using: data fusion method A, data fusion method B, and FIR method (acceleration only). The displacement of the structure is also tracked using computer vision. This tracked displacement is used as a reference for comparison.

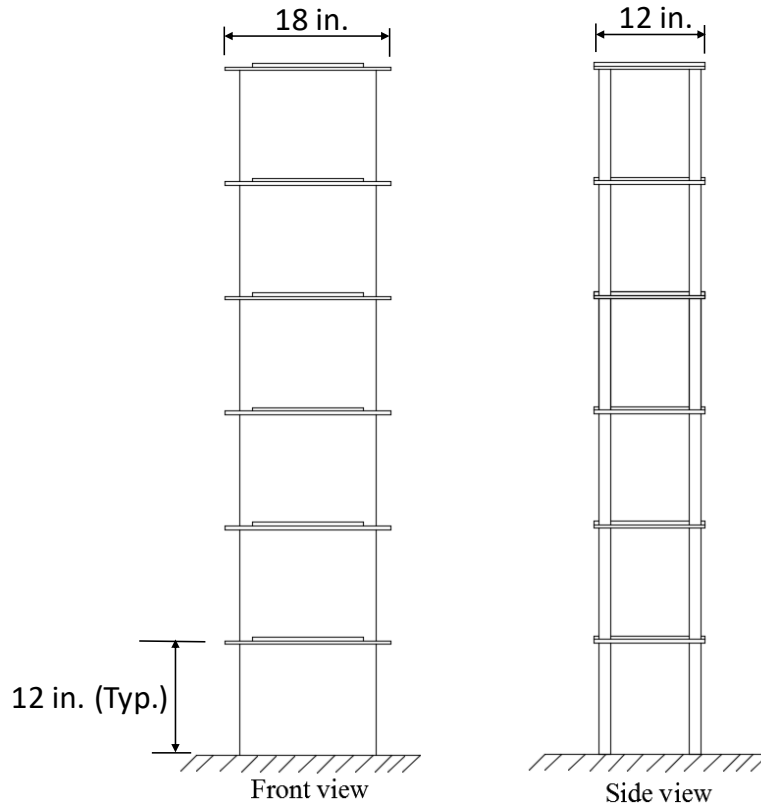


Figure 4: Front and side view of the small-scale 6-story structure

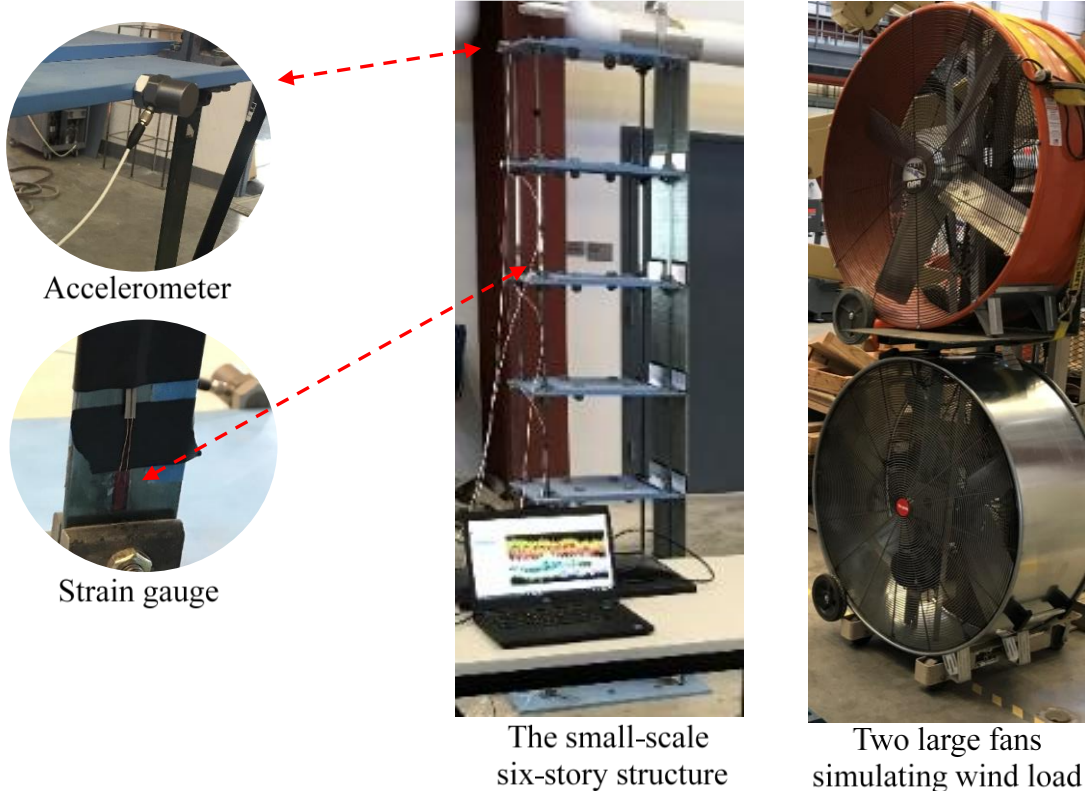


Figure 5: Test setup for the 6-story structure and wind load

3.4.2. Experimental results

This section presents the experimental results from the structure and test setup shown in Figure 5. The measured accelerations from the structure, under the wind load generated by the two fans, are presented in Figure 6. The measured strains are shown in Figure 7, where the maximum strain on the sixth floor is 13 microstrains. The maximum strain on the first floor is 44 microstrains. The measured strains preserved the low-frequency components (the pseudo-static component), which is the motivation of fusion strain with acceleration.

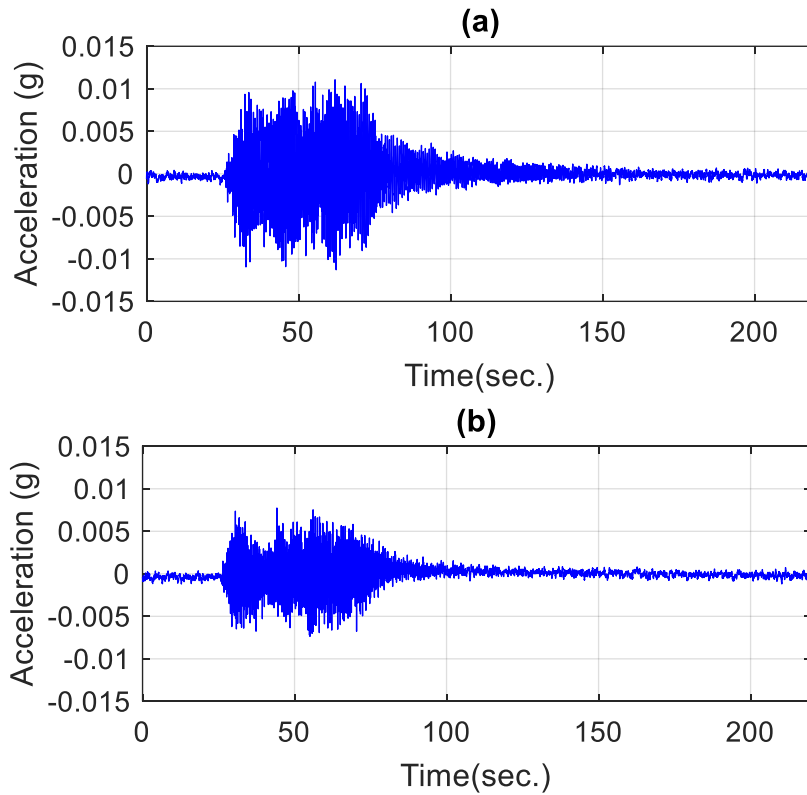


Figure 6: Measured acceleration under wind load: (a) Sixth story (b) First story

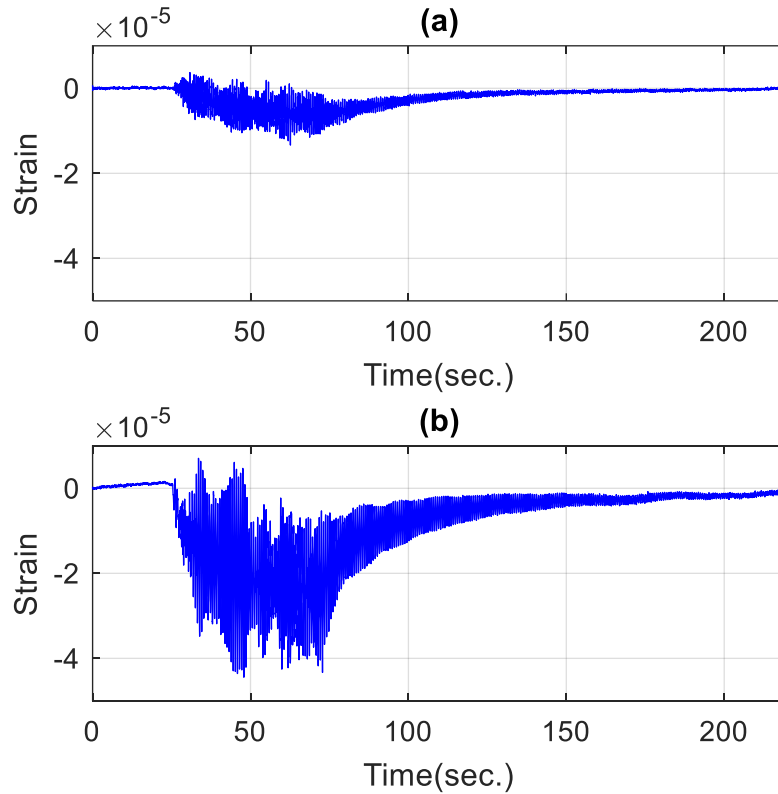


Figure 7: Measure strain under wind load: (a) Sixth story (b) First story

The displacement is estimated using three methods and compared with the reference displacement measured using the KLT tracker (see Figure 8 and Figure 9), which tracks the displacement from a recorded video of the structure. The KLT tracker is discussed in detail in sections 2.3 and 4.2.1. Even though the wind load generated by the two fans is relatively small due to their power limitations, the measured reference displacement still shows clear dynamic and pseudo-static components.

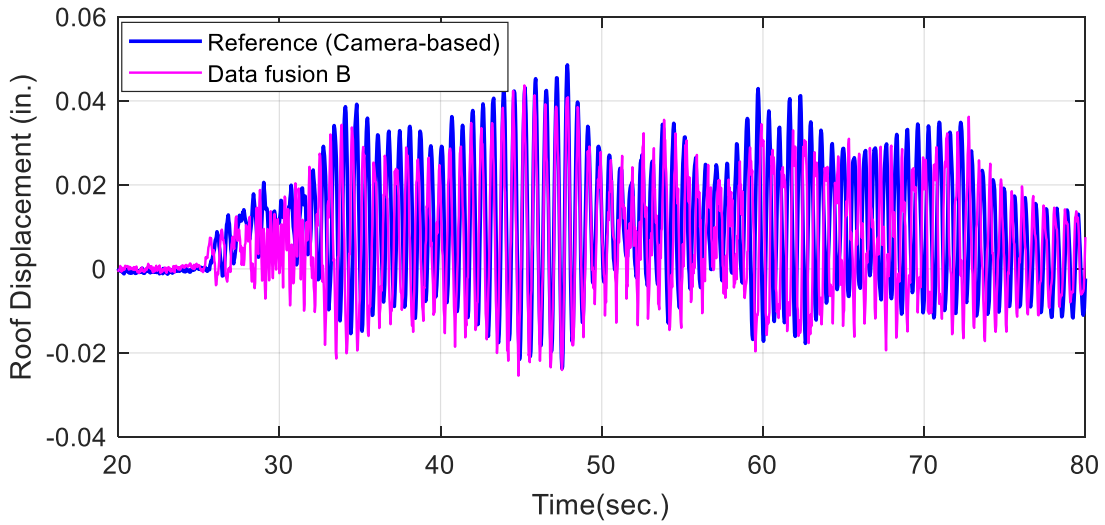
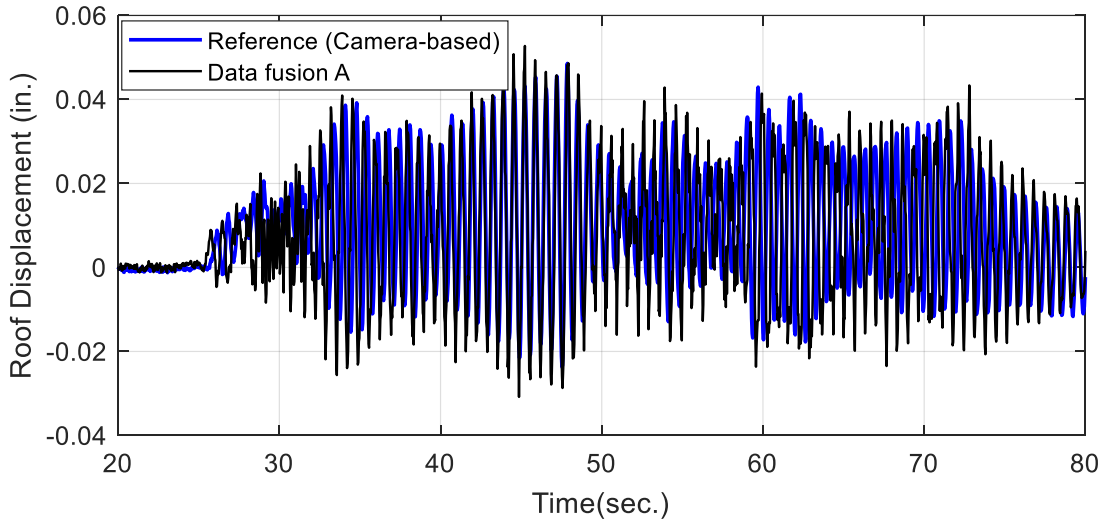
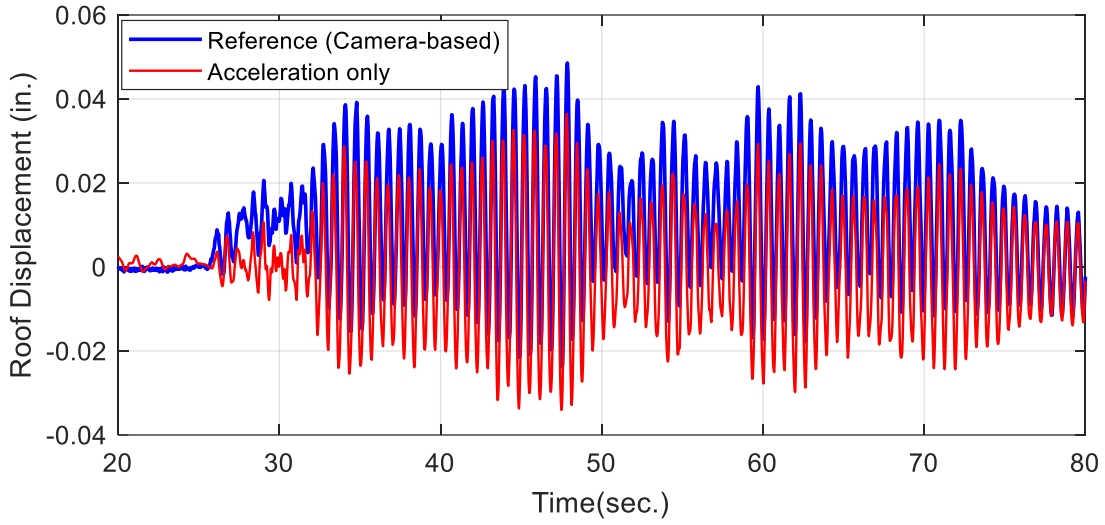


Figure 8: Comparison of the roof displacement using various methods

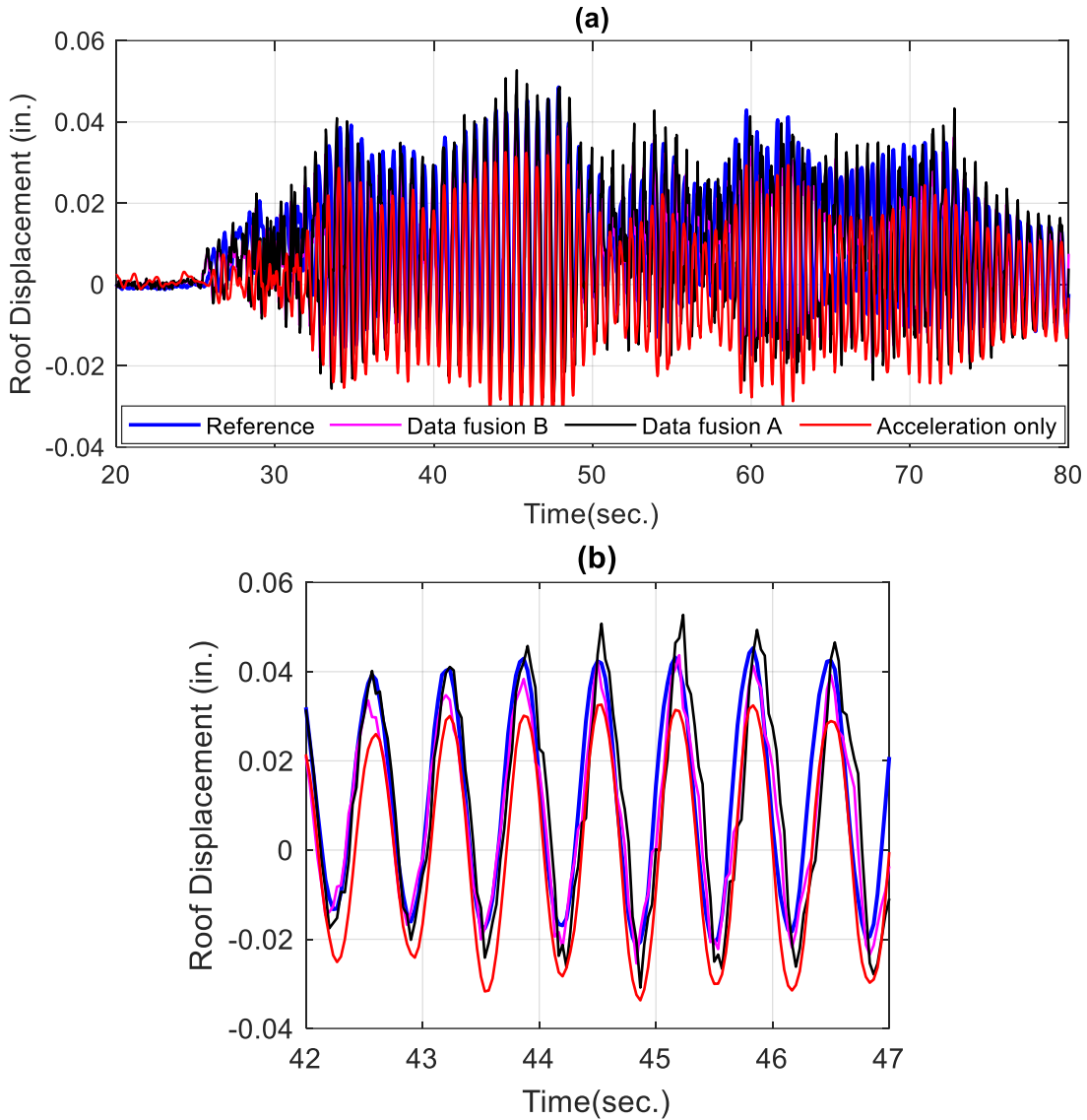


Figure 9: Comparison of the roof displacement using various methods: (a) Full record (b) Partial record

The estimated displacements from the proposed methods clearly provide higher accuracy than using acceleration only. The errors in the estimated displacement from the three methods are presented in Table 4. These results confirm the validity of the proposed data fusion methods. The error in the estimated displacement from acceleration could be much larger if the wind load was larger than the used load. The contribution of the pseudo-static part to the total displacement is directly affected by the input wind load level.

Table 4: Peak error and FDE for the estimated displacements

Measurements type	Peak displacements (in.)	Error in the peak displacement	FDE-Amp.	FDE-Phase	FDE-Total
Acceleration only	0.0365	- 25%	20.4%	9.1%	29.5%
Data fusion A	0.0527	+ 8%	10.2%	16.4%	26.6%
Data fusion B	0.0437	-10%	12.8%	7.3%	20.1%
Camera-based	0.0486	Reference			

3.5. Summary

Two methods (data fusion A and data fusion B) were presented to provide reliable displacement estimation from acceleration and strain measurements. The proposed methods were able to estimate dynamic structural displacements (including a pseudo-static component) using acceleration and strain measurements. In particular, the proposed methods do not require mass-normalized mode shapes to calculate displacements from strains. Instead, the mode shapes were normalized to have a maximum value equal to one, and a scaling factor calculated from acceleration measurements was adopted to achieve appropriate modal participation.

The effectiveness of the proposed methods was proved numerically and experimentally. The numerical investigation used a numerical model of a 20-story steel moment frame structure. Both measurements noise and mode shape noise were applied in the numerical investigation. The experimental investigation used a small-scale 6-story structure with input load from two large fans. The measured acceleration and strains were used to calculate the displacement using the two proposed methods. The numerical and experimental investigations prove the effectiveness of data fusion in estimating the structural displacement of buildings subjected to non-stationary wind load. Estimating buildings' floor displacement subjected to non-stationary wind loading using acceleration only is insufficient and could lead to large error.

CHAPTER 4: SYSTEM IDENTIFICATION USING COMPUTER VISION

4.1. Introduction and Background

System identification is an essential tool to establish a solution for a wide range of problems in structural health monitoring (SHM). For example, system identification is needed for damage identification, structural control, structural fragility analysis, and design validation. System identification through experimental modal analysis uses dynamic measurements from a structure to build a representative mathematical model. Experimental modal analysis is a significant application of system identification, which identifies the dynamic characteristics of structures (i.e., natural frequencies, mode shapes).

System identification can be performed based on different types of dynamic measurements, such as acceleration and displacement. In particular, acceleration measurements measured using accelerometers are more commonly applied in system identification than other types of measurements, such as displacement measurements. Accelerations are more commonly acquired compared with displacements due to several advantages of accelerometers, such as their sensitivity to high frequencies, and they do not have the need for a fixed reference point. However, accelerometers require physical contact with the structure, which may require intensive labors for installation, and it reduces the effectiveness of the accelerometers in terms of cost. Also, each accelerometer can only measure a limited number of degrees of freedom (DOFs). As a result, system identification for large-scale structures using accelerometers may require many sensors to be attached to the structure.

On the other hand, displacement measurements such as those from the GPS is less common in system identification. The main limitations of using the GPS are the requirement for physical

contact and the limited number of measured degrees of freedom (similar to the accelerometers). Besides, the GPS provides a relatively low sampling rate when compared to accelerometers. Furthermore, the accuracy of the displacement from a single GPS receiver is inferior. The GPS's accuracy is commonly improved using the differential-GPS (DGPS) technique, which requires an additional receiver instrument at a fixed reference point [63, 80].

Displacement measurements are known for their low sensitivity to high frequencies when compared to acceleration measurements. This low sensitivity affects the identification of the higher order modes when using the displacement measurements. The following section highlights the difference between computer vision—which measure displacement—and traditional sensors such as accelerometers.

4.1.1. Traditional sensors vs. computer vision

System identification using computer vision is an active field in structural health monitoring because it overcomes some of the limitations of traditional sensors. For example, computer vision can simultaneously monitor many degrees of freedom, and each pixel in a frame might be monitored. However, traditional sensors, such as accelerometers, are limited to measuring the motion at the sensor location. Furthermore, the feature-based (target-free) techniques have the significant advantage of avoiding any physical contact with the monitored structure. These unique advantages, along with the cost-effectiveness, provide the potential for computer vision in SHM.

However, there is a lack of studies investigating the use of computer vision in system identification compared to traditional sensors. Moreover, many of the available studies on using computer vision for system identification used special procedures, i.e., professional high-speed cameras or special lighting conditions. Other studies also used experimental structures with

impractical large motion, which might be unrealistic or unachievable under operational loads. These special procedures limit the applicability of computer vision in system identification for real structures.

For real structures, the level of displacement due to operational loads (i.e., ambient vibration) is usually small. The small displacement means a low signal-to-noise ratio, making the system identification using computer vision more challenging under operational loads. This study examines the ability of computer vision in system identification using consumer-level cameras (i.e., smartphones' cameras) and for motions with small displacements. The use of consumer-level cameras combined with realistic displacement levels increases the applicability of computer vision in system identification for real structures.

This study proposes a framework that uses consumer-level cameras and relies on small structural displacement motions. In addition to modal frequency identification, the proposed framework provides two strategies to identify mode shapes, discussed with details in 4.2.3. The accuracy of identified parameters using computer vision is affected by several factors, which include the process of video recording and the post-processing steps. In the proposed framework, the essential guidelines for each step are discussed in detail. The effectiveness of the proposed framework is validated experimentally using two structures: a small-scale 6-story shear building and an experimental truss bridge, as shown in 4.3.

4.2. Methodology

The proposed framework adopts the KLT tracker [75, 103, 117], discussed with more details in sections 2.3 and 4.2.1, to extract structural displacements from recorded videos. In addition, the proposed framework adopted the phase-based motion processing PBMP [121] to magnify small motions to enhance the accuracy of mode shape identification for weakly excited modes. In this

study, the frequencies of structures are obtained using tracked displacements from the KLT tracker. The proposed framework provides two strategies to extract the mode shapes; the first option uses the displacement records obtained from the KLT tracker. The second option extracts the mode shapes from a series of processed videos that involve the PBMP. The details of the proposed framework are discussed in 4.2.3.

4.2.1. **Kanade-Lucas-Tomasi (KLT) feature tracker**

In 1981, Lucas and Kanade proposed an iterative method that makes image registration faster than traditional methods [75]. This method approximates the second derivative of an image to reduce the computational time. Tomasi and Kanade adopted this method in 1991, and proposed a way to track features in the images that are suitable for their tracking algorithm [117]. Tomasi and Kanade's method selects feature points based on a defined threshold for the gradient matrix and eigenvalues. These two papers yielded the well-known Kanade-Lucas-Tomasi (KLT) tracker. In 1994, Shi and Tomasi proposed a method to examine the quality of the tracked feature points in the KLT tracker [103]. The quality of feature points is determined by measuring feature dissimilarity between the current frame and the reference frame.

The KLT tracker is adopted in this study to monitor structural displacements. The KLT tracker identifies the feature points in the user-defined region of interest (ROI). The displacement of these feature points is tracked using their coordinates in each frame (see Figure 10). The tracked displacements are then used to estimate the natural frequencies and mode shapes of the structure. However, the tracked displacements might not provide adequate accuracy for estimating the mode shapes due to low signal-to-noise ratio. An alternative is to estimate the mode shapes from magnified videos, which is Option B as a part of the proposed framework. The adopted method for motion magnification is discussed in section 4.2.2.

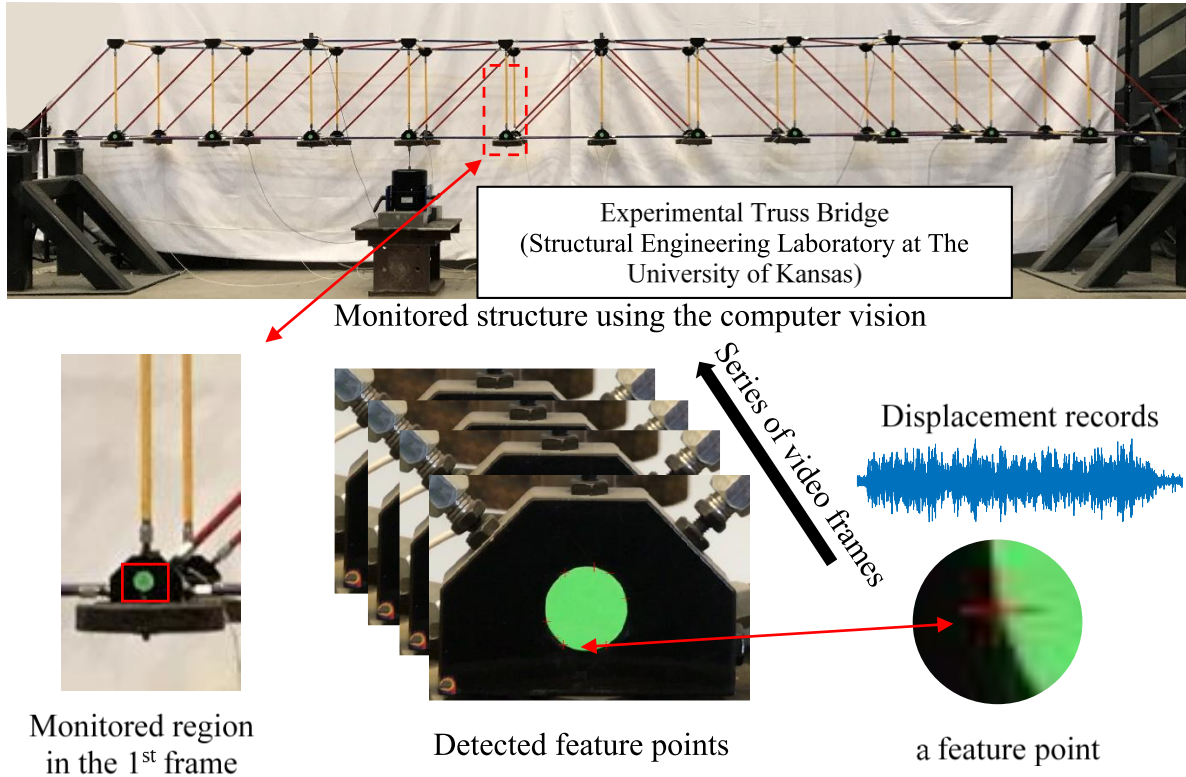


Figure 10: Displacement tracking using the KLT

4.2.2. Phase-based video motion processing (PBMP) method

The Phase-Based Video Motion Processing (PBMP) method was proposed in 2013 [121]. This method can magnify small motions in videos and attenuate unwanted ones without a significant amplification of noise. The PBMP method is based on processing the video in complex-valued pyramids [105]. In the PBMP method, the motion is manipulated by amplifying or attenuating the complex steerable pyramids' local phase variations over time using temporal filtering.

Wadhwa et al. also compared the results of the PBMP with the Linear Eulerian Video Magnification (LEM) method [127]. The PBMP can support about four times larger magnification factor than the LEM. Besides, the PBMP showed much less sensitivity to noise when compared to the LEM. The PBMP method translates (shifts) the noise rather than the LEM, where the noise is amplified linearly [121].

In the PBMP method, each frame in the input video passes through different steps summarized in Figure 11. The decomposition in step (a) uses the complex steerable pyramids, which are shown as cropped filters. Then the amplitudes (b) and the phases (c) are separated. The phases in (c) are the temporally filtered phase variation that is used for magnification and attenuation in step (d). The magnified video is then reconstructed in step (e) using the magnified phases in (c) along with all other components (see Figure 11). The PBMP is adopted in the proposed framework to improve mode shape estimation.

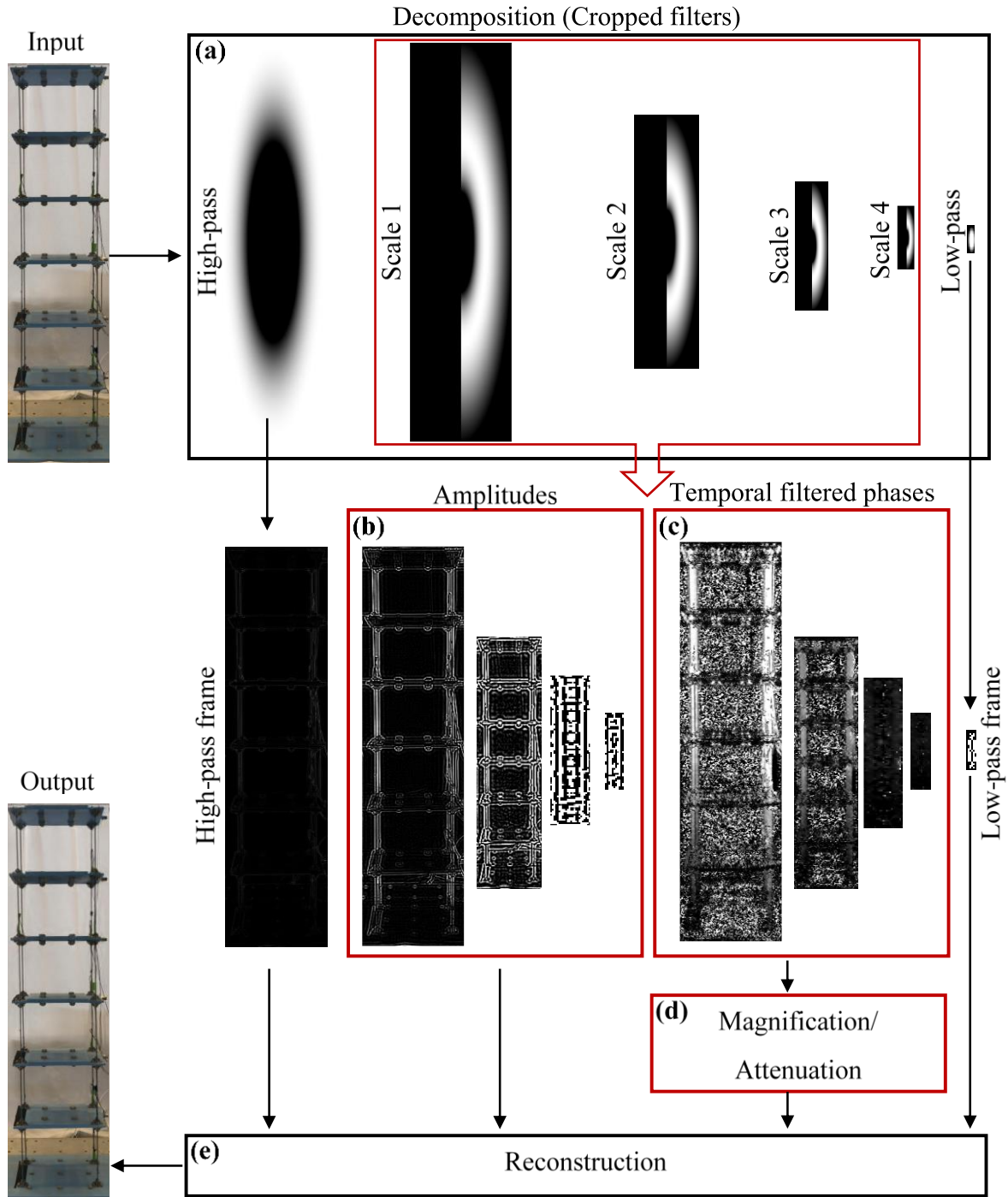


Figure 11: Processes of the phase-based motion processing (PBMP)

4.2.3. Proposed framework

The proposed framework has four main steps, as shown in Figure 12. The processes start by inputting a recorded video of the structural response. The second step performs displacement tracking from the video using the KLT method. The third step is to obtain the natural frequencies

using the Eigensystem Realization Algorithm (ERA) method [61] and the KLT tracked displacements. The fourth step is to obtain mode shapes using displacement records, which has two options. In Option A, the mode shapes are extracted using the ERA from the displacement measurements obtained in the second step. In Option B, the mode shapes are extracted using magnified videos, in which each video is processed to contain a single mode of interest. The proposed method adopted the original open-source MATLAB code for the PBMP method [121]. The processes of magnifying the videos are shown in Figure 13, which is accomplished by magnifying the video within the frequency range of the mode of interest while attenuating all other frequency components.

The accuracy of system identification using computer vision is affected by several factors. Some of these factors are unavoidable, such as the fact that civil infrastructures are designed to have small motions under operational loads. However, other factors that affect the accuracy of the system identification can be overcome. For example, the processes of recording and post-processing the videos greatly impact the accuracy of the identified modal parameters. This study presents general guidelines and recommendations for recording and processing videos for modal identification.

The process of recording the input video should consider the following (for step 1):

- Adequate resolution should be used that can provide an acceptable signal-to-noise ratio of the tracked displacements. In general, the highest available resolution is desirable. However, high resolution has a higher noise level, which might affect identifying higher modes more than lower modes.
- An adequate sampling rate should be used that can cover the bandwidth of interest and to avoid temporal-aliasing. Even though consumer-level cameras support a much lower

sampling rate (e.g., 30 fps) than traditional sensors, it can still provide an adequate sampling rate for many civil infrastructures.

- Digital cameras such as the ones on smartphones usually support different options of video formats, such as the High-Efficiency Video Coding (HEVC) format and the Most Compatible format. The HEVC option reduced the consumed storage size significantly. However, it generally affects the quality of the video. Furthermore, the HEVC format requires a much longer time in importing the video to the computer because the device changes the format to a compatible format while importing the video. The HEVC format could also result in several error messages about device connection, especially for large videos. It is recommended to use the Most Compatible format option even though it will result in a larger storage size.
- Videos should be recorded during stable lighting conditions. Sudden changes in lighting conditions have a significant effect on the accuracy of the tracked displacements using the KLT. By considering the range of the frequency of civil structures and the sampling rate of consumer-level cameras, the adequate recording duration might range from a few to several minutes. For this relatively short duration of recording, the stability of light conditions should not be challenging for field applications.
- The auto-exposure/autofocus lock (AE/AF-L) should be activated when using an iPhone or other devices that have this feature. A rapid change in exposure or focus during the recording might induce a large error in the output displacements.
- The monitored regions should have distinct local features (i.e., a point and an edge). These features are necessary to successfully apply the KLT. Examples of local features usually available naturally in structures are exposed screws, edges, angles, or distinct color patterns.

- The camera should be set up perpendicular to the monitored regions as much as possible. An ideal camera setup might eliminate the need for the calibration process due to image distortion.
- Physical dimensions of the monitored structural members in the video should be known to be used for calibration if needed. The calibration is applied by converting the unit of the tracked displacements from pixels to a physical unit.

When applying the KLT tracker to videos (steps 2 and 4), the following details and parameters should be considered:

- Cropping the video before processing to cover the regions of interest reduces the computational time of processing.
- When tracking multiple objects in one video, it is more efficient to apply the KLT at once using multi-regional tracking instead of running the KLT algorithm multiple times for each region individually. Multi-regional tracking will significantly reduce the time cost.
- Using the average of multiple feature points from the same rigid object might improve the accuracy of tracked displacements.
- The KLT tracker in MATLAB allows the user to specify the maximum allowable bidirectional error (forward-backward error). Allowing a range of 1% to 5% bidirectional error of the peak displacement should result in reasonable outputs. Using extremely small allowable bidirectional error might result in preventing the tracker from computing the displacements.
- The block size (the size of the neighborhood) and the maximum number of iterations should be appropriately selected; thus, the default values might not be sufficient for some

applications. The block size should not exceed the size of the area covered by the monitored object.

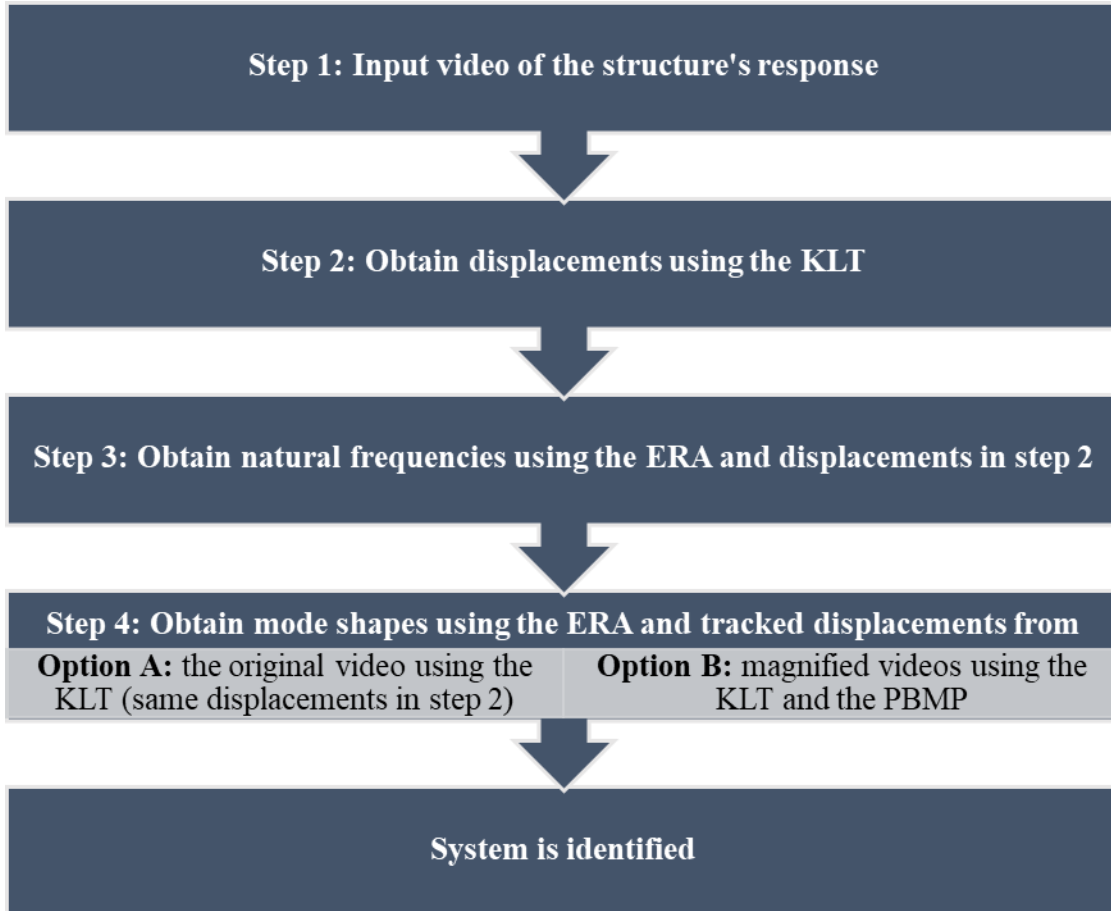


Figure 12: Proposed framework for system identification using computer vision

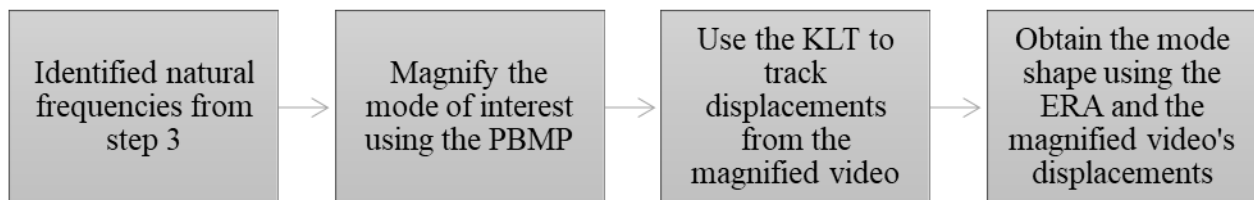


Figure 13: The process of obtaining mode shapes using Option B shown in Figure 12

In the fourth step of the proposed framework, the Option B to obtain the mode shapes applies the phase-based motion processing (PBMP) to magnify modes of interest individually, which will result in one magnified video for each mode. Applying the magnification to a wide

frequency range that contains multiple modes will result in a poor-quality video, which cannot be used for system identification.

For efficiency, it is recommended to attenuate all other frequencies outside the frequency range of interest. The combination of magnification and attenuation eliminates the need to use a large magnification factor for higher modes. This process allows the mode of interest to dominate the response in the magnified video, which will then clearly improve the accuracy of the output. However, the use of attenuation might induce a large noise level in some cases; this includes a moving object with a large motion before the magnification. In such cases, the PBMP algorithm will induce large noise around the moving edges during the process of attenuating the motion of this object. In this case, the magnification of the mode of interest should be performed without attenuation.

The use of Option B might not be required in some cases, especially when identifying lower modes from measurements that have a high signal-to-noise ratio. In this case, the frequencies and mode shapes can be obtained directly from displacements obtained using Option A. The need to use Option A or Option B can be determined based on engineering judgment by evaluating the output displacements from the KLT.

When applying the PBMP (step 4 Option B only), the following details might be considered:

- Smoothing the video should be avoided by setting zero value to the smoothing factor, as it could lead to combining pixels motion that results in inaccurate motion estimation.
- The PBMP allows the user to scale down large videos, which reduces the resolution of the video. Reducing the resolution impacts the accuracy; it is recommended to use the full available resolution without scaling. Note that using full resolution without scaling

will consume a large part of the computer RAM and increase the computation time significantly.

- The PBMP allows three different complex-valued steerable image pyramids: octave (shortest computational time), half-octave, and quarter-octave (longest computational time). In this study, the half-octave pyramid was used with a negligible difference in accuracy compared to that of the quarter-octave. The octave pyramid is very effective in terms of computational time. However, it supports smaller magnification factors than the other two pyramids, which was insufficient for some of the investigated cases in this study.
- For a quick start, the user can use a concise duration (a few seconds might be adequate) of the recorded video to visualize the magnified mode shapes. In this case, it is recommended to use video scaling combined with octave complex pyramids, which will reduce the computational time significantly.
- The PBMP can support a relatively large magnification factor compared with other magnification methods (e.g., LEM method); however, using a too large amplification factor could lead to unstable results. The maximum allowable magnification factor is determined based on several parameters, such as the type of selected complex-valued steerable image pyramids, the magnified frequency range, resolution, and others [121].

4.3. Experimental Investigation

This section presents the experimental investigation of the proposed framework using two structures: a small-scale 6-story structure discussed in 4.3.1 and an experimental truss bridge discussed in 4.3.2. The experimental results from both structures validated the robustness of the

proposed framework and show the great potential of using computer vision for system identification.

4.3.1. Small-scale 6-story structure

4.3.1.1. Model description and test setup

The experimental investigation of this study used the small-scale 6-story steel structure discussed in 3.4.1. The structure is attached to a shake table in the West Campus Structural Laboratory at The University of Kansas, as shown in Figure 14. The structure is subjected to Band-Limited White Noise (BLWN) excitation using the shake table.

System identification is performed using computer vision following the proposed framework in 4.2.3. The response of the structure is video recorded using an iPhone 7, which is used as an input to the proposed framework. The iPhone is placed 8 feet away from the building structure. The video is recorded using two resolution options: 1080p with 120 frames per second (fps) for the first experiment, and 4K (2160p) with 30 fps for the second experiment. For iPhone 7, the option of 1080p with 120 fps is only available as a slow-motion recording. The slow-motion affects only the display of the video on the iPhone. The slow-motion video is exported as a regular-motion video to the computer.

Acceleration measurements are also collected using seven accelerometers, one per story in addition to the ground level. The acceleration measurements are sampled at 2048 Hz and then downsampled to 30 Hz. The system identification results obtained from the accelerometers are compared with those obtained from computer vision. The results and comparisons are presented in the following section 4.3.1.2.

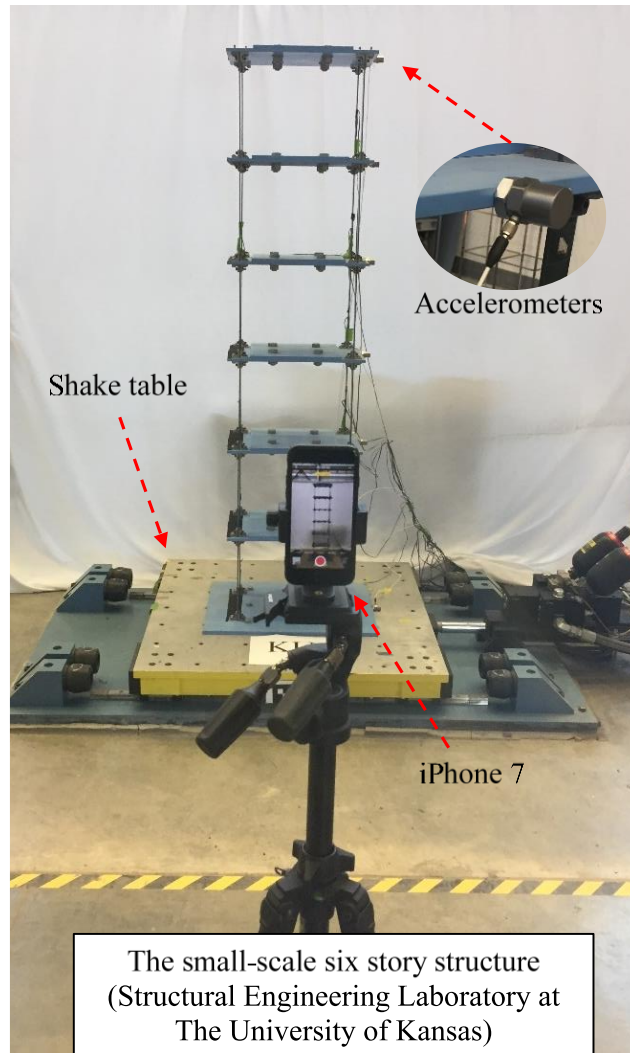


Figure 14: Test setup for the small-scale 6-story structure

4.3.1.2. Experimental results

This section presents the experimental results from the small-scale 6-story structure using the test setup shown in Figure 14. The structure is subjected to BLWN excitation with a wide frequency bandwidth, which can excite the six bending modes of interest that are between 0 and 15 Hz. The results from the two experiments are presented using the two resolution options and compared with results obtained from the accelerometers. In both experiments, the absolute peak displacement of the roof story was 0.22 inches, which is less than 0.3% of the building height. The peak story drift at the roof did not exceed 0.03 inches, corresponding to about a drift ratio of 0.25%.

Experiment 1: 1080p with 120 fps

The first experiment used a resolution of 1080p (1,920-by-1,080 pixels) with 120 fps to record the structural response under band-limited white noise excitation. The tracked displacements using the KLT at each story are shown in Figure 15 (a). These displacement records are downsampled from 120 Hz to 30 Hz, which enhanced the signal-to-noise ratio from 26 decibels (dB) to 28.6 dB. The process of recording and processing the video considered the discussed guidelines in 4.2.3. The displacement record of each story is shown in Figure 15 (a). The power spectral densities (PSDs) of the displacement measurements in Figure 15 (a) are shown in Figure 15 (b). The power spectral densities in Figure 15 (c) are calculated using acceleration converted from displacements measured by computer vision. The acceleration measurements from computer vision are the double derivative of the tracked displacements. The acceleration measurements are more sensitive to high modes when compared to displacement measurements. This difference in sensitivity clarifies the difference in the energy levels of higher modes between Figure 15 (b) and Figure 15 (c). It also gives the potential to use the double derivative of the tracked displacement instead of using the displacement to perform system identification.

The acceleration measurements from the accelerometers are used as reference measurements in this study. The measured acceleration from the accelerometers are shown in Figure 16 (a), and the power spectral densities of these measurements are shown in Figure 16 (b). The average power spectral density (PSD) is shown in Figure 16 (c), which is the weighted average of all the power spectral densities in Figure 16 (b), with the identified six peaks of the bending modes. The third and sixth peaks show a lower energy level when compared to the other four peaks. The identified mode shapes using the accelerometers are shown in Figure 17.

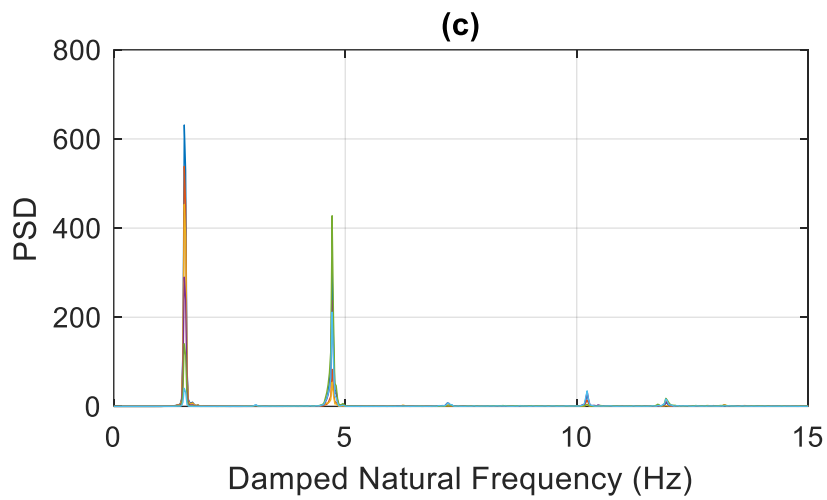
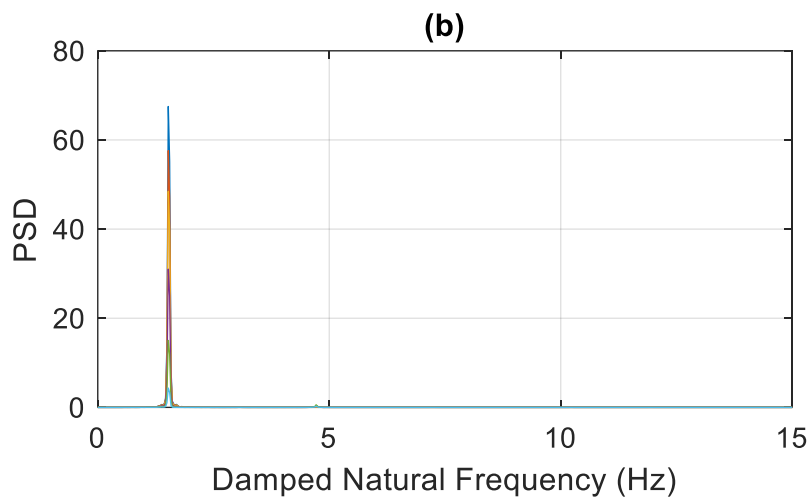
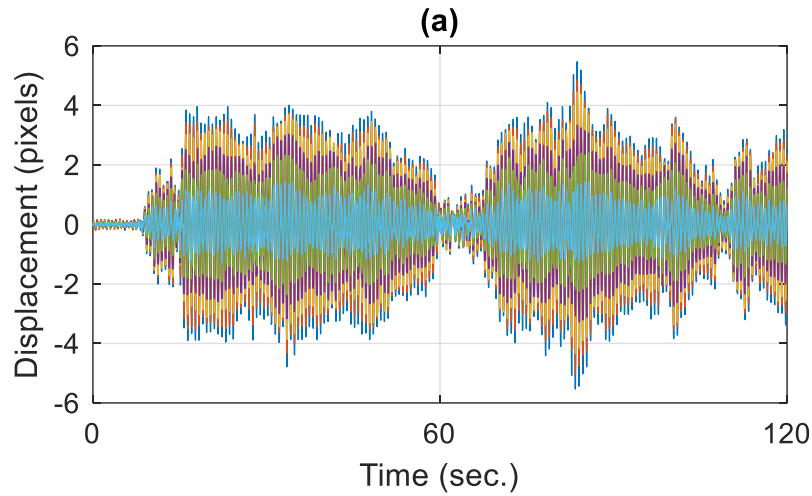


Figure 15: (a) The tracked displacements at each story (the resolution is 1080p with 120 fps, downsampled to 30 Hz). (b) The PSDs of displacement measurements in (a). (c) The PSDs using the double derivative of displacement measurements in (a)

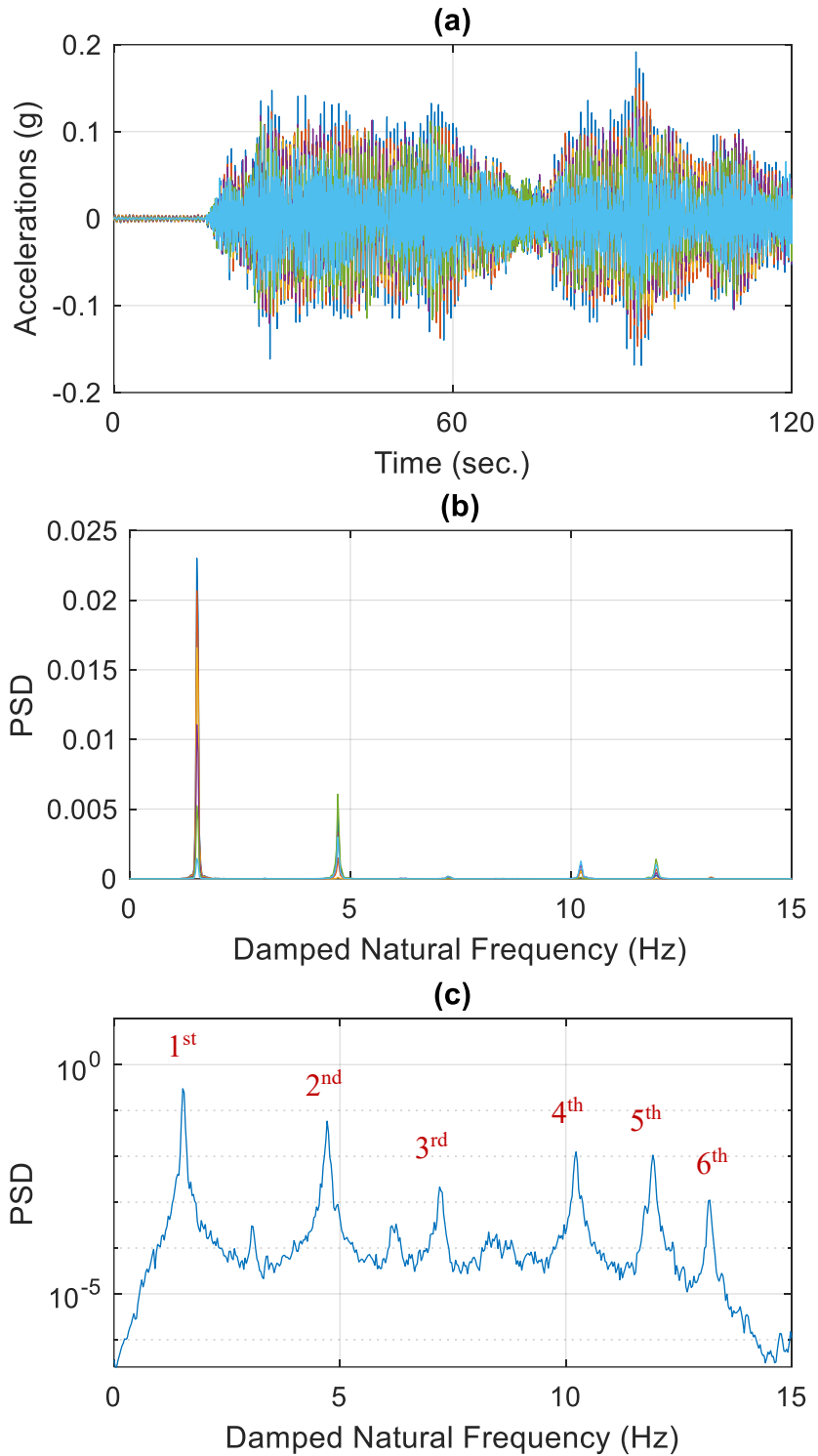


Figure 16: (a) Accelerometers measurements at each story (downsampled to 30 Hz). (b) The PSDs of measurements in (a). (c) The average of PSDs in (b) using a logarithmic scale for the y-axis

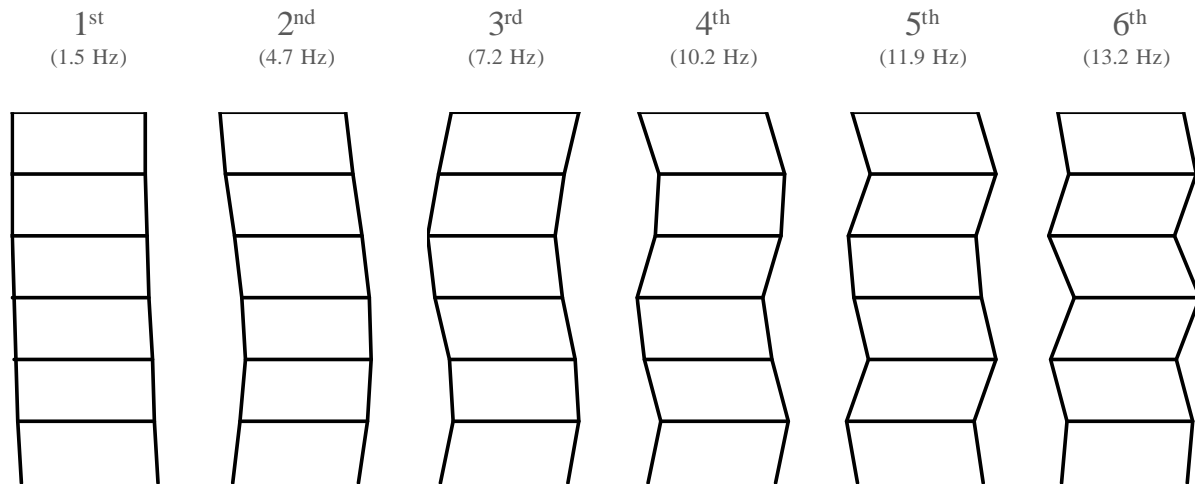


Figure 17: Identified six bending modes of the small-scale 6-story structure using measurements from accelerometers

The average power spectral densities from displacement measurements using computer vision and using accelerometers are shown in Figure 18 (a). The average power spectral densities using the double derivative of displacements from computer vision and accelerometers are presented in Figure 18 (b) and Figure 18 (c). These results prove the ability of the computer vision method to identify the frequency of structures with high accuracy. For the investigated cases in this study, the computer vision results identified all modes except the sixth. The inability to identify the sixth mode is attributed to the fact that computer vision measures the motion as a displacement, which is naturally less sensitive to high modes. Taking the double derivative of the tracked displacements increases the energy level of higher modes and makes them more visible. However, this also amplifies the noise level, which means the acceleration measurements from computer vision will not have the same sensitivity to high modes as the acceleration from the accelerometers.

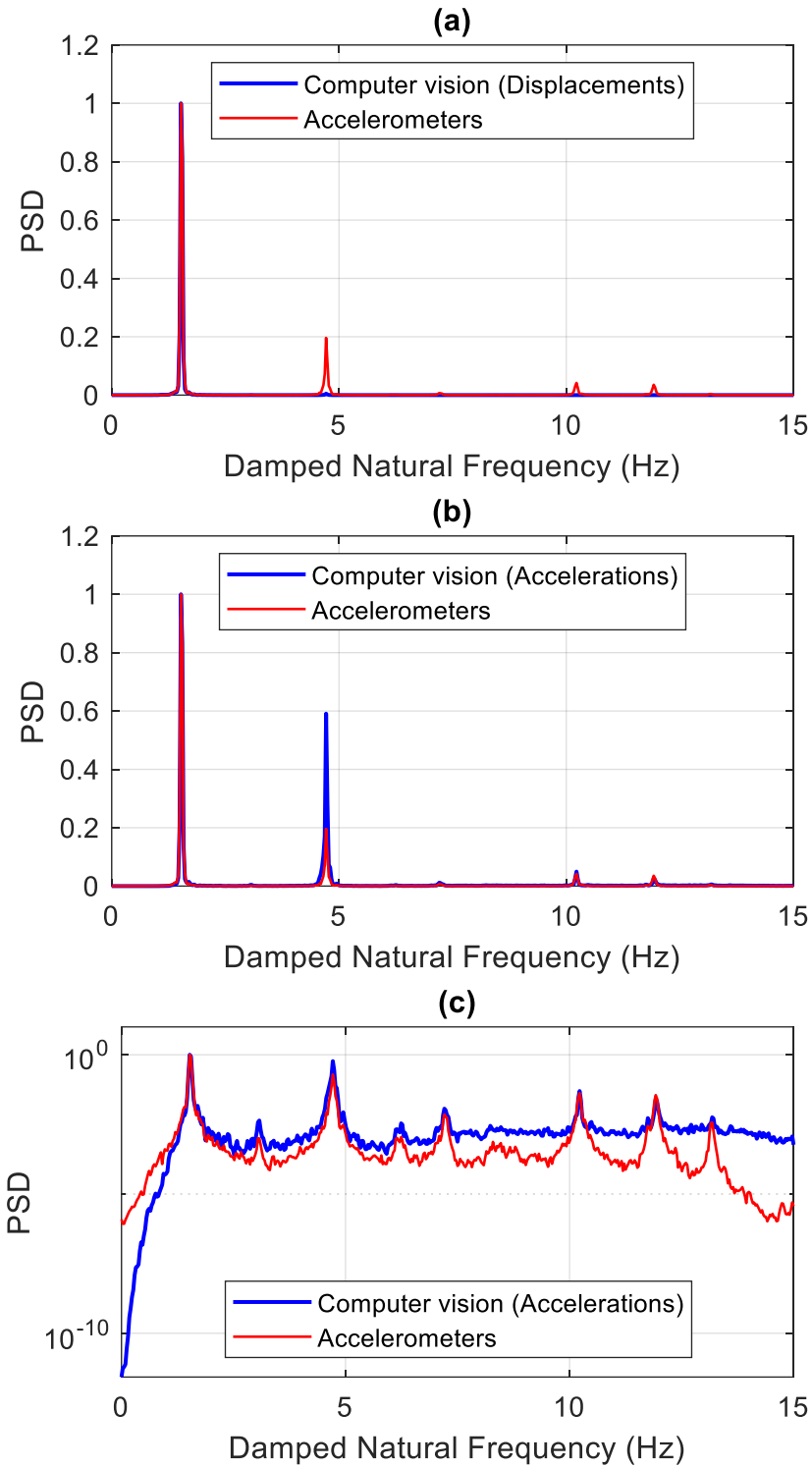


Figure 18: (a) Normalized average PSDs using displacements from computer vision (1080p video used in Figure 15) and accelerations from accelerometers. (b) Normalized average PSDs using accelerations from computer vision and accelerometers measurements. (c) Similar to (b) but using a logarithmic scale for the y-axis

The mode shapes from computer vision using the two options in the proposed framework are shown in Figure 19. The mode shapes from the accelerometers are also shown in Figure 19 and are used as a reference for comparison. The Modal Assurance Criterion (MAC) is a statistical indicator that measures the difference between mode shapes [4], where 100% means a perfect match. The MAC values comparing the mode shapes from accelerometers and computer vision are shown in Table 5.

The estimated mode shapes using Option A show relatively good accuracy, where the MAC values for all modes are more than 96% except the third mode that has a MAC value of 87%. The mode shapes estimated using Option B showed high accuracy for all five modes, with a significant improvement for the third mode, which is a weakly excited mode. The MAC value for the third mode shape increased from 87% in Option A to 95% in Option B. It is important to highlight that Option B might yield slightly lower accuracy for some of the modes that already achieved high accuracy by using Option A. This slight difference is credited to the induced noise by involving the PBMP in Option B.

Option B shows relatively accurate outputs for all modes in the investigated cases. However, Option A shows lower accuracy for the weakly excited mode shapes (i.e., third mode). The author recommends using Option B as the first choice for all modes; however, this option might not be efficient in computational time compared to Option A. An alternative to estimating all mode shapes using Option B is to apply it only to the estimated modes with less accuracy. The Extended Modal Amplitude Coherence (EMAC) value of a mode indicates its consistency in the temporal domain. The EMAC value is commonly used to eliminate modes that show varying consistency, such as weakly excited modes [89]. As a result, the EMAC value of a mode might help to indicate its accuracy. Applying Option B only to those modes with lower accuracy can

significantly reduce computational time and preserve similar accuracy. The EMAC values of the mode shapes are presented in Table 5.

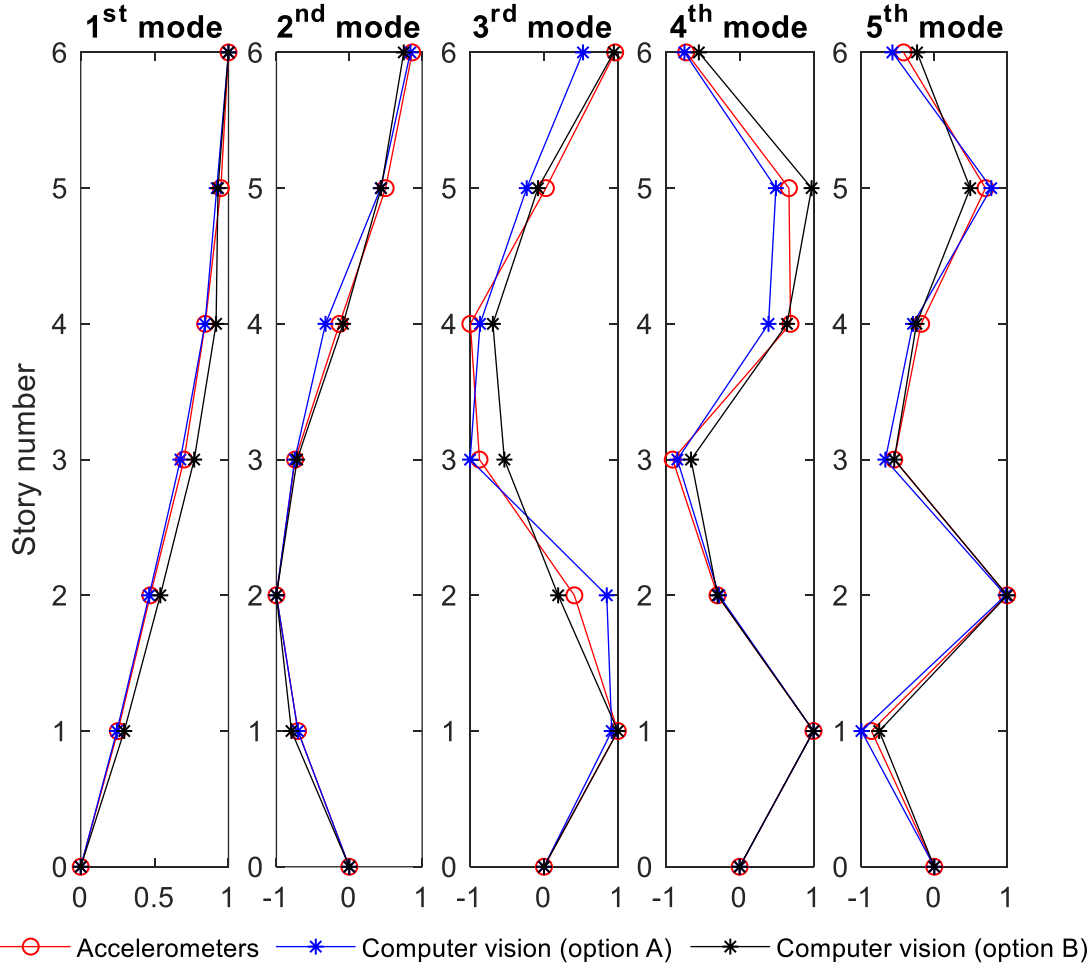


Figure 19: Identified mode shapes using computer vision (1080p video that is used in Figure 15) vs. accelerometers

Table 5: EMAC and MAC values for mode shapes in Figure 19

		1 st mode	2 nd mode	3 rd mode	4 th mode	5 th mode
EMAC values for mode shapes using computer vision		99.83%	98.55%	58.47%	89.29%	79.66%
MAC values for mode shapes obtained using	Option A: KLT only	99.98%	98.63%	87.42%	96.93%	98.76%
	Option B: KLT and PBMP	99.68%	99.11%	94.96%	94.42%	97.32%

Example frames from the magnified videos are shown in Figure 20. Each mode is processed independently by magnifying the frequency range of interest and attenuating other frequencies. In order to enhance the visualization, these videos applied the quarter-octave pyramids, smoothing, and large magnification factors. As a result of magnifying only the frequency of interest and attenuating all other frequencies, the output frames show the mode shape of the magnified mode.

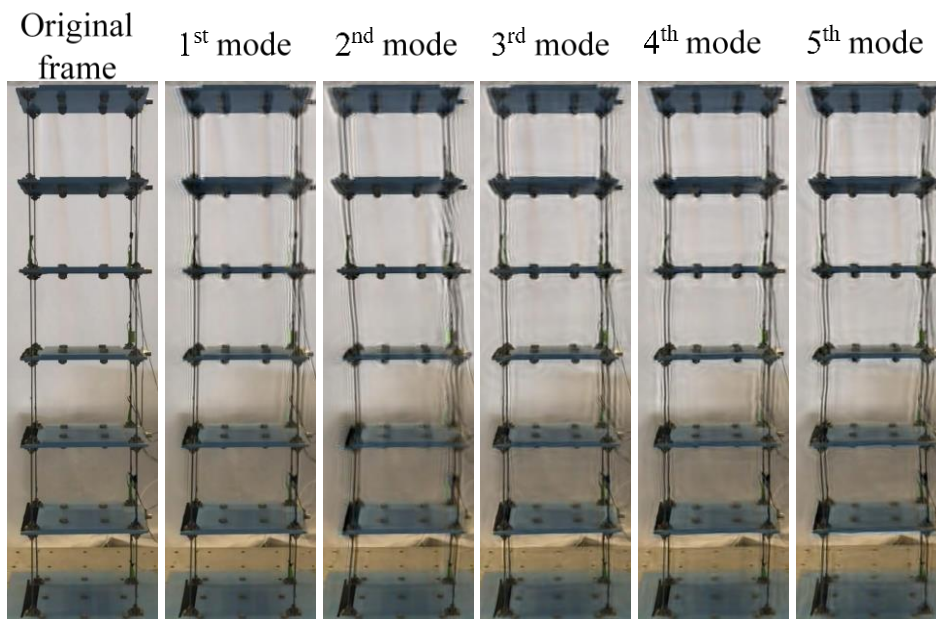


Figure 20: Extracted example frames from the magnified videos, one magnified video per mode.

Experiment 2: 4K (2160p) with 30 fps

The second experiment used a similar test setup as the first experiment but with a resolution of 4K (3,840-by-2,160 pixels) with 30 fps. The tracked displacements at each story are shown in Figure 21 (a). In this experiment, the tracked displacements were used with their original sampling rate, which provided a signal-to-noise ratio of 23.5 dB. However, the displacements of the first experiment were down-sampled from 120 Hz to 30 Hz, and the signal-to-noise ratio was 28.6 dB. The power spectral densities of the measurements in Figure 21 (a) are shown in Figure 15 (b). The

power spectral densities shown in Figure 21 (c) are calculated using the acceleration measurements from computer vision, which are based on the double derivative of the displacements in Figure 21 (a). Notably, the energy level of higher modes is slightly lower than the first experiment. This difference can be attributed to the difference in the signal-to-noise ratios between the two experiments.

Using the displacement measurements from computer vision and using the acceleration measurements from the accelerometers, the average power spectral densities are shown in Figure 22 (a). The average power spectral densities using the double derivative of displacements from computer vision and accelerometers are also presented in Figure 22 (b) and Figure 22 (c). The results from these experiments validated the ability of the proposed framework to identify the frequencies of structures with high accuracy.

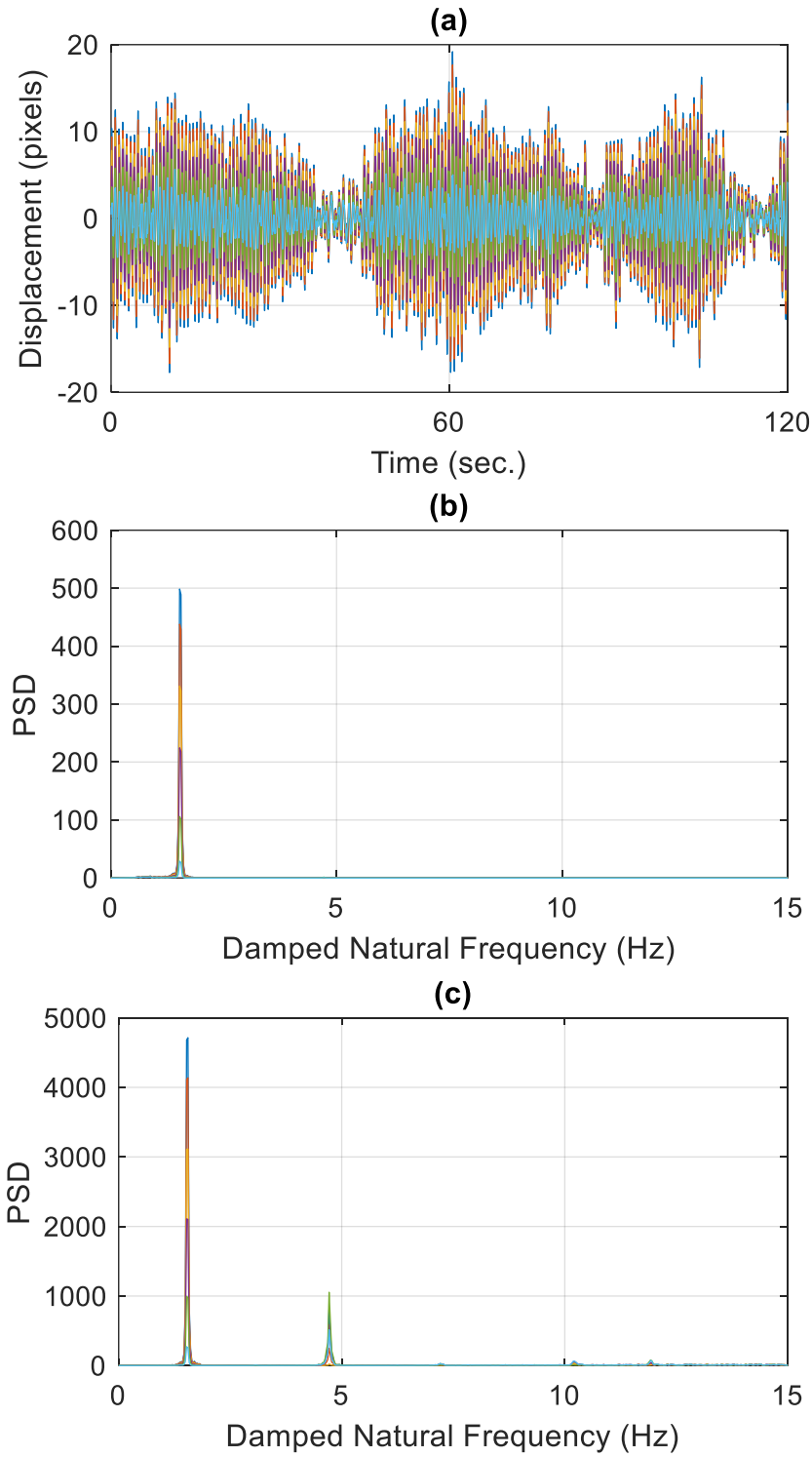


Figure 21: (a) The tracked displacements at each story (the resolution is 4K with 30 fps). (b) The PSDs of measurements in (a). (c) The PSDs using the double derivative of measurements in (a)

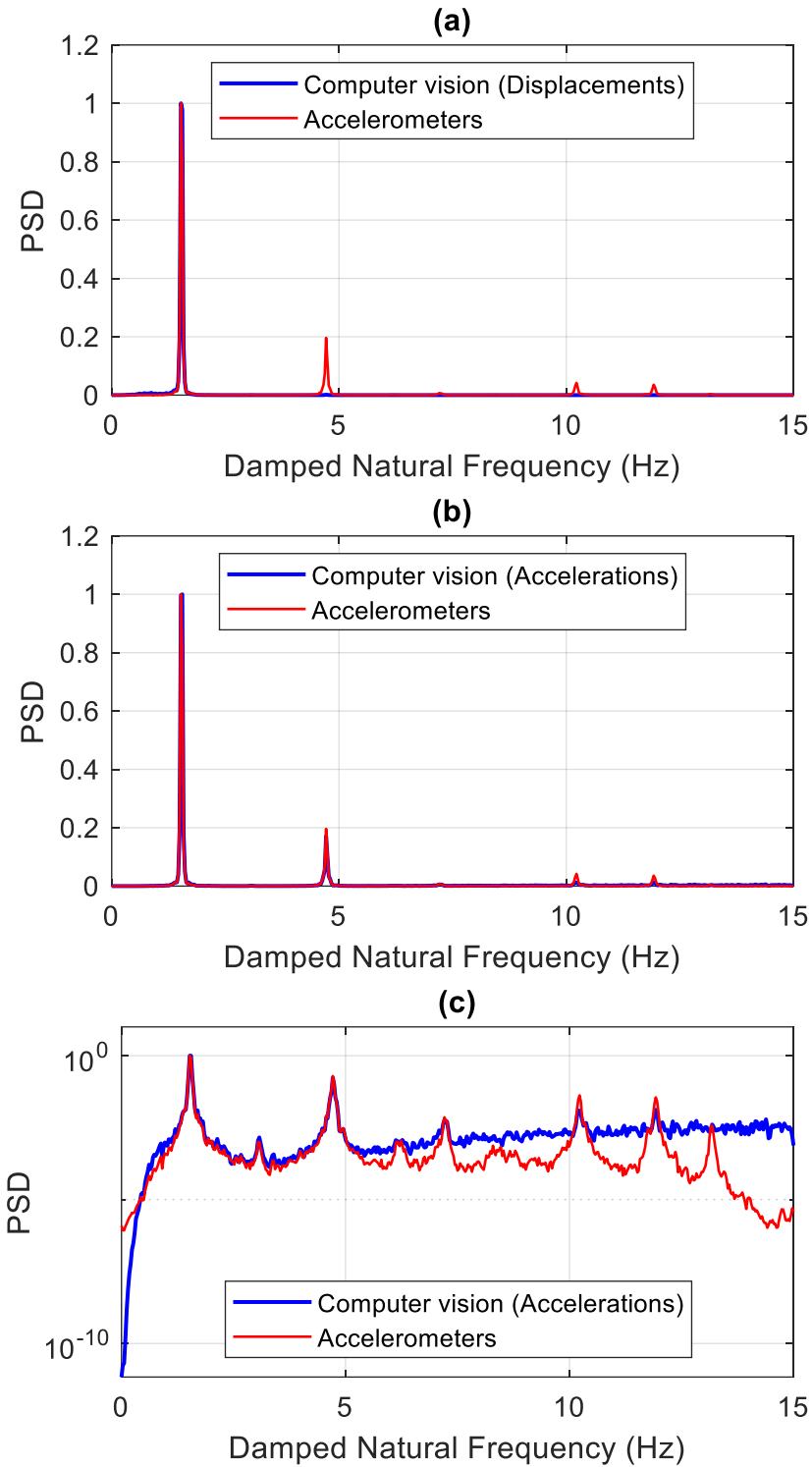


Figure 22: (a) Normalized average PSDs using displacements from computer vision (4K video used in Figure 21) and accelerations from accelerometers. (b) Normalized average PSDs using accelerations from computer vision and accelerometers measurements. (c) similar to (b) but using a logarithmic scale for the y-axis

The mode shapes for the second experiment using Options A and B are in Figure 23. The mode shapes obtained using the accelerometers are in Figure 23. Even though this experiment was recorded using a higher resolution, it provides a lower signal-to-noise ratio than the first experiment. Additionally, by looking at the frequency domain for this experiment, the peak to noise level of higher modes is lower than the first experiment. This difference is the reason for obtaining less accurate high modes in this experiment. The EMAC and MAC values for the mode shapes are presented in Table 6.

The estimated mode shapes using Option A show relatively good accuracy, where all mode shapes have a higher MAC value than 91%, except for the fifth mode with a MAC value of 65%. The mode shapes estimated using Option B high accuracy for all five modes, with a significant improvement for the third and the fifth modes. The MAC value for the fifth mode increased from 65% in Option A to 87% in Option B. As was discussed earlier, the estimation of mode shapes using Option B results in higher accuracy for all modes. On the other hand, estimating the mode shapes using Option A can provide relatively good accuracy but not for all modes, especially for the weakly excited modes.

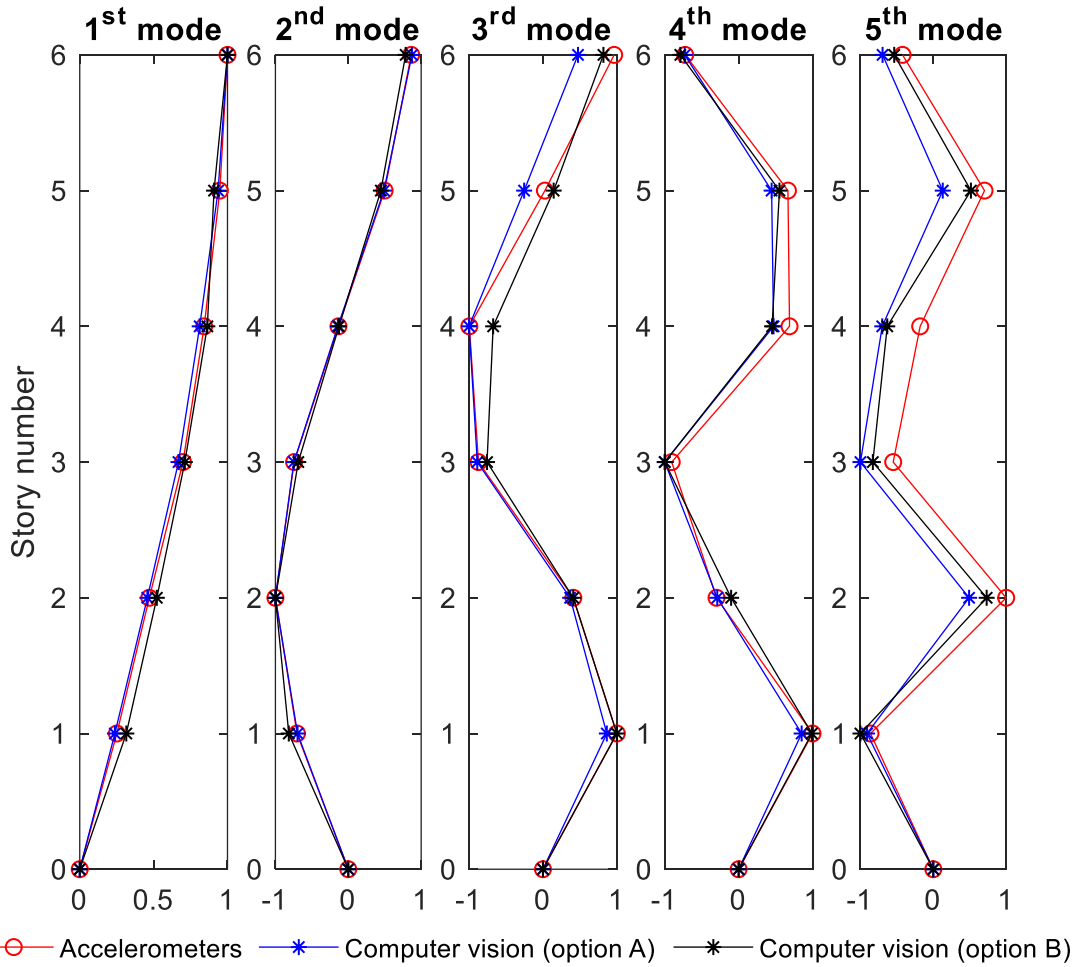


Figure 23: Identified mode shapes using computer vision (4K video used in Figure 21) vs. accelerometers

Table 6: EMAC and MAC values for mode shapes in Figure 23

		1 st mode	2 nd mode	3 rd mode	4 th mode	5 th mode
EMAC values for mode shapes using computer vision		99.81%	99.05%	71.47%	92.14%	77.99%
MAC values for mode shapes obtained using	Option A: KLT only	99.97%	99.99%	91.86%	96.81%	64.84%
	Option B: KLT and PBMP	99.75%	99.21%	97.54%	96.41%	86.75%

4.3.2. Experimental truss bridge

4.3.2.1. Model description

A 3-D truss bridge (shown in Figure 24) was modeled in SAP2000 to be used for numerical investigation in this study (Chapter 4) and the damage identification study (Chapter 5). The truss

bridge consists of 136 tube elements, where the outside diameter is $\frac{3}{8}$ inches, and the internal wall thickness is 0.06 inches. The elements are connected to 48 joints using screws and bolts. The truss has 12 bays with a total span of 18 feet, where the span of each bay is $1\frac{1}{2}$ foot. The height and the width of the bridge are $1\frac{1}{2}$ foot. The truss has a total self-weight of 104 pounds, with additional masses of 110 pounds attached to the bottom chord, the total mass of the structure is 214 pounds. This bridge is used for the experimental investigation (shown in Figure 25).

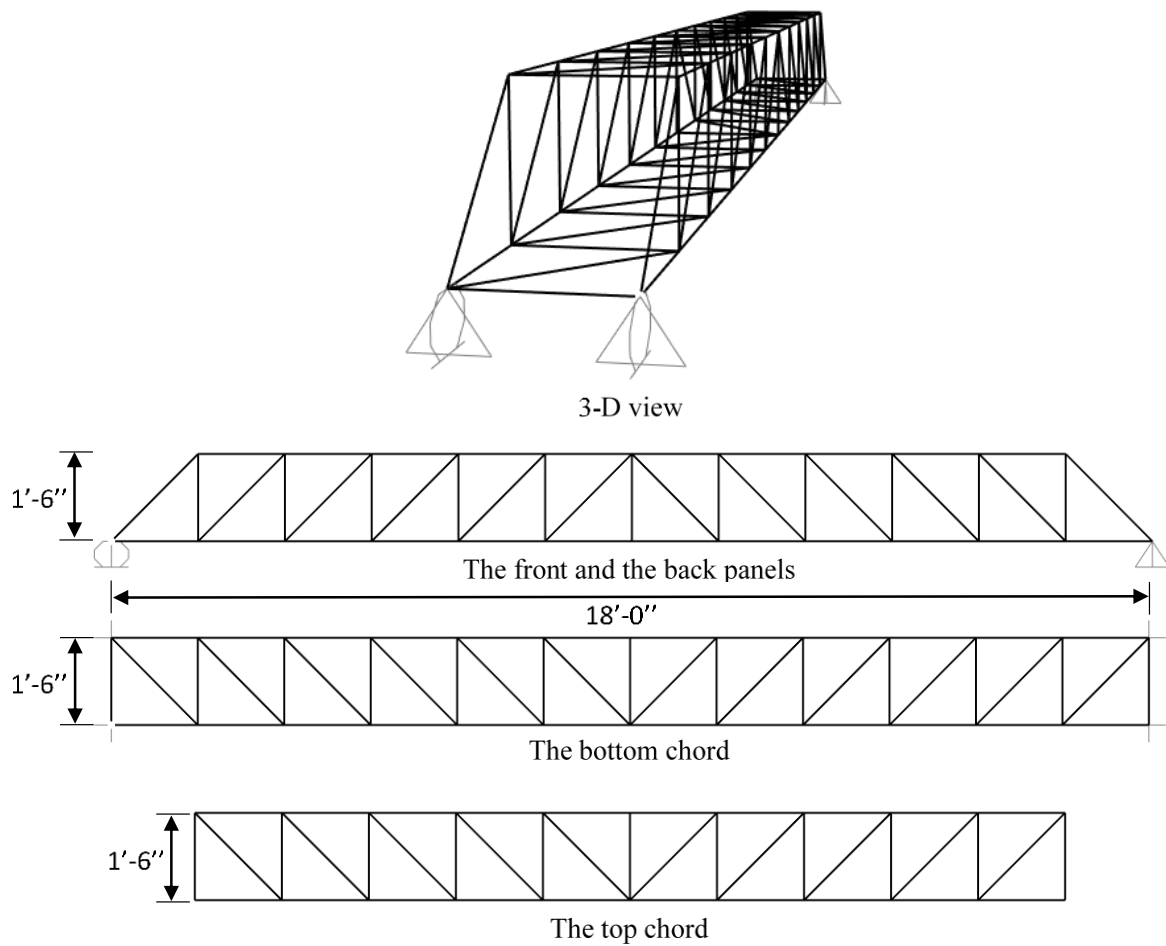


Figure 24: Layout of the 3-D truss bridge

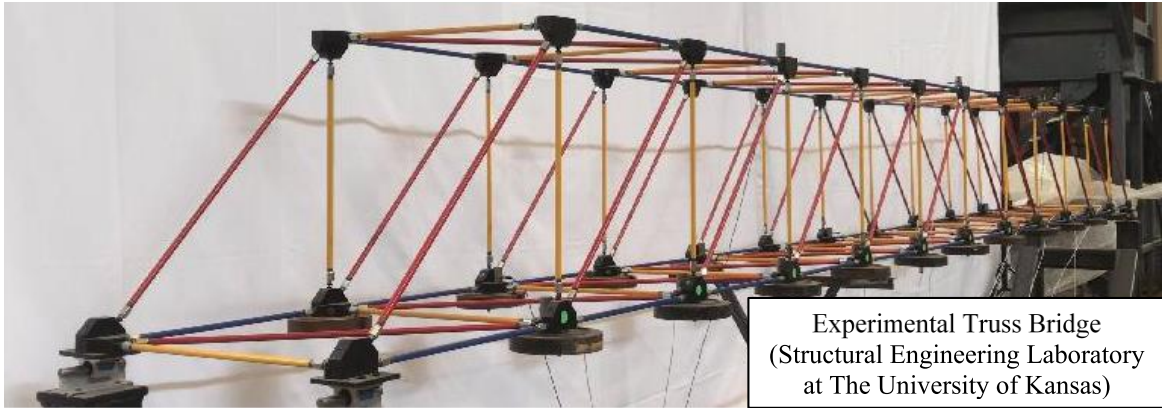


Figure 25: The experimental truss bridge

4.3.2.2. Test setup

The experimental truss bridge in Figure 25 is used to perform an additional experimental investigation of the proposed framework in 4.2.3. This experimental truss bridge was constructed according to the described model in 4.3.2.1. This structure was subjected to BLWN excitation force at joint 5 using the dynamic shaker shown in Figure 27. The input force is limited to 20 pounds due to the shaker limitation. Under the input force, the maximum displacement at the midspan is in the order of 0.02 inches, which is less than $1/10,000$ of the bridge's span.

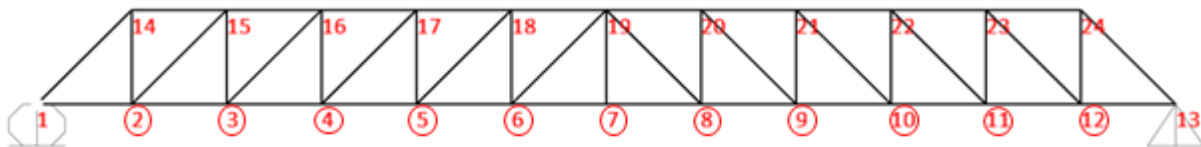


Figure 26: Joints labels of the front panel (monitored 11 joints are circled)

A total of 19 accelerometers are attached to the structure at different locations, including 11 accelerometers at the front panel shown in Figure 26. These accelerations serve as reference measurements for computer vision. The accelerations are sampled at 2048 Hz and then downsampled to 30 Hz or 120 Hz to be compared with computer vision results. The response of the truss is also recorded using the camera of an iPhone 7 that is placed perpendicular to the structure at a distance of 13 feet (see monitored joints in Figure 26). The recorded response video

is used as an input to the proposed framework in 4.2.3. The steps of recording and processing these videos followed the guidelines in 4.2.3.

Like the 6-story structure (experiments 1 and 2), the recorded videos for the truss's response used two resolution and sampling rate options available in the iPhone 7. Experiment 3 used a resolution of 1080p with 120 fps; experiment 4 used 4K with 30 fps. The obtained results using these two options are presented and compared to those from accelerations in the following section 4.3.2.3.

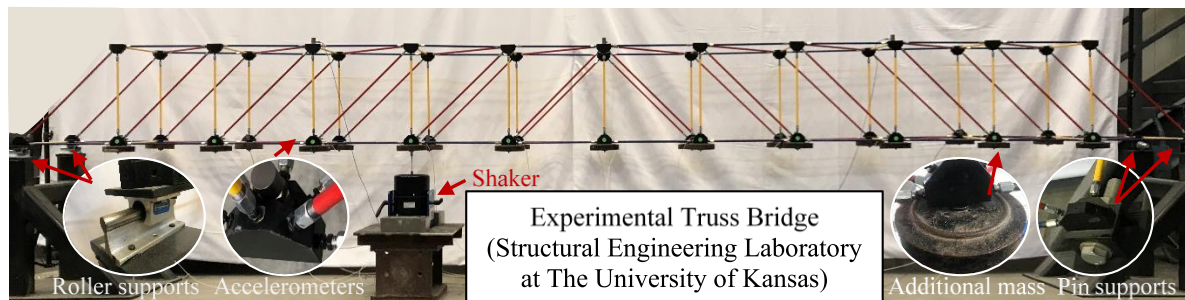


Figure 27: Test setup of the experimental truss bridge

4.3.2.3. Experimental results

The experimental results for the truss bridge from experiments 3 and 4 are presented in this section. The truss bridge's identified fundamental frequency is 13 Hz, which is higher than the typical fundamental frequency for most existing bridges. The first modal frequency of bridges can vary based on several factors, such as the type and the span of the bridge. The modal first frequency of existing bridges can be as low as 0.1 Hz and might reach 5 Hz [25, 106, 107, 130-132, 134]. This high fundamental frequency led to a minimal midspan's displacement of less than $1/10,000$ of the span's length compared to real bridges' measured displacements, which can range between $1/4,000$ and $1/8,000$ of the span's length due to truck or wind loads [81, 83, 91].

The small-displacement makes system identification of this experimental truss bridge more challenging, especially for computer vision methods. Computer vision relies on the displacement measurements, which naturally have a lower sensitivity to high frequencies than acceleration measurements. However, the proposed framework was able to achieve accurate results, even with these discussed challenges. The presented results show the ability of the proposed framework to identify the truss bridge's dynamic characteristics using sub-pixel motions, hardly observed with the naked eyes.

Experiment 3: 1080p with 120 fps

The third experiment used a resolution of 1080p with 120 fps to record the response of the truss structure under band-limited white noise excitation. The results in Figure 28 (a) are the tracked displacements using the KLT at the bottom chord of the front panel of the structure. The total number of tracked joints is 11 (joint number 2 through joint number 12, where joints number 1 and 13 are the supports). Recording and processing the video followed the recommended details and guidelines in the proposed framework in 4.2.3.

The 11 joints were tracked simultaneously using the strongest three local feature points at each joint. The average displacement record of each joint is shown in Figure 28 (a). The amplitude of the maximum displacement at midspan is less than a third of a pixel. In comparison, the minimum displacement amplitude at the bridge supports is less than one-tenth of a pixel.

The power spectral densities of the measurements in Figure 28 (a) are shown in Figure 28 (b). As shown in Figure 28 (b), the fundamental mode's peak is 12.8 Hz. The truss bridge has other modes between 0 Hz and 60 Hz, as is shown in the results from accelerations in Figure 29. However, since the computer vision method relies on displacement measurements, it has a lower

sensitivity to high modes than acceleration measurements. As a result, only the first mode is identified using the computer vision method.

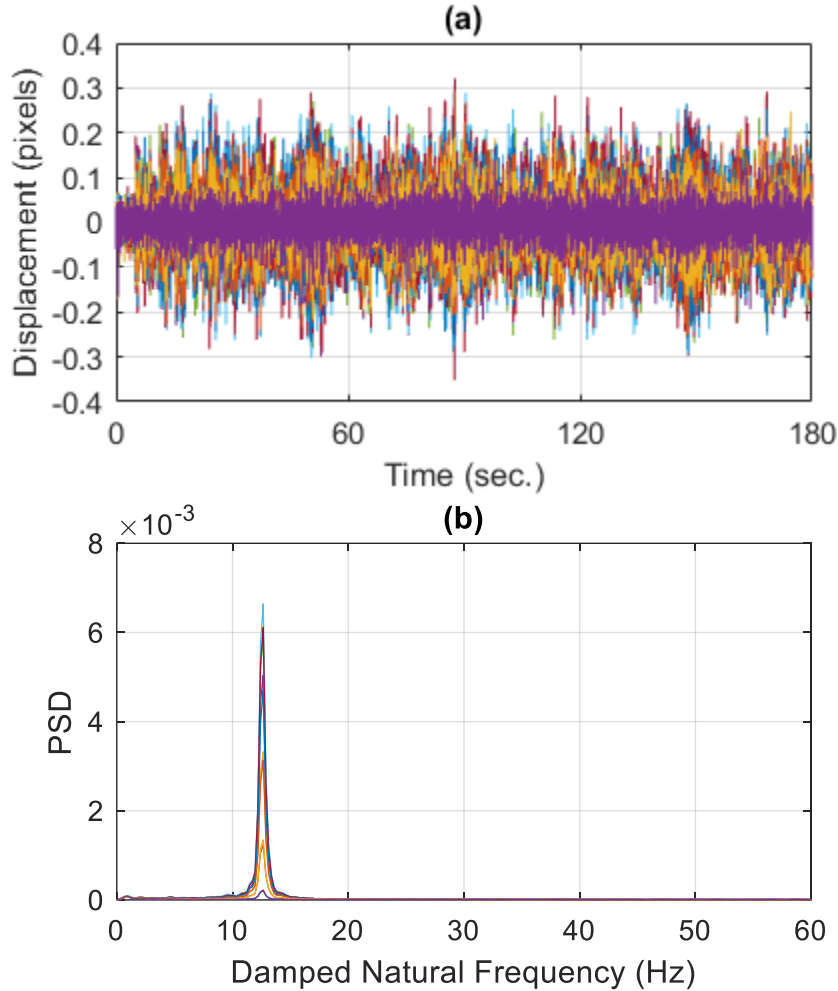


Figure 28: (a) The tracked displacements of the bottom chord of the front panel (the resolution is 1080p with 120 fps). (b) The PSDs of measurements in (a).

The acceleration measurements for the bottom chord of the front panel are shown in Figure 29 (a). The accelerations are collected using a sampling rate of 2048 Hz and then downsampled to 120 Hz, similar to the sampling rate of the computer vision. The acceleration measurements from the accelerometers at the same locations of the tracked displacements are shown in Figure 28 (a). The power spectral densities in Figure 29 (b) are from accelerometers results. The fundamental frequency is 12.8 Hz, which matches the identified frequency from computer vision. In addition

to the fundamental mode, other modes at 30 Hz and 40 Hz were not identified by computer vision. The normalized average power spectral density for computer vision's displacement and acceleration using measurements are shown in Figure 30 (a).

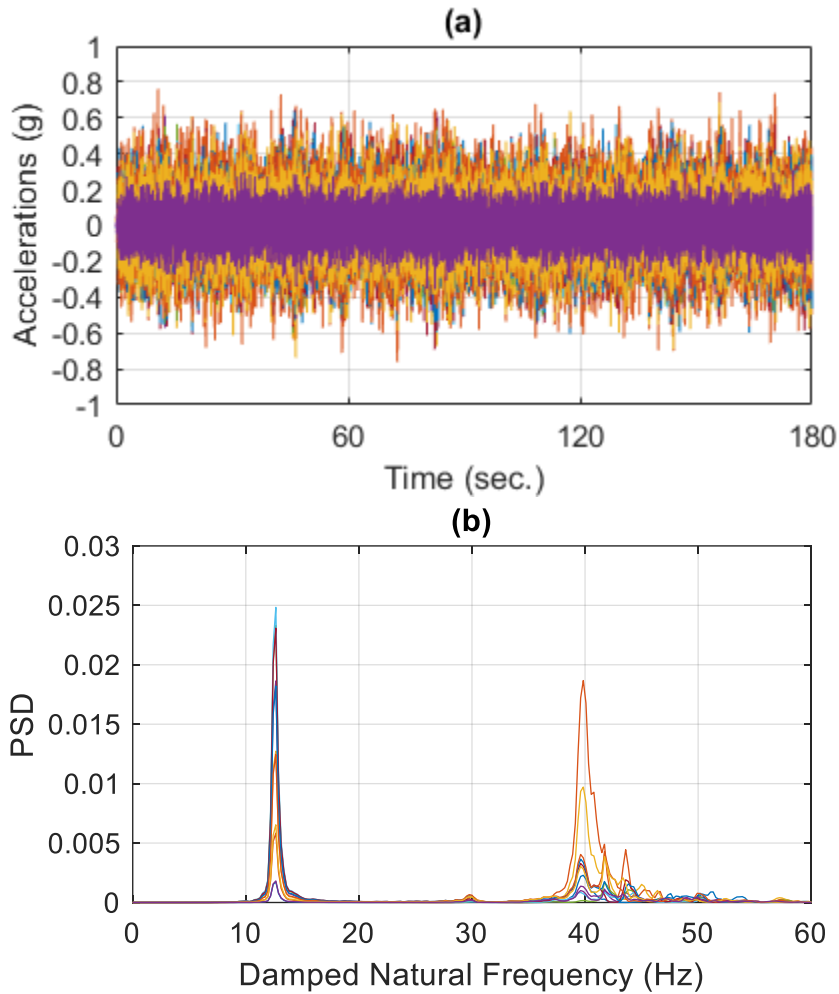


Figure 29: (a) Accelerometers measurements at the bottom chord of the front panel (downsampled to 120 Hz). (b) The PSDs of measurements in (a).

Using the double derivative of the displacement from computer vision did not enhance the truss bridge's results as it did for the 6-story structure; instead, the noise level was amplified, as shown in Figure 30 (b). In the 6-story structure results (experiments 1 and 2), the energy level of higher modes was low, and taking the double derivative of the signal increases their energy level.

However, for this truss bridge, the energy level of higher modes is significantly low, and taking the double derivative would only amplify the noise.

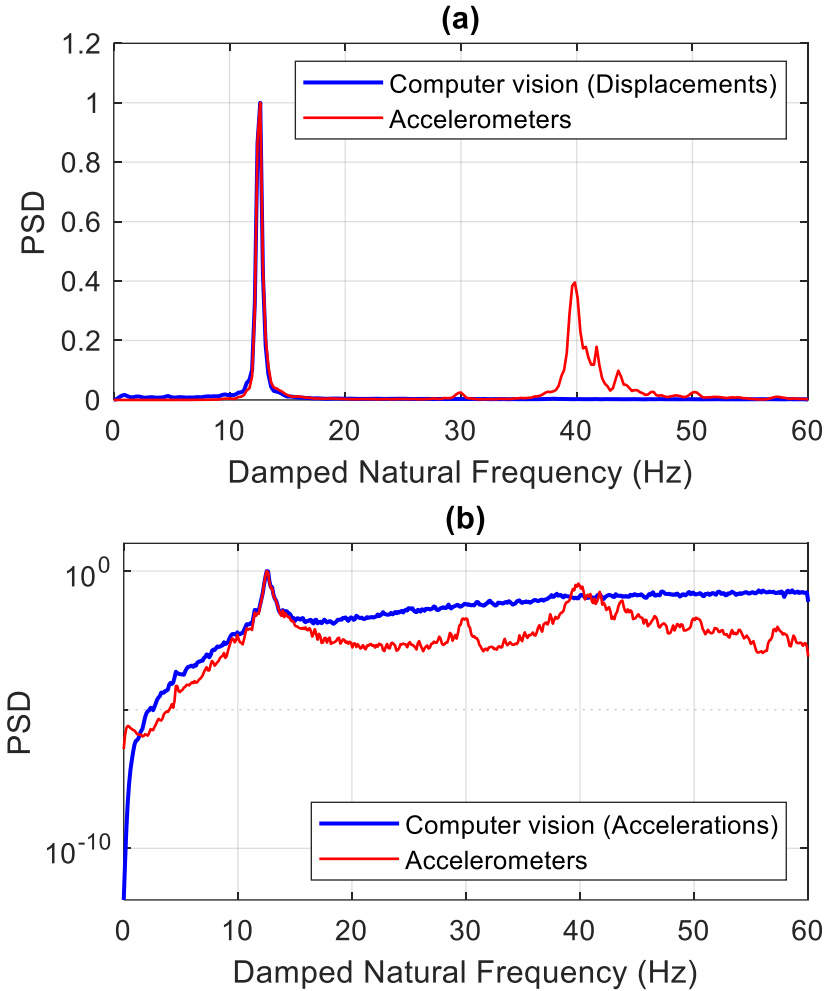


Figure 30: (a) Normalized average PSDs from computer vision (1080pi video Figure 28) and accelerations from accelerometers (b) Normalized average PSDs using accelerations from computer vision and accelerometers measurements (using a logarithmic scale for the y-axis).

The mode shapes for experiment 3 using Options A and B in the proposed framework are presented in Figure 31. For this experiment, the accuracy of the mode shapes obtained from Option A was relatively low. However, mode shape from Option B shows improved accuracy, especially between joints 4 and 10. The MAC values of the mode shapes from Options A and B were similar (99.68% and 99.65%, respectively).

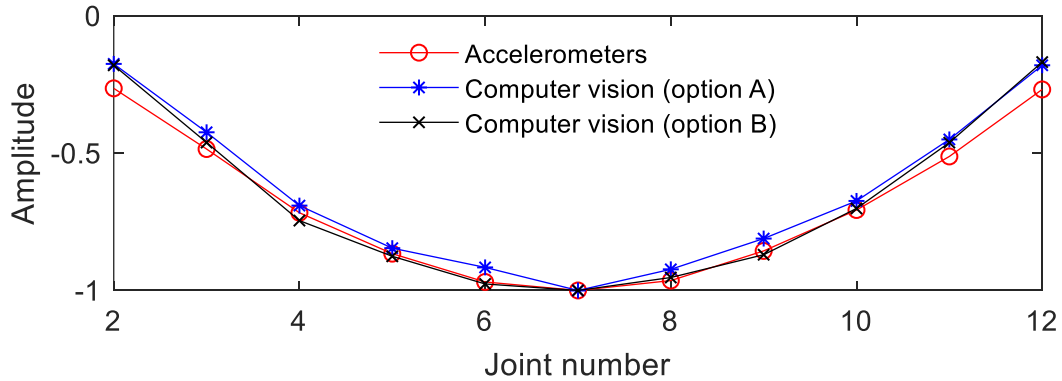


Figure 31: Identified first mode shape using computer vision (1080pi and 120 fps) vs. accelerometers (120 Hz)

The reference frame (the 1st frame) and the 400th frame before and after magnification are shown in Figure 32 and Figure 33. The 400th frame was selected here for illustration purposes, where the peak displacement was observed. It is not easy to distinguish between the original and the magnified videos by looking at single frames. The difference (or subtraction) of two identical frames can help show the location of displaced pixels. If the two frames are identical, the difference between them should result in a zero matrix, displayed as a black image. The difference between the two frames clarifies the difference between the original and the magnified videos. The shown difference frame in Figure 32 and Figure 33 results from subtracting the 1st and the 400th frames. The difference between the two frames before magnification was very close to zero, which means no or negligible motion. However, the magnified video shows a clear motion, especially around the midspan.

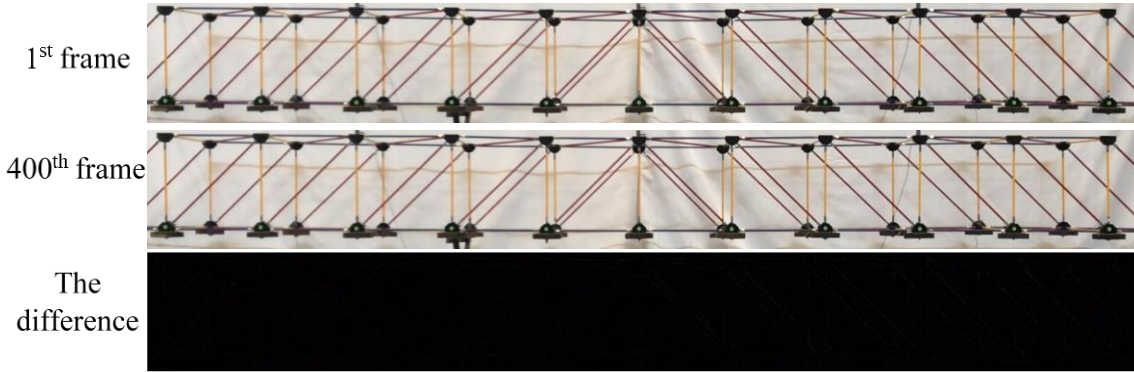


Figure 32: Before magnification

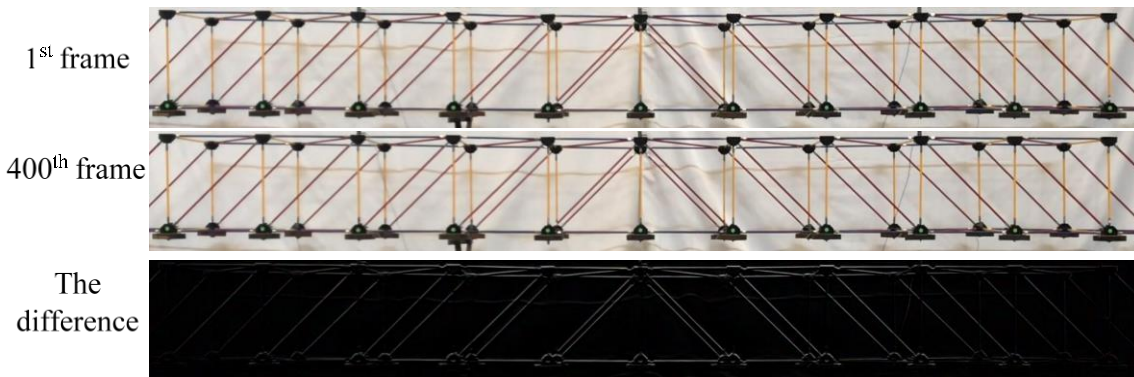


Figure 33: After magnification

Experiment 4: 4K (2160p) with 30 fps

The fourth experiment used a resolution of 4K with 30 fps to record the structural response under band-limited white noise excitation. Figure 34 (a) results are the tracked displacements at the front panel's bottom chord. The total number of tracked joints is 11 joints, similar to experiment 3. The process of recording and processing the video also followed the recommended details and guidelines in the proposed framework in 4.2.3. The 11 joints were tracked simultaneously using the strongest five local feature points at each joint. The number of strong feature points is higher in this experiment due to the used higher resolution. The average displacement record of each joint is in Figure 34 (a).

The maximum midspan's displacement is less than two-thirds of a pixel. In comparison, the amplitude of displacement at the bridge supports is less than a third of a pixel. The power spectral densities are shown in Figure 34 (b). As shown in Figure 34 (b), the fundamental mode is identified at 12.7 Hz. The truss bridge does not have other modes that fall in 0 Hz to 15 Hz.

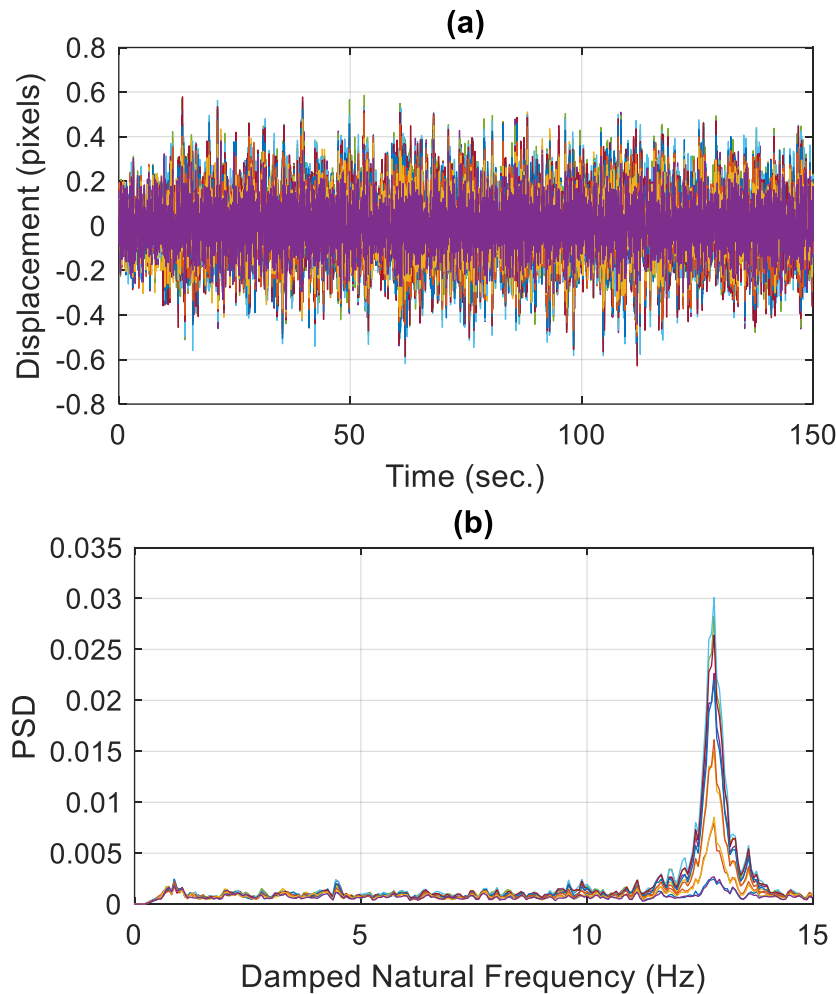


Figure 34: (a) The tracked displacements of the bottom chord of the front panel (the resolution is 4K with 30 fps). (b) The PSDs of measurements in (a).

The measured accelerations from experiment 4 at the bottom chord of the front panel are presented in Figure 35 (a). The accelerations are collected using a sampling rate of 2048 Hz and then downsampled to 30 Hz, similar to the sampling rate of the computer vision. The power spectral densities of these accelerations are provided in Figure 34 (b). The fundamental mode's

frequency is 12.7 Hz, which matches the identified frequency from computer vision. In the range 0 Hz to 15 Hz, only a single mode is identified from accelerations and computer vision. The normalized average power spectral density for computer vision's displacement and accelerometers' measurements are shown in Figure 36.

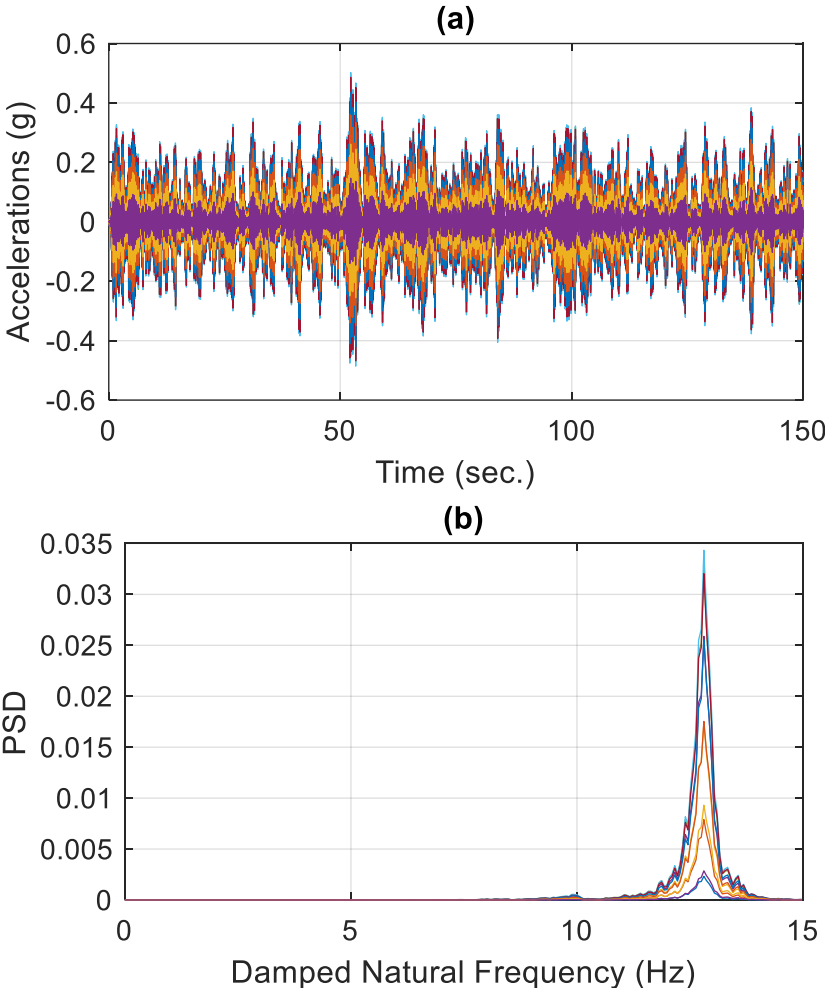


Figure 35: (a) Accelerometers measurements at the bottom chord of the front panel (downsampled to 30 Hz). (b) The PSDs of measurements in (a).

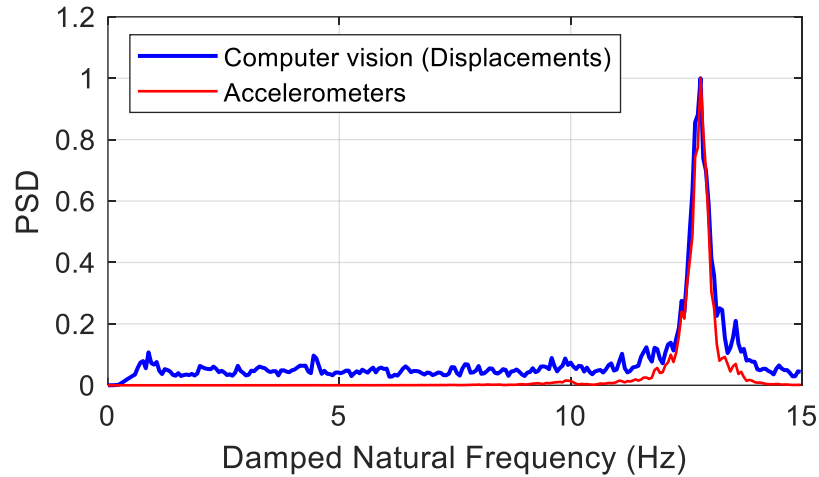


Figure 36: Normalized average PSDs from computer vision (4K video) and accelerometers

The mode shapes in Figure 37 are identified using accelerometers and computer vision (Options A and B). Options A and B results have a great match with accelerometers' results. In this experiment, the used resolution is four times the resolution of experiment 3 (twice the resolution at each axis). Similar to the 6-story structure (experiments 1 and 2), the difference between Options A and B is not significant because the mode shape is estimated with high accuracy in Option A. The MAC values for mode shapes of Options A and B are 99.97% and 99.91%, respectively.

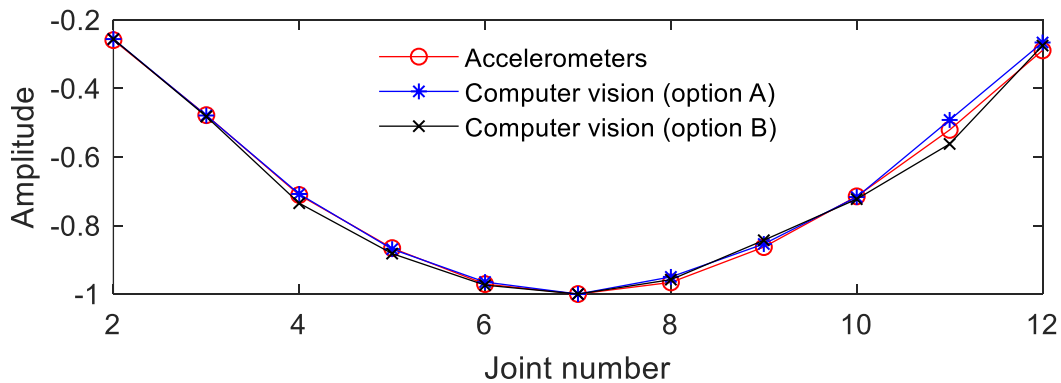


Figure 37. Identified first mode shape using computer vision (4K and 30 fps) vs. accelerometers (30 Hz)

4.4. Summary

The beginning of this chapter presented a general background about system identification using computer vision and its limitations compared to traditional sensors. This study proposes a method for system identification using computer vision with two options to estimate the mode shapes (Options A and B). The Guidelines and detailed steps of implementing the proposed framework were provided for both pre-recording and post-processing steps.

Several methods were adopted in the proposed framework: the ERA, the KLT, and the PBMP. The proposed framework was validated experimentally using two structures: the small-scale 6-story (experiments 1 and 2) and the experimental truss bridge (experiments 3 and 4). The results from the four experiments show the ability of computer vision to reach comparable results to accelerometers. The mode shapes result from Option B that combines the KLT with the PBMP methods, showed significant improvement for the weakly excited modes in comparison to Option A that only uses the KLT method.

The experimental investigation used a consumer-level camera (an iPhone 7) and relied on small structural displacement motion. The proposed method shows the potential of overcoming some of the main existing limitations and challenges. These limitations include the need for exceptional high-speed cameras, special lighting conditions, or the need for a large motion of the structure (which is not available from real structures under normal operational loads). Besides, this method extracted and validated the mode shapes, which allow for extended applications such as damage identification discussed in the following study (Chapter 5).

CHAPTER 5: DAMAGE IDENTIFICATION USING COMPUTER VISION

5.1. Introduction and background

One of the significant structural health monitoring applications is damage identification, which is essential for several reasons, such as safety, maintenance, and research purposes. Damage identification using vibration-based methods relies on the fact that the structure's global dynamic characteristics are affected by local stiffness change. Vibration-based damage identification relies on detecting changes in modal parameters such as frequencies and mode shapes that represent the physical properties of the structure.

Vibration-based damage identification methods are classified into three levels: detection, localization, and quantification. In the first level, the goal is to detect the presence of change from the measured response or modal information of the structures. In the second level, the methods detect and localize the damage, which can be data-driven or model-based. The methods in the third level quantify the damage and can be data-driven or model-based [34, 38].

Vibration-based damage identification methods rely on extracting modal parameters from measured data before and after the damage. Traditional sensors (e.g., accelerometers) have been widely used to measure the vibration of structures pre and post damage. However, damage identification using traditional sensors can be costly, requires physical contact, and measures limited degrees of freedom. Alternatively, feature-based computer vision methods for damage identification can be more effective in terms of cost, do not require physical contact, measure a high number of degrees of freedom.

This study investigates the possibility to use computer vision in damage identification. It was confirmed in Chapter 4 that computer vision—using either Option in the proposed

framework—can achieve high accuracy in identifying the frequencies and the mode shapes of the structure. This gives the potential for computer vision to be used for damage identification. This study adopted the proposed framework in Chapter 4, combined with a damage localization method known as the Damage Locating Vector (DLV) method that is discussed in detail in 5.2.2. The robustness of the DLV method has been discussed and established numerically by Bernal [13]. Other studies also provided experimental validation of the DLV method [49]. In these studies, acceleration measurements were used to localize damaged elements.

The main focus of this study is to examine the possibility to use computer vision in damage identification. Computer vision methods measure the displacement response of structures; however, the common traditional sensors are accelerometers that measure acceleration response. A critical difference between displacement and acceleration measurements is their sensitivity to high modes, as the acceleration measurements have a higher sensitivity to high modes. The number and accuracy of the measured modal parameters before and after the damage significantly impact the accuracy of damage localization.

Theoretically, the DLV method is capable of localizing the damage regardless of the damage level. However, in practical cases, relatively significant local damage could result in a minor change in the modal parameters. Detecting minor changes in modal parameters is practically challenging, making it difficult to identify damage in these cases.

In this section, numerical and experimental investigations are presented using the 3-D truss bridge discussed in Chapter 4. The numerical investigation considered some of the practical challenges for damage identification in general and computer vision in particular. The considered challenges include adding noise to the measurements and investigating different damage levels. Temporal-aliasing can be a practical challenge for computer vision in some cases. A discussion

about temporal-aliasing and its effect on damage identification using the DLV method is provided in 5.3.3.

5.2. Methodology

5.2.1. Motivation of Flexibility-based methods

Experimental identification of high-frequency modes is more challenging than identifying low-frequency modes as low-frequency modes are generally easier to be excited and have higher energy. As a result, estimating an accurate stiffness matrix using measured vibration data is difficult. The stiffness matrix is sensitive to high modes because of its direct relationship with the square of the modal frequencies. However, the flexibility matrix, which is the inverse of the stiffness matrix, is less sensitive to the high modes because it has the inverse relationship with the square of the modal frequencies. The flexibility matrix can be constructed with a high accuracy using only a few modes. To illustrate that, consider the truss shown in Figure 38 that has 45 degrees of freedom. The flexibility matrix of this truss is estimated using a vary number of modes, from a single-mode shape to all mode shapes.

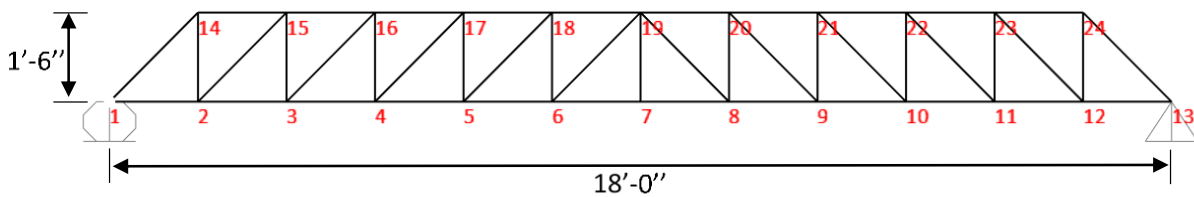


Figure 38: A 2-D truss example with 45 elements

The error is calculated using the norm of the difference between the estimated flexibility matrix ($F_{estimated}$) and the actual flexibility matrix (F) over the norm of (F), as shown in equation (5-1). The error in the estimated flexibility matrix was minimal after including the first few modes, and the error is less than 1% by including the first six modes, as shown in Figure 39.

$$Error = \frac{\|F_{estimated} - F\|_2}{\|F\|_2} \quad (5-1)$$

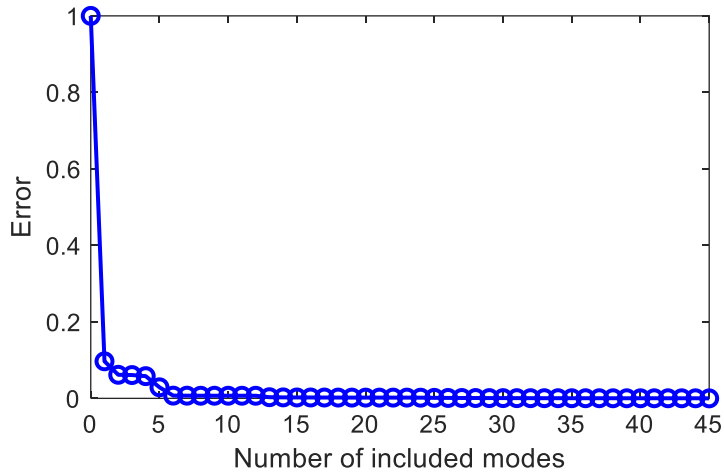


Figure 39: Flexibility matrix construction

The ability to achieve high accuracy by including only a few modes gave the potential to dynamically measured flexibility matrices for damage identification. Several methods were motivated by this unique feature of the flexibility matrix, such as the DLV method discussed in Section 5.2.2.

5.2.2. Damage locating vector (DLV) method

Bernal (2002) proposed a method for damage localization in structures by assuming the structure's response is linear in the pre-damage and the post-damage states [13]. The DLV method uses the change in flexibility matrices (ΔF) before and after the damage (F_U and F_D) to localize the damage as shown in equation (5-2). In equation (5-2), the DLVs are computed as the null space of the change in the measured flexibility, assuming $\Delta F \neq 0$. The matrix L contains the independent vectors which produce identical deformations for the damaged and the undamaged states. The column vectors in L are the damage locating vectors (DLVs) [13].

$$(F_D - F_U)L = (\Delta F)L = 0 \quad (5-2)$$

The DLVs have the feature of inducing zero stresses to the damaged elements when applied to the undamaged structure. For field measurements, the induced stress to the damaged elements by the DLVs \neq zero. Instead, the DLVs induce relatively small stresses to the damaged elements due to noise in the measurements and the approximations.

This method requires a representative static model in the undamaged state to localize the damage. When the DLVs are applied to the structure, they produce identical deformation in the damage and the undamaged states. This allows the method to rely on the change in the flexibility matrices (ΔF) between the damaged (F_D) and the undamaged (F_U) states to localize the damage (see Figure 40). The DLV method is adopted in this study for damage localization.

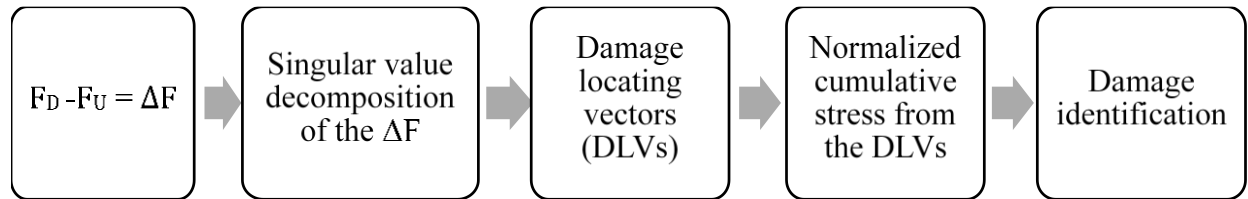


Figure 40: Processes of damage identification using the DLV method

5.2.3. Framework

This study includes numerical and experimental investigations for damage identification using the DLV method. The numerical investigation uses acceleration measurements with added noise to represent the traditional field measurements. The numerical investigation also uses displacement measurements with added noise to simulate the results from computer vision. The numerical results for computer vision consider the experimental limitations of the system identification with computer vision discussed in Chapter 4. One of the main limitations is the number of identified modes from computer vision when compared to accelerometers. For the numerical and

experimental investigations, the same 3D truss structure in Chapter 4 is used. The truss has a small motion under BLWN excitation, simulating ambient vibration.

The steps shown in Figure 41 show the framework of implementing the DLV method in this study. In the first step, the response of the structure is measured for the damaged and undamaged states. These measured responses can be either from numerical simulation or can be measured experimentally. The frequencies and the mode shapes are then identified using these responses, which is similar to Chapter 4 for the experimental measurements. The rest of the steps is similar to the process of implementing the DLV method, discussed earlier in Figure 40. The details and the results of the numerical investigation are shown in the following section 5.3. Moreover, the test setup with the results from the experimental investigations are shown in section 5.4.

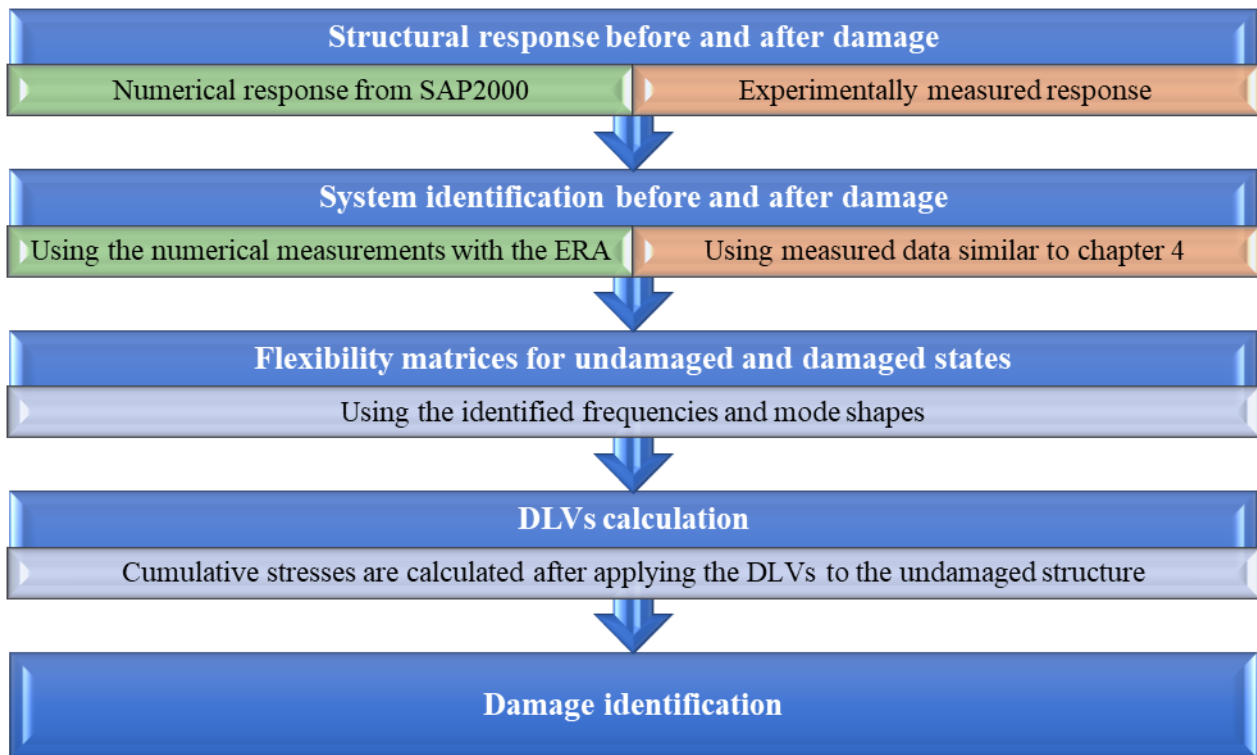


Figure 41: The framework of damage identification for the numerical and the experimental investigations

5.3. Numerical investigation

5.3.1. Model description and damage simulation

The 3-D experimental truss bridge discussed in 4.3.2.1 is modeled in SAP2000 and MATLAB to be used for the numerical investigation of this study (see Figure 42). The truss has 48 joints and 136 frames, with a total of 134 degrees of freedom (DOFs). The structure is excited using the BLWN record shown in Figure 43. This record was experimentally measured when exciting the experimental truss bridge that is discussed in sections 4.3.2 and 5.4. The amplitude of the input force is 20 pounds. This input force resulted in 0.03 inches of displacement at the midspan, comparable to the measured displacement in the experimental structure.

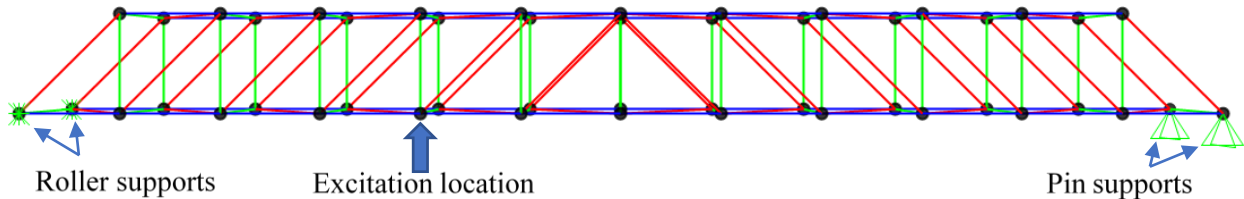


Figure 42: The 3-D truss bridge model in SAP2000

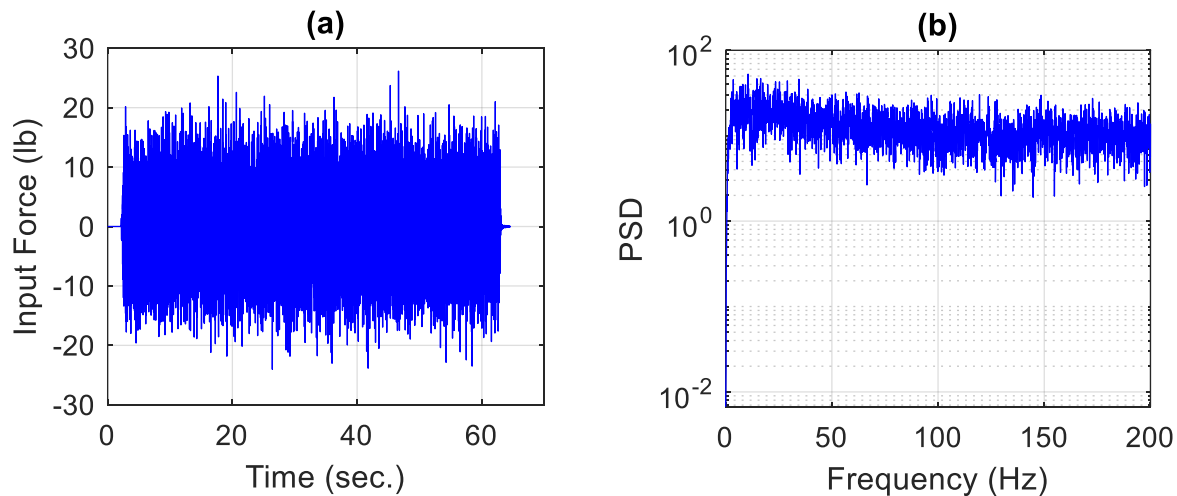


Figure 43: (a) Input force record (b) The PSD of record in (a)

Damage is simulated by reducing the cross-sectional area of the undamaged element. The numerical investigation includes four cases with different damage scenarios. These cases included

horizontal, vertical, and diagonal damaged elements. The labels for the elements of the truss are shown in Figure 44.

The acceleration and displacement responses are extracted from SAP2000 for undamaged and damaged cases at certain joints of the structure. These measurements are used to localize the damage for the numerical case without the presence of noise. Measurement noises are added to the records using BLWN with a root mean square (RMS) amplitude of 5%. The damage localization is then repeated using the measurements with noise. The power spectral densities from acceleration and displacement with and without noise are shown in Figure 45. As shown in the figure, the noise has a larger impact on the high mode in displacements than accelerations. This difference is expected due to the significant difference in the energy levels of higher modes between the accelerations and displacements.

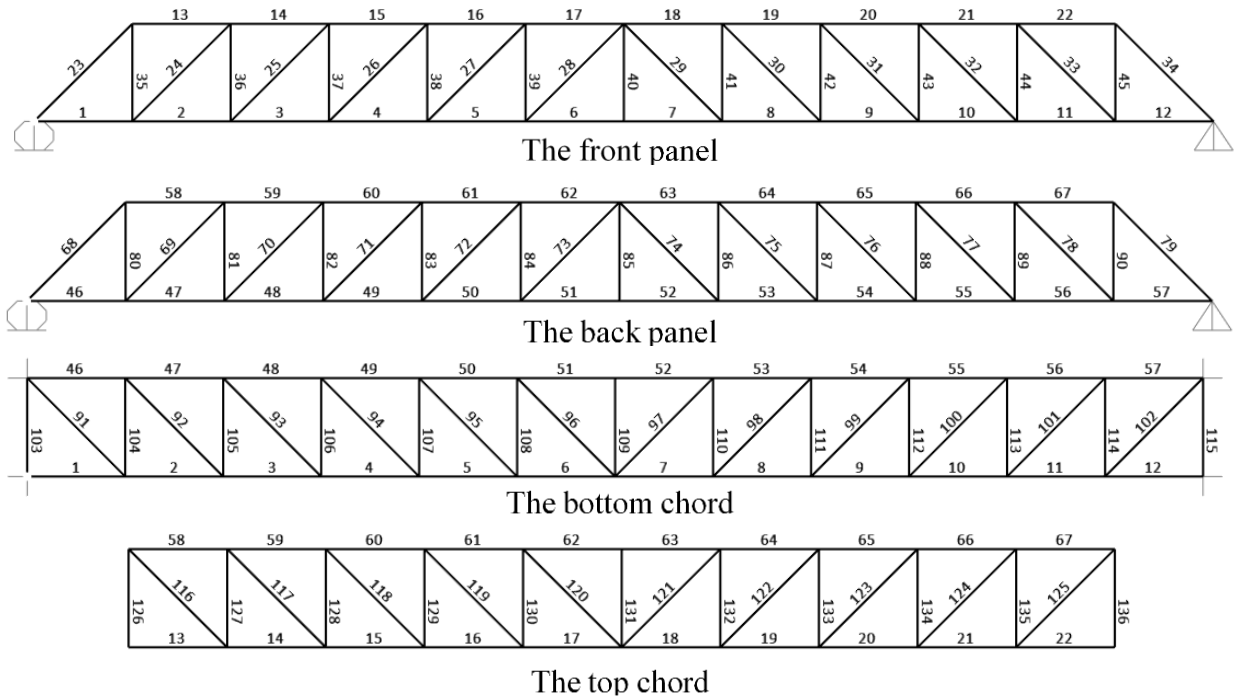


Figure 44: The 3-D truss model in SAP2000 with elements labels

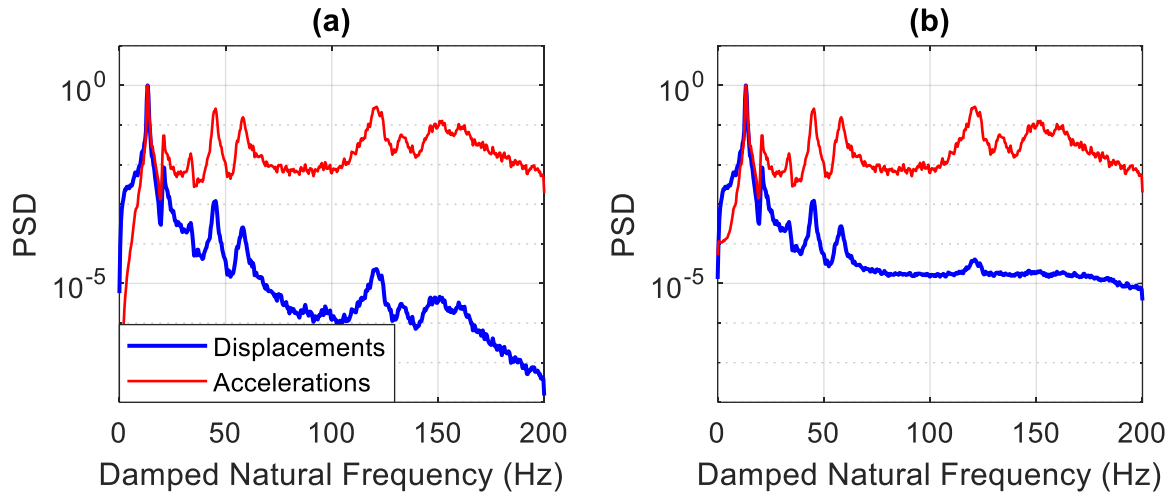


Figure 45: PSDs from numerical outputs from SAP2000 (a) no noise (b) with noise

The number of included modes for damage identification in this study was limited to possible modes identified by the computer vision based on the experimental results in section 4.3.2.3. Those experimental results show computer vision’s ability to estimate the first mode for the experimental truss bridge, unlike the small-scale building structure for which the computer vision method was able to estimate five modes. Another factor that impacted the number of included modes is the typical sampling rate of consumer-level cameras, which is limited to 120 fps or less for a reasonable resolution. Based on these limitations, this study included three identified modes for damage identification. Using a structural acceleration response can identify a greater number of modes than displacement response. The acceleration measurements have a higher sensitivity to high modes and provide a larger sampling rate. Including a large number of modes might have an impact on the accuracy of damage identification if these modes were estimated with high accuracy. However, this is beyond the scope of this numerical investigation, which is focused on investigating the possibility of using computer vision for damage identification. The included mode shapes are shown in Figure 46. These modes will be used in the next section for the numerical results presented in section 5.3.2.

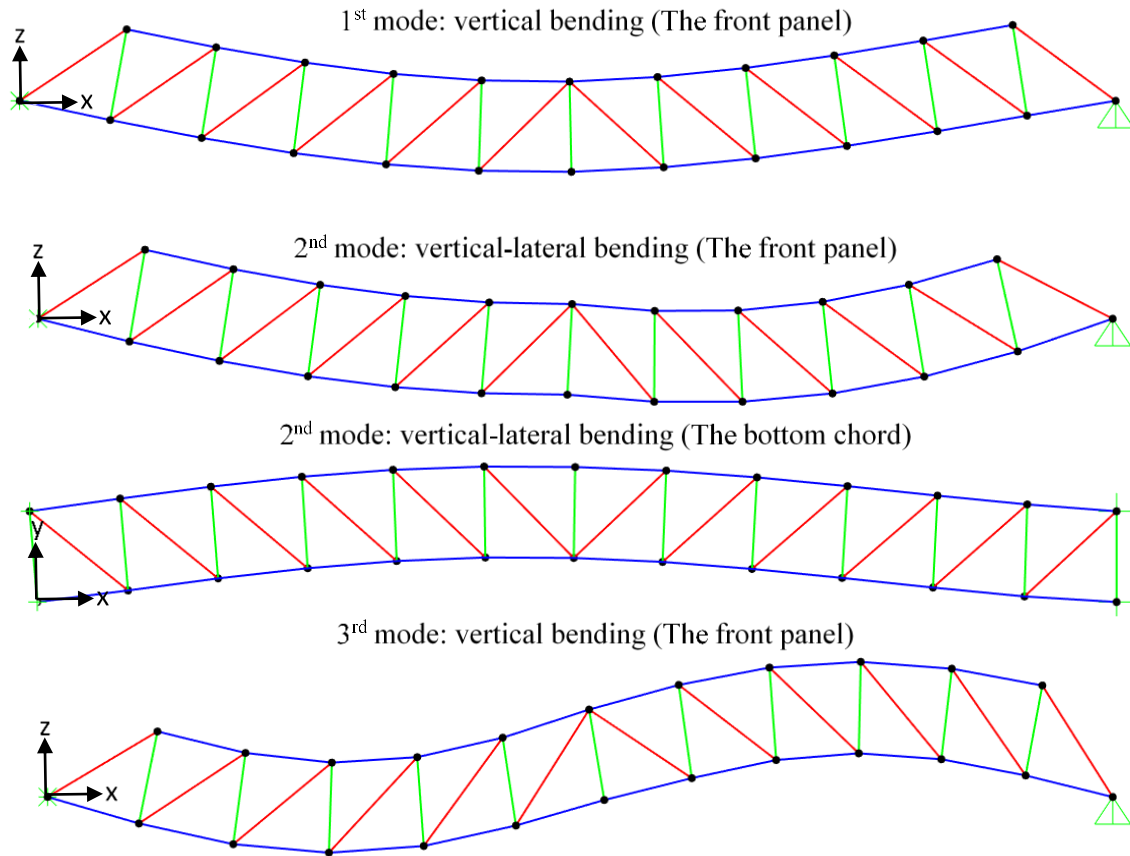


Figure 46: Mode shapes from the 3-D truss model in SAP2000

5.3.2. Numerical results

As an example of applying the DLV method to the 3-D truss structure, the results shown in Figure 47 are obtained using a flexibility matrix constructed by 15 modes that included all the 134 DOFs. Element 7 is damaged by reducing its cross-sectional area by 50%. The obtained DLVs were able to localize the damage by inducing zero cumulative stresses in the damaged element. Elements 103 and 115 also show zero forces, which are the two elements connecting the supports, and they are zero force members. However, measuring all 134 DOFs in practice is challenging, and estimating 15 modes is also difficult in practice. In considered cases in this section, the flexibility matrix is constructed using only 11 DOFs out of 134 DOFs. The included DOFs are the same for

the numerical and the experimental investigations, which are the vertical DOFs at the bottom chord of the front panel (joint 2 through joint 12, as shown in Figure 48).

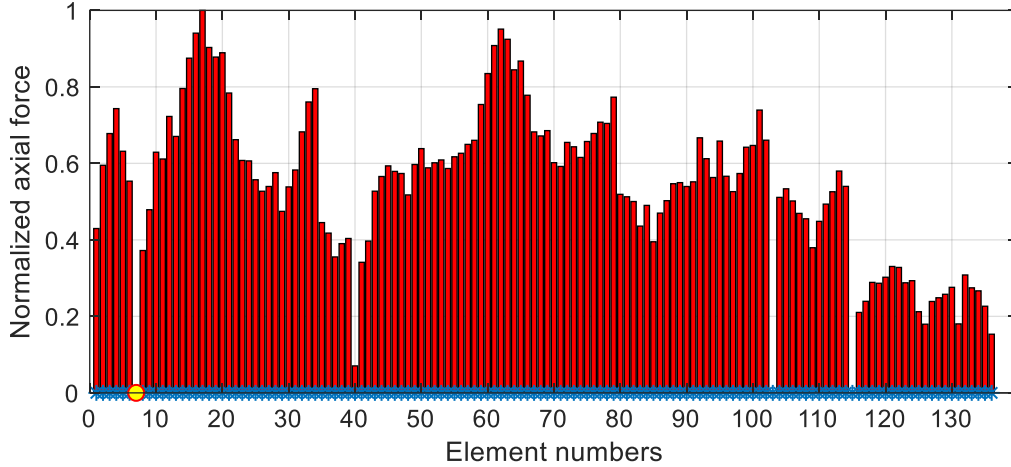


Figure 47: Example case where the damaged element is number 7 by 50%

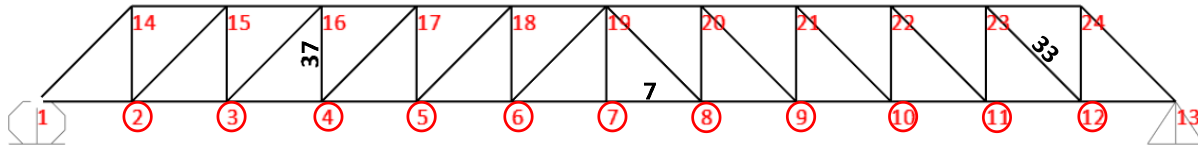


Figure 48: The location of the included 11 vertical DOFs (shown in circles) and the labeled damage locations

The numerical investigation included four cases. For each case, damage identification was performed using acceleration measurements and displacement measurements. Cases are presented using the numerical measurements from SAP2000 with and without added noise. A summary of the four cases is shown in Table 7. The number of measured DOFs is 11 out of the total 134 DOFs, and the included modes are three modes due to the computer vision limitations discussed earlier. The monitored elements are 45 elements of the front panel, for which the 11 DOFs are measured.

Table 7: Summary of the numerically investigated cases

	Damaged element	Reduction in the cross-sectional area	Change in the fundamental frequency	Results are shown in
Case 1	37	40%	0.07%	Figure 49, Figure 50, Figure 51, and Figure 52
Case 2	33	30%	0.15%	Figure 53, Figure 54, Figure 55, and Figure 56
Case 3	33	50%	0.45%	Figure 57, Figure 58, and Figure 59
Case 4	7	50%	2.3%	Figure 60, Figure 61, Figure 62, and Figure 63

Case 1:

In this case, the cross-sectional area of element 37 was reduced by 40% to simulate damage. This reduction results in a small change of 0.07% in the fundamental frequency of the truss bridge, as shown in Table 7. The mode shapes before and after the damage also have a minimal difference that is hard to be observed by direct comparison of the mode shapes, as shown in Figure 49. Theoretically, the DLV method can localize the damage regardless of the damage level. The DLV method has the advantage of using truncated flexibility matrices, which are constructed using partial measurements and a small number of modes. However, using partial measurements could induce a small (or zero) cumulative stresses to undamaged elements due to a particular sensor configuration. For example, element 37 is damaged, and only the 11 vertical DOFs at the bottom chord are included. Under this configuration and due to the vertical force balance at joint number 16, if element 37 has a small axial force, then element 25 will have a small force. The results in Figure 50 show the ability of the DLV method to localize the damaged element using very few modes. However, after adding the noise to the measurements, the DLV method could not localize the damage, as shown in Figure 51 and Figure 52. This is attributed to the difficulty of achieving extremely accurate measurements with the presence of noise. In other words, the induced error in

the undamaged and the damaged states by the noise and modeling error exceeds the difference due to damage.

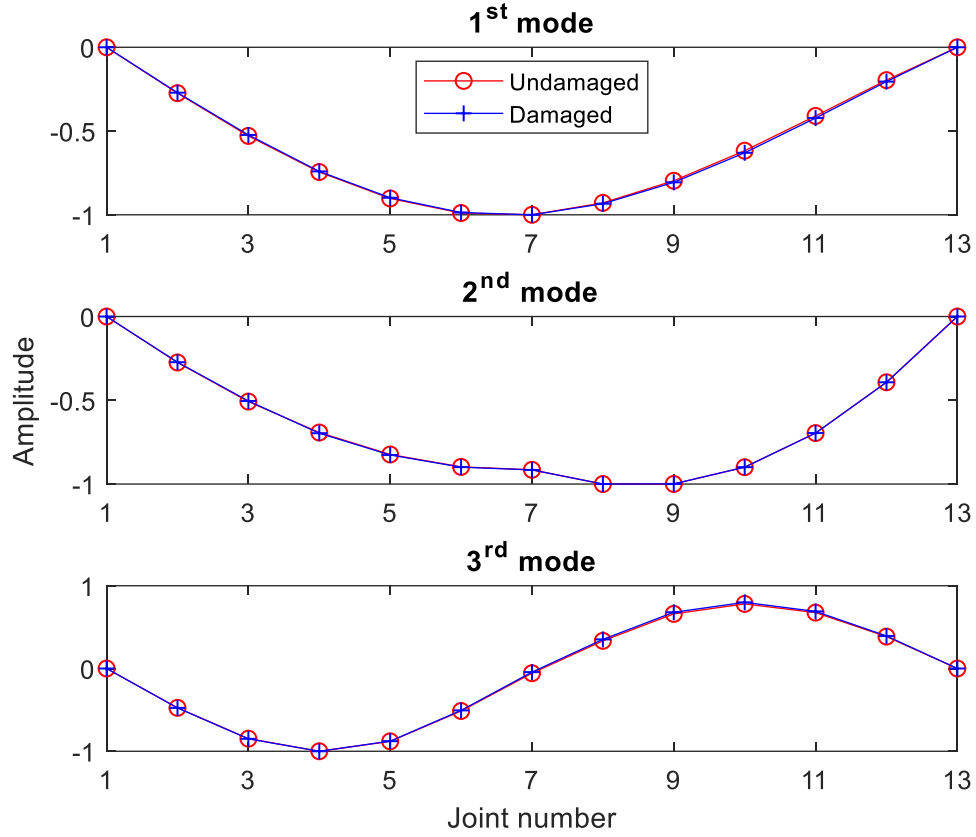


Figure 49: Mode shapes for case 1 (element 37 is damaged by 40%)

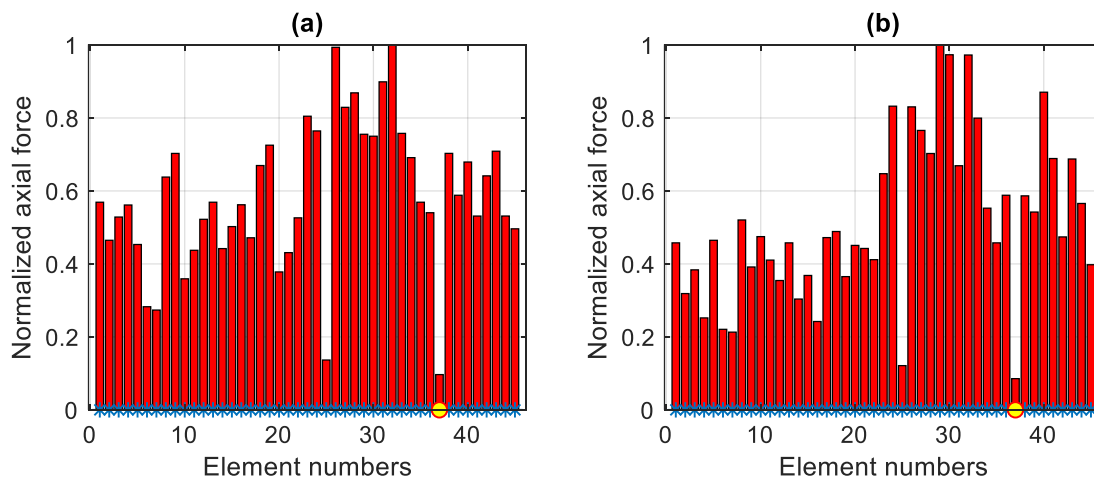


Figure 50: Results for case 1 using acceleration without noise including: (a) Two modes (b) Three modes

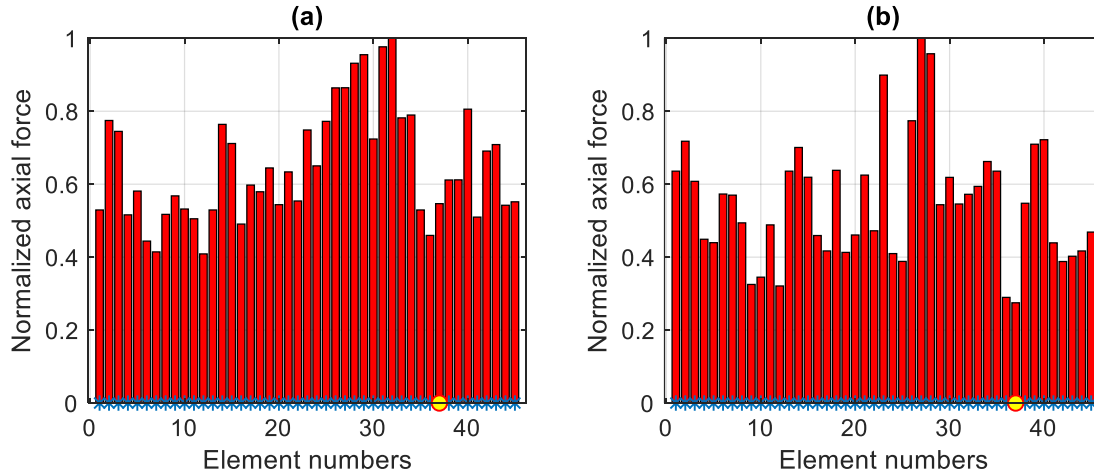


Figure 51: Case 1 using acceleration with 5% RMS noise and including: (a) Two modes (b) Three modes

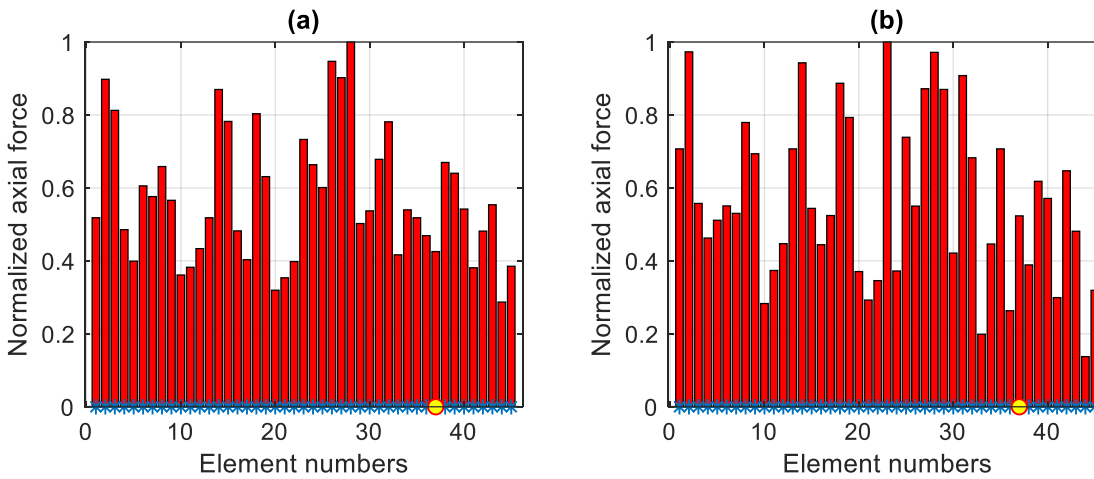


Figure 52: Case 1 using displacement with 5% RMS noise and including: (a) Two modes (b) Three modes

Case 2:

The damaged element in the second case is element 33, with a 30% reduction in the cross-sectional area. Even though the damage extent is less in this case than the first case, the change in fundamental frequency was 0.15%, as shown in Table 7. The mode shapes before and after the damage for this case are shown in Figure 53. Similar to the first case and due to using partial measurements, it is expected that element 44 will have a small axial force if element 33 has a small axial force to balance the vertical force at joint 23. The results in Figure 54 show the cumulative

axial force by applying the DLVs and show small axial forces for the damaged element 33. Similar to the first case, after adding measurement noise, the DLV method was not able to localize the damage, as shown in Figure 55 and Figure 56. For case 3 and case 4, the damage's level was increased to a 50% reduction in the cross-sectional area, and the DLV method was able to localize the damage successfully.

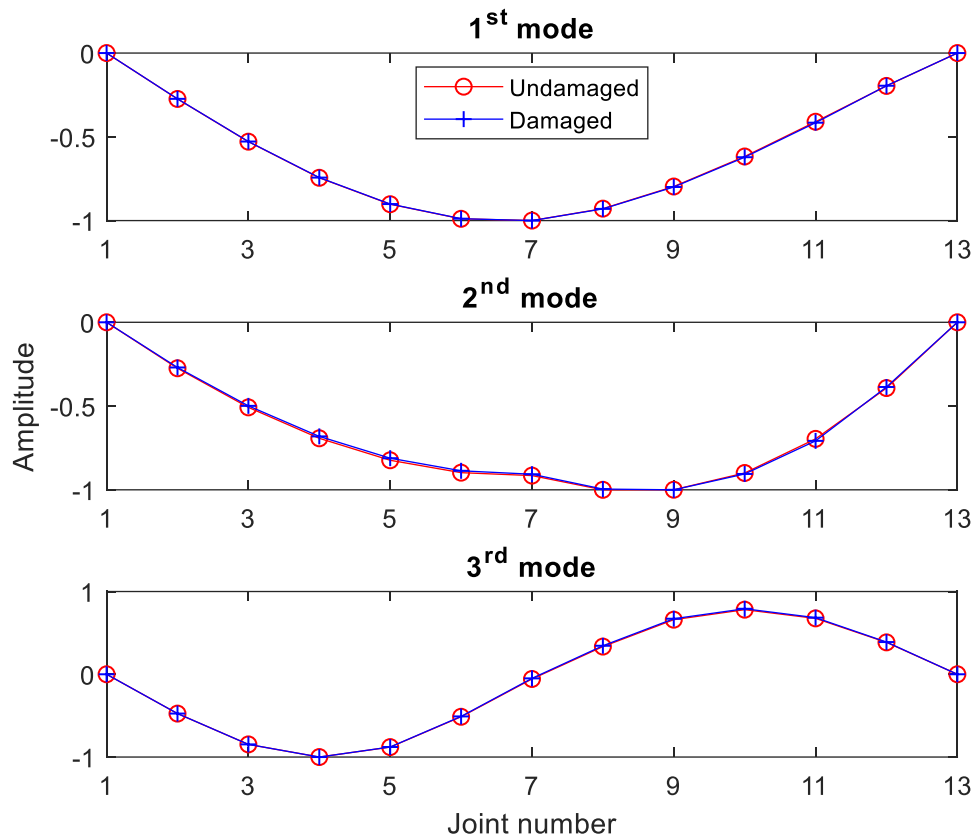


Figure 53: Mode shapes for case 2 (element 33 is damaged by 30%)

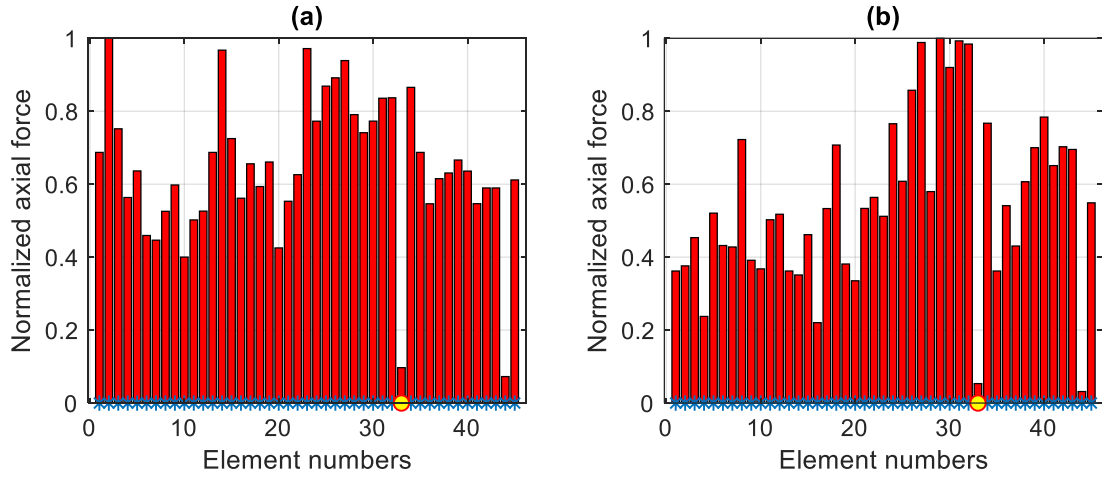


Figure 54: Case 2 using acceleration without noise and including: (a) Two modes (b) Three modes

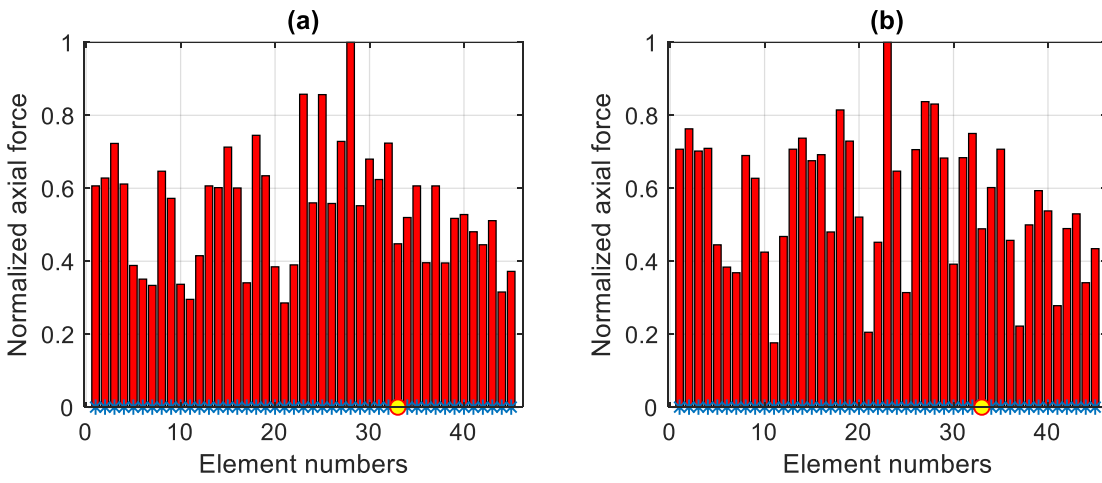


Figure 55: Case 2 using acceleration with 5% RMS noise and including: (a) Two modes (b) Three modes

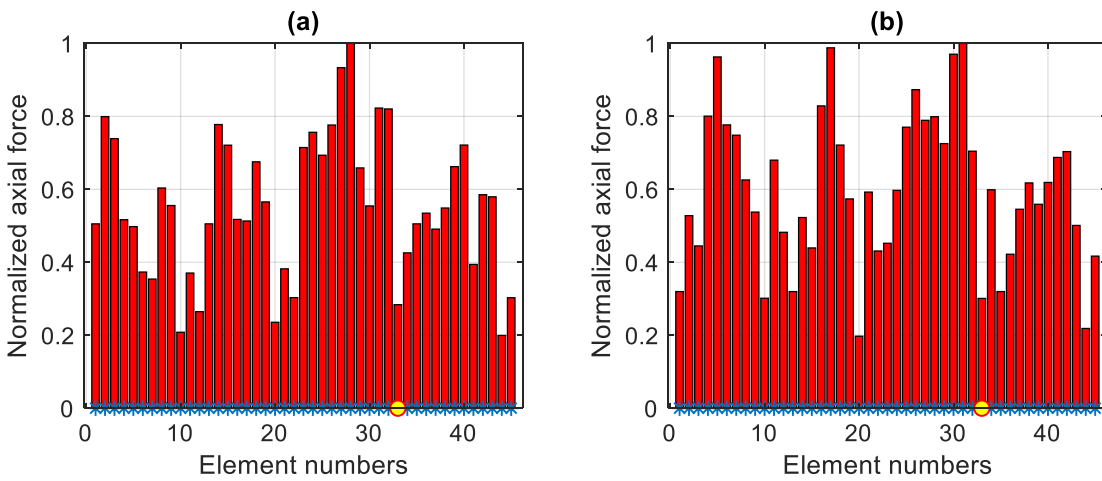


Figure 56: Case 2 using displacement with 5% RMS noise and including: (a) Two modes (b) Three modes

Case 3:

In this case, element 33 is damaged similar to the second case but with a 50% reduction in the cross-sectional area. The increase in the damage level increases the change in fundamental frequency from 0.15% to 0.45% (see Table 7). The rise in the damage level also results in a slightly higher difference in the mode shapes, shown in Figure 57. The damaged element 33 clearly shows small axial force using acceleration with noise (see Figure 58) and using displacement with noise (see Figure 59). Due to the relatively higher damage level in this case compared with the previous two cases, the damaged element was localized by including a few modes with the presence of noise.

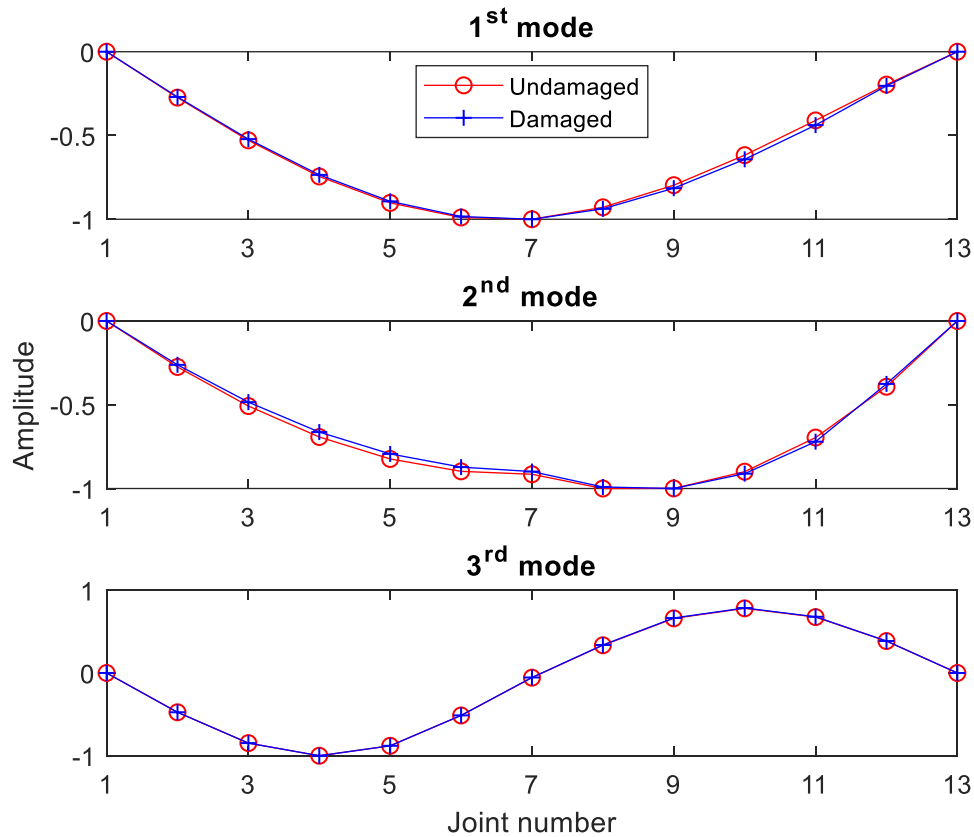


Figure 57: Mode shapes for case 3 (element 33 is damaged by 50%)

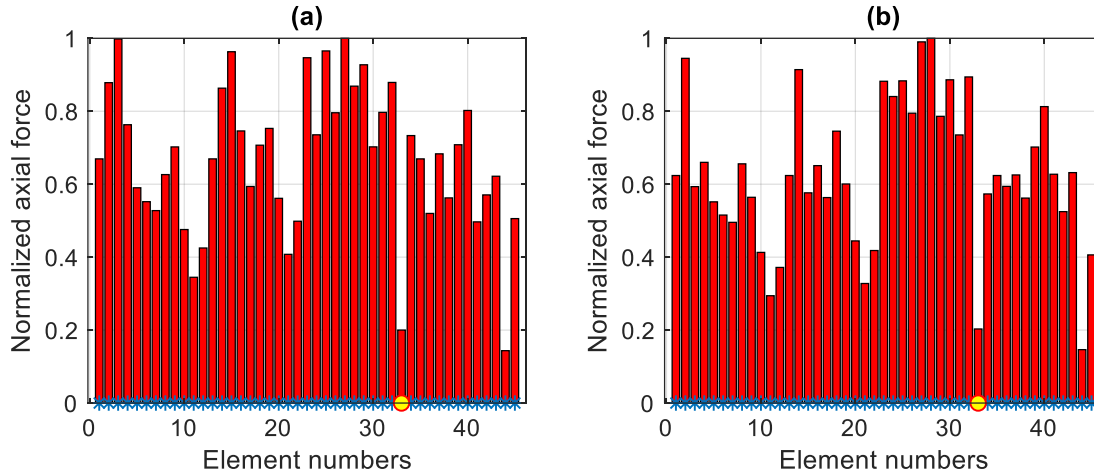


Figure 58: Case 3 using acceleration with 5% RMS noise and including: (a) Two modes (b) Three modes

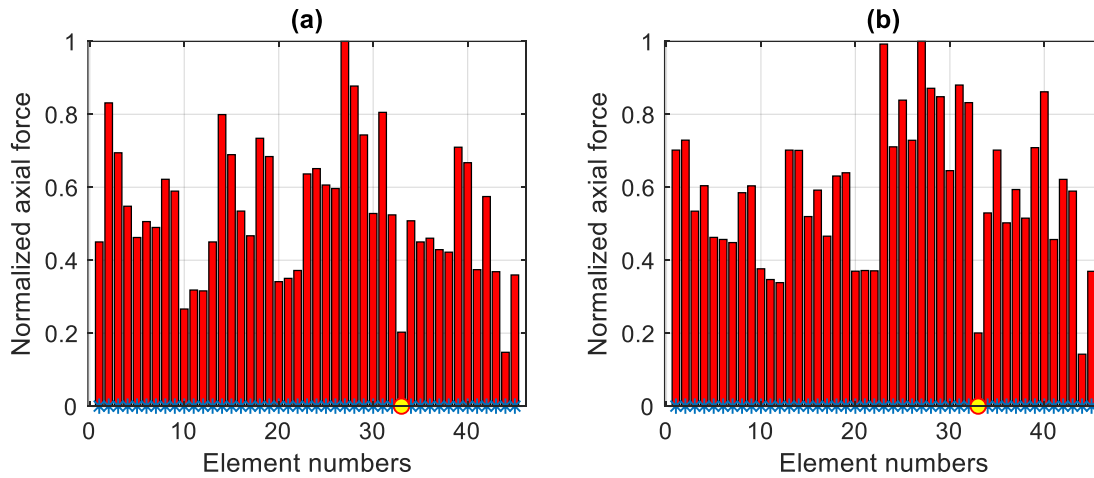


Figure 59: Case 3 using displacement with 5% RMS noise and including: (a) Two modes (b) Three modes

Case 4:

The fourth case induced 50 % damage to element 7, which led to a 2.3% change in the fundamental frequency. This change in frequency is the largest in comparison with the previous three cases. The mode shapes are shown in Figure 60, which shows a small difference around the midspan. The results from the DLVs using measurements without noise are shown in Figure 61. Due to the sensor configuration and to balance the vertical force at joint 7, both elements 6 and 7 show almost zero axial forces (see Figure 61). The damaged element was also successfully localized using measurements with noise and including only two and three modes (see Figure 62 and Figure 63).

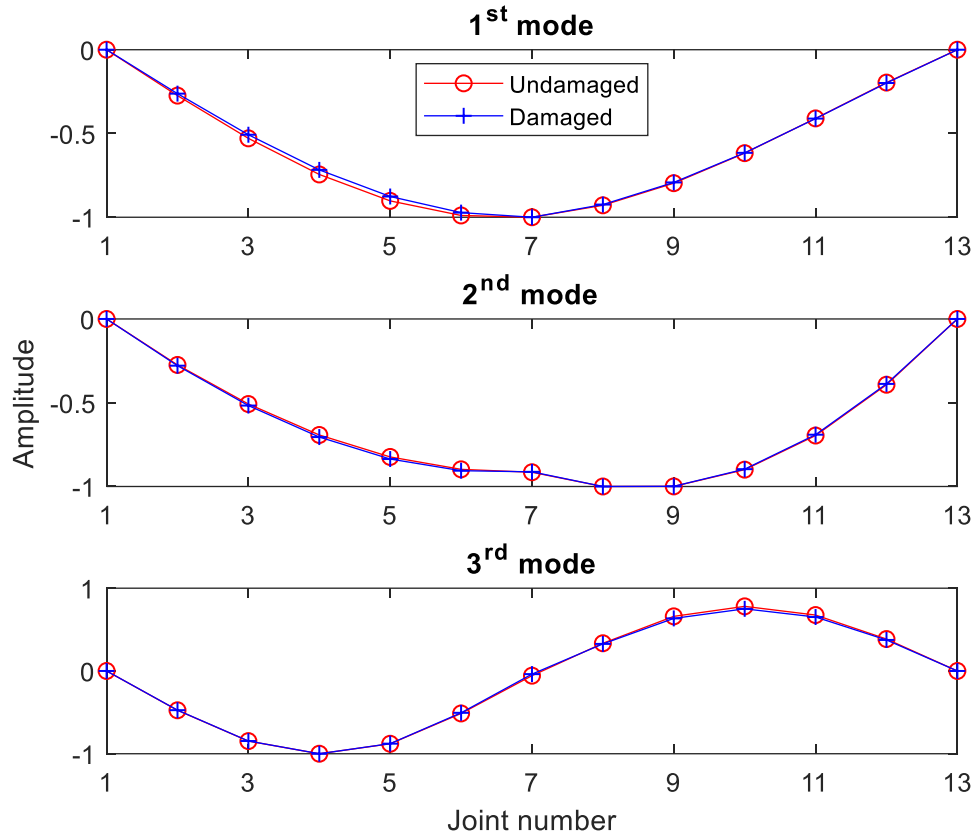


Figure 60: Mode shapes for case 4 (element 7 is damaged by 50%)

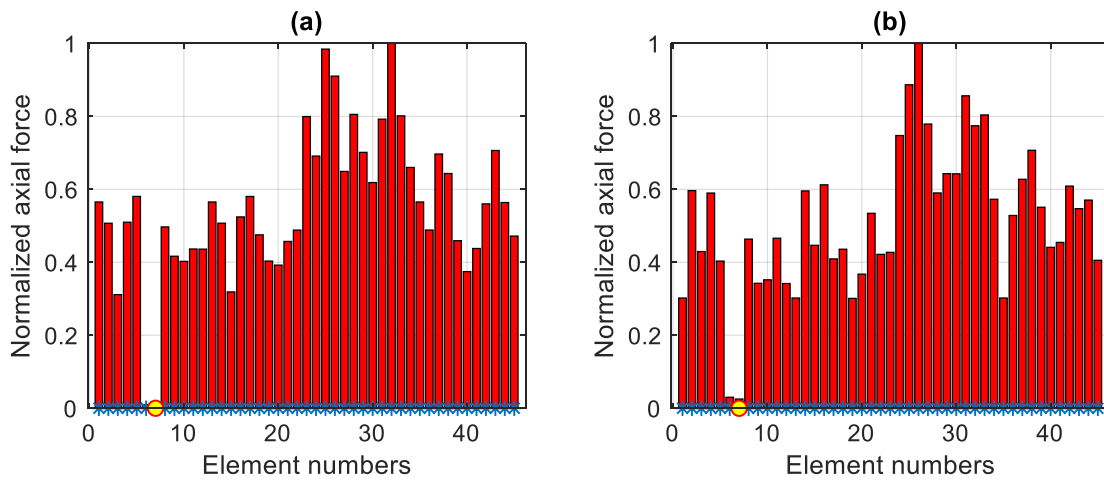


Figure 61: Case 4 using acceleration without noise and including: (a) Two modes (b) Three modes

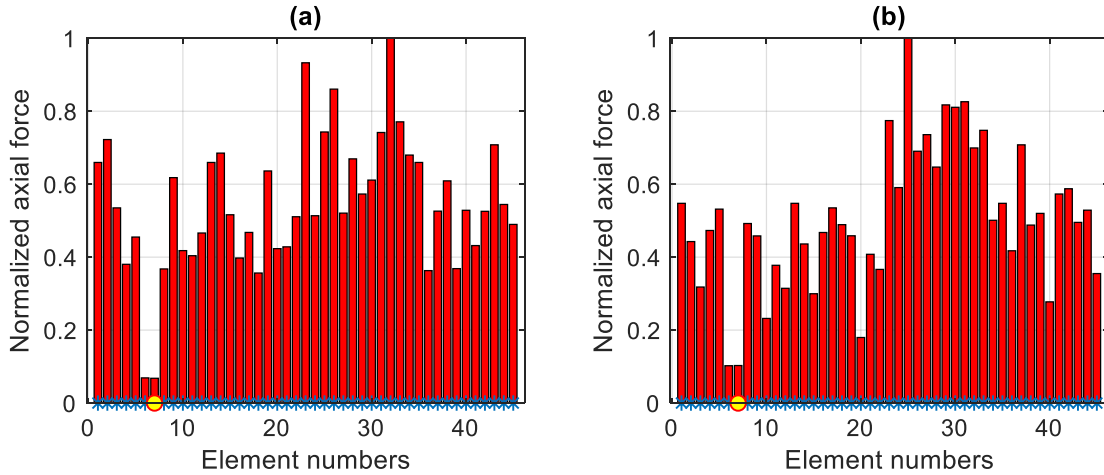


Figure 62: Case 4 using acceleration with 5% RMS noise and including: (a) Two modes (b) Three modes

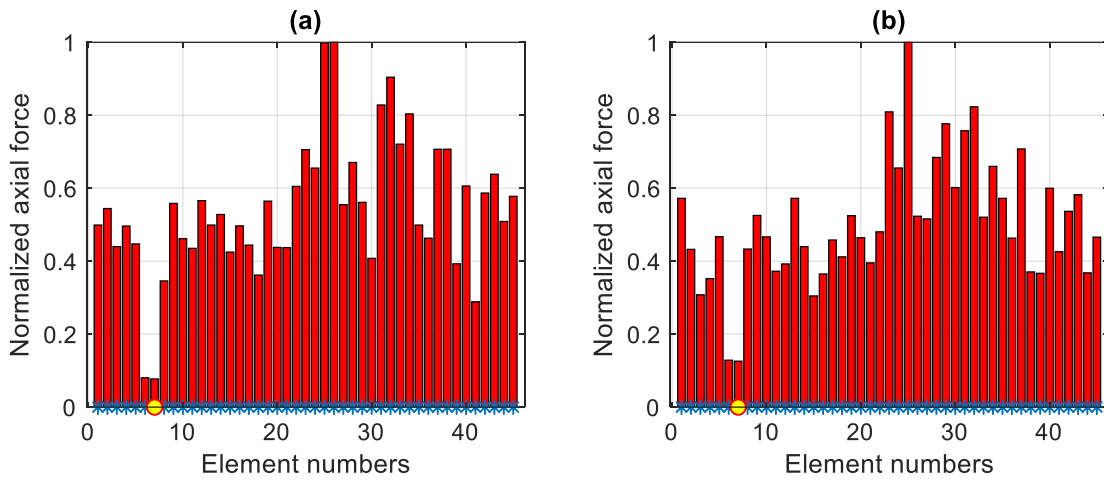


Figure 63: Case 4 using displacement with noise and including: (a) Two modes (b) Three modes

From the results of the four investigated cases, it can be observed that the computer vision has the potential to be used for damage identification. In the third and fourth cases, the damage was localized using only two or three modes that were estimated using the simulated computer vision response—the displacement measurements from SAP2000—with an added 5% noise. The numerical investigation considers the limitations of computer vision compared to traditional sensors, such as the sampling rate and the number of identified modes.

The number of the identified modes by computer vision and its accuracy can be affected by different factors. For example, the structure’s natural frequencies can impact the number of

identified modes, where stiffer structures are likely to have fewer modes identified. In the previous chapter (Chapter 4), two structures were experimentally identified using the proposed computer vision framework. For the small-scale 6-story structure, five modes were identified with high accuracy. However, only one mode was identified for the experimental 3-D truss. It is difficult to define a general limit for computer vision that can be applied for any test setup and any structure. Nevertheless, damage identification using computer vision is possible as long as the damage is significant enough to make a detectable change in the modal properties. In practice, it might not be possible to distinguish the difference in modal properties coming from insignificant damage with the small changes from other sources, such as noise or processing error. In addition, temporal-aliasing could be a practical challenge for computer vision. The following section (5.3.3) discusses the impact of temporal-aliasing on damage identification.

5.3.3. Practical challenge: temporal-aliasing for computer vision

The use of an inadequate sampling rate in collecting vibration measurements leads to misidentifying high frequencies (above the Nyquist frequency), which is known as temporal-aliasing. For traditional measurements, temporal-aliasing is avoided by using an anti-aliasing filter in the data acquisition system. However, typical computer vision devices do not have anti-aliasing filters. Consumer-level cameras can provide an adequate sampling rate to perform system identification for many civil engineering structures. However, since the consumer-level cameras have lower sampling rates than accelerometers and do not have anti-aliasing filters, this could potentially lead to aliasing the high-frequency modes.

This section investigates the impact of including aliased modes in damage identification using the DLV method. Element 33 is damaged by a 50% reduction in the cross-sectional area. The damaged element is successfully localized by including two and five modes, as shown in

Figure 64. In Figure 64 (a) and (b), the damage is successfully localized using actual modes with no aliasing. The damage is also localized by including one actual and one aliased mode, as shown in Figure 64 (c). In addition, the damage is localized by including one actual and four aliased modes, as shown in Figure 64 (d). Similarly, element 2 is damaged by a 50% reduction in the cross-sectional area, and the damage localized using actual and aliased modes, as shown in Figure 65.

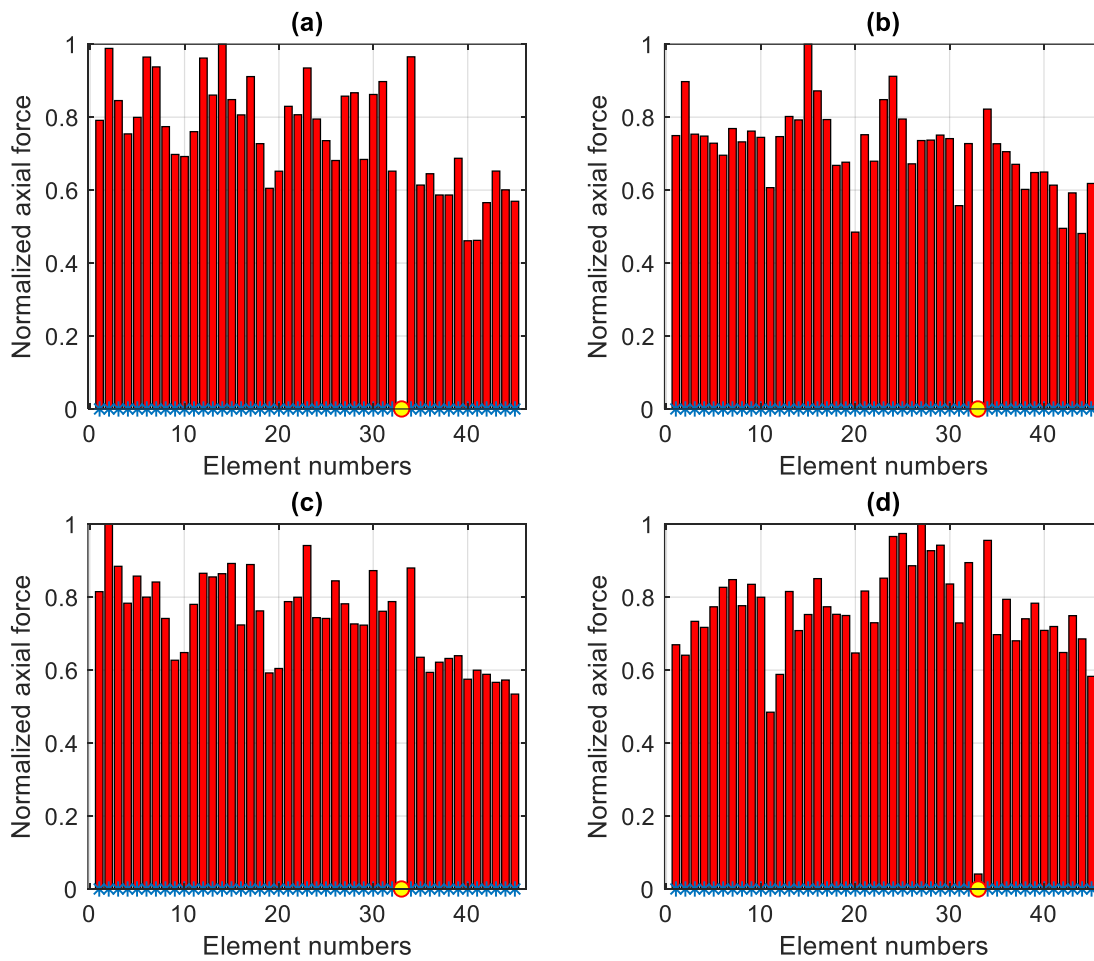


Figure 64: Damage identification for element 33 where: (a) Two actual modes are included. (b) Five actual modes are included. (c) One actual mode and one aliased mode are included. (d) One actual mode and four aliased modes are included.

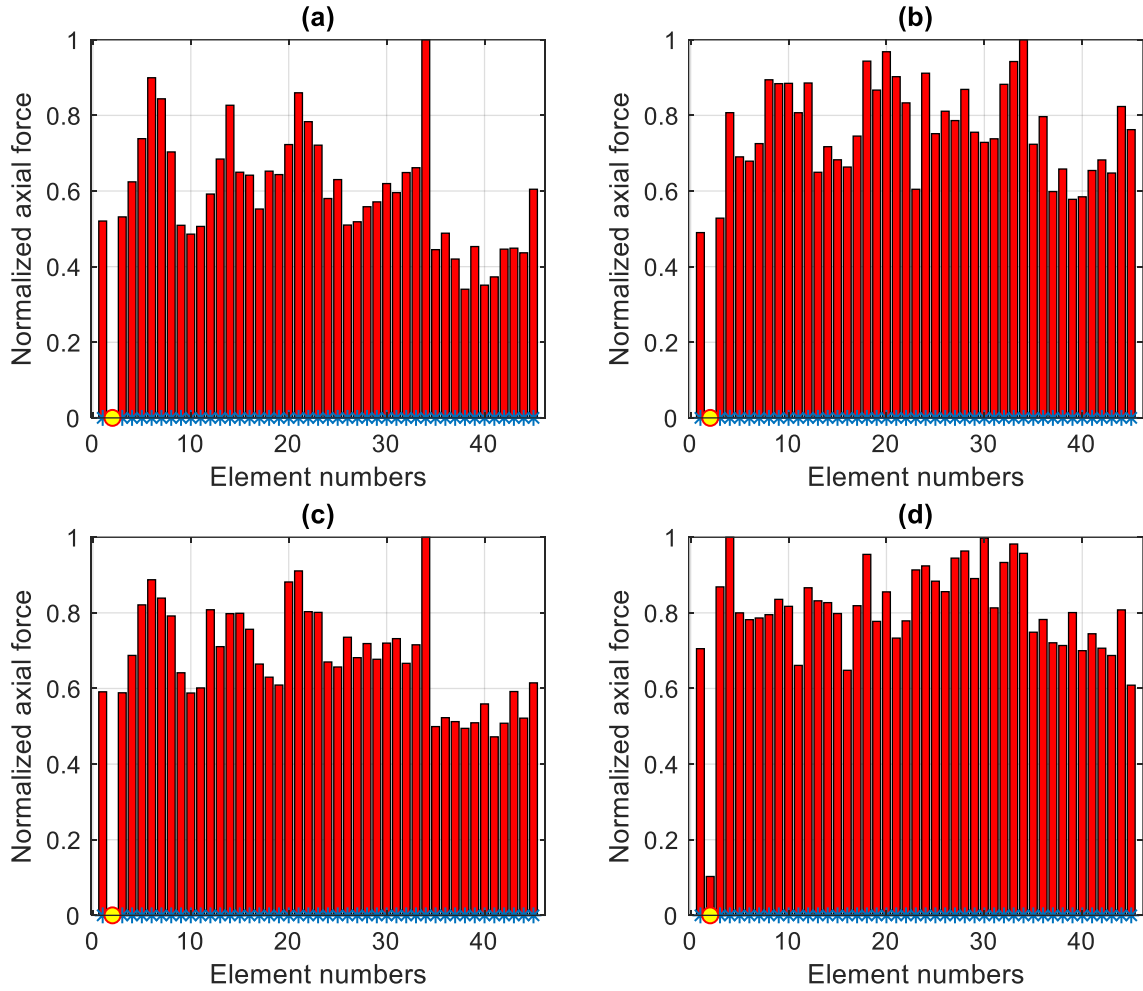


Figure 65: Damage identification for element 2 where: (a) Two actual modes are included. (b) Five actual modes are included. (c) One actual mode and one aliased mode are included. (d) One actual mode and four aliased modes are included.

In Figure 66, a more comprehensive range of aliased modes are included to show their impact on damage identification. The used sampling rate is 30 Hz, which can only capture the first mode of the truss structure, while all the other 19 modes are aliased. It can be observed from these results that including a few of the aliased modes could enhance the accuracy of damage identification. However, including a significant number of aliased modes lead to a large error in the damage identification. The author recommends including the modes below twice the sampling rate, instead of half of the sampling rate. Only the first three modes fall below the recommended limit ($2f_s = 60$ Hz) shown in Table 7. For this structure, the first three modes have a total of 95.4%

modal participation ratio. The induced error in the damage identification can be huge when including a large number of aliased modes. The inverse relationship between the square of the modal frequencies and the flexibility matrix is affected directly by including aliased modes. In other words, using aliased modes to construct the flexibility matrix changes the participation factors of the aliased modes.

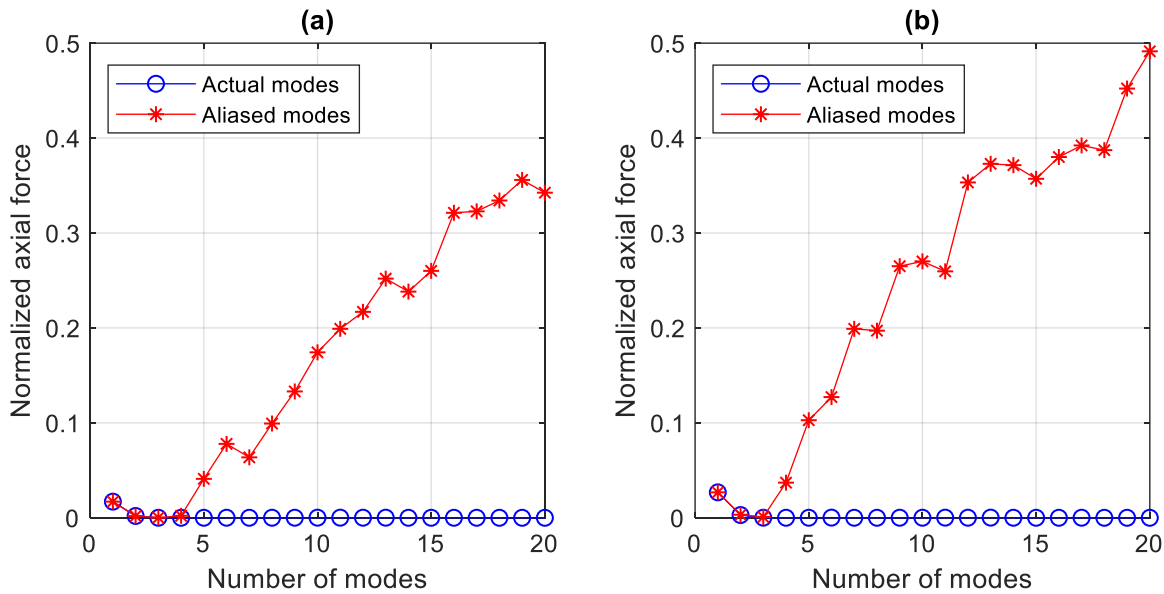


Figure 66: Damage identification for (a) Damaged element 33 and (b) Damaged element 2. Actual modes: included from 1 to 20 actual modes. Aliased modes: included from 1 to 20 aliased modes, where the first mode is actual, and the remaining 19 modes are aliased.

For field application on real structures, it is vital to consider the following three points. First, the accuracy of the reconstructed flexibility matrix from measurements is highly affected by the first few modes, while higher modes have a minimal contribution. Second, computer vision (and displacement measurements in general) have lower sensitivity to higher modes, discussed in 5.3.2. Third, the considered structure in the numerical (and the experimental) investigation is stiffer than real-world bridge structures. This means that real structures could have a few modes that can be captured with a low sampling rate (i.e., 30 Hz) without aliasing, as opposed to only the first mode that can be captured without aliasing in the considered structure in this study. For real

structures, the ratio of measured non-aliased to aliased modes should be higher than 1 to 44. By considering the previous three points for practical applications, it can be concluded that including a few aliased modes for damage localization will induce a relatively small error. Knowing that the induced error of including possibly aliased modes is small for damage localization, gives the potential to use computer vision.

Table 8: Actual and aliased first five modal frequencies of the truss bridge

Mode	Frequencies (Hz)		Note
	Actual	When using 30 Hz sampling rate	
1	13	13	non-aliased
2	42.7	12.7	aliased
3	59.8	0.2	aliased
4	84.6	5.4	aliased
5	125.9	5.9	aliased

5.4. Experimental investigation

5.4.1. Model description and test setup

The experimental truss bridge is used in this study with a similar test setup for system identification in 4.3.2 (see Figure 67). The elements are connected with the joints using two connectors at the ends to allow for element substitution, as shown in Figure 68. Damage is simulated by reducing the element's stiffness, which is by replacing it with an element with a smaller cross-sectional area.

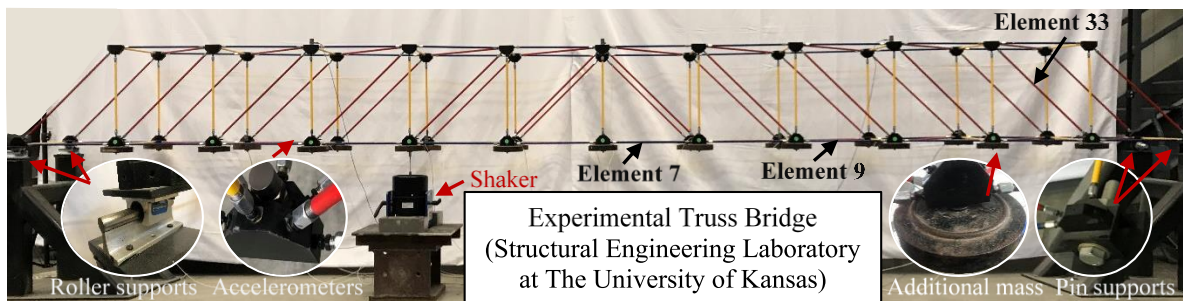


Figure 67: Test setup for damage identification (the locations of the substituted damaged elements are labeled)

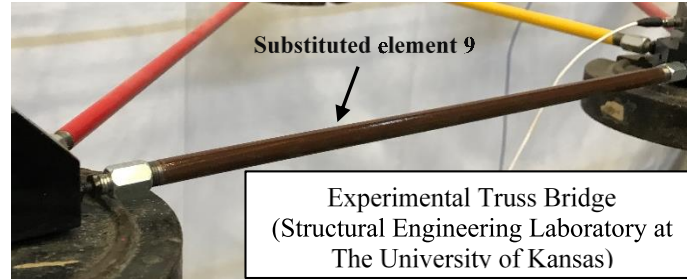


Figure 68: Substituted element 9, which has a 30% reduction in cross-sectional area

The structure is excited using BLWN excitation with the shaker, as shown in Figure 67. The excitation force has an amplitude of 20 pounds, similar to the input force in the numerical investigation (see Figure 43). The structural response is measured before and after the damage for the same measured DOFs in the numerical investigation (see Figure 48), which are the 11 vertical DOFs at the bottom chord of the front panel. From the findings in section 4.3.2.3, computer vision was able to identify only the first mode of the experimental truss bridge. Due to this limitation, the experimental results for damage identification considered only acceleration measurements.

5.4.2. Experimental results

The experimental investigation of damage identification included four cases for different damage scenarios. The damaged member is replaced on both panels (back and front panels) to achieve a more significant damage level, and the summary of the four cases is shown in Table 9. From the numerical results, it was observed that damage identification is difficult for cases with small damage when compared to those with significant damage. Similarly, the presented results show more potential for damage identification for cases with a significant damage level. These included cases have different damage levels at different locations.

Table 9: Summary of the experimentally investigated damage cases

	Damaged element	Reduction in the cross-sectional area	Change in the fundamental frequency	Results are shown in
Case 5	9	27%	0.47%	Figure 69 and Figure 70
Case 6	33	45%	0.5%	Figure 71 and Figure 72
Case 7	7	27%	0.8%	Figure 73 and Figure 74
Case 8	7	45%	2.7%	Figure 75 and Figure 76

Case 5:

In this case, element 9 was substituted with another element with a 27% smaller cross-sectional area. The change in the fundamental frequency of the structure due to damage was only 0.47%. The mode shapes before and after the damage from the measured acceleration are shown in Figure 69. The number of included mode shapes is limited to three modes, similar to the numerical investigation due to computer vision limitations.

The consumer-level cameras, such as the camera of the iPhone 7 used in Chapter 4, can provide a maximum sampling rate of 120 fps (or 120 Hz) for a reasonable resolution. For this reason and similar to the numerical investigation, the acceleration measurements were downsampled to 120 Hz. The difference in the mode shapes before and after the damage is minimal (see Figure 69). The results for damage identification using measured acceleration are shown in Figure 70. The normalized cumulative stresses in the damaged element from the DLVs was 0.5, which means the damaged element was not detected in this case.

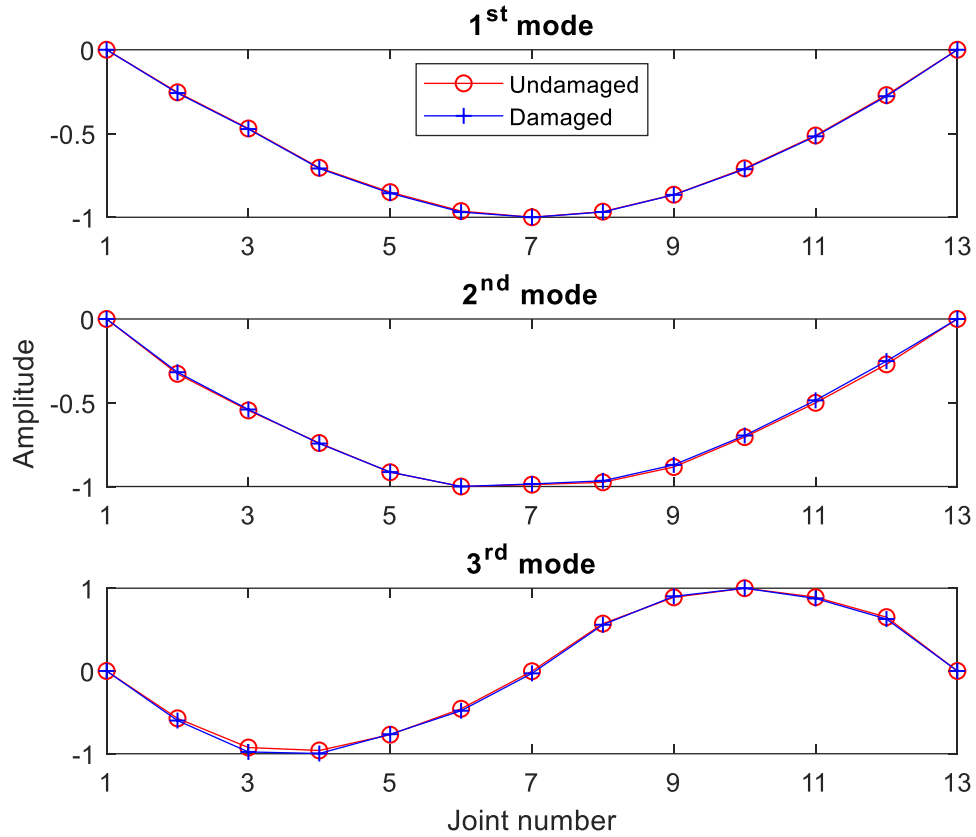


Figure 69: Mode shapes for case 5 from measured acceleration (element 9 is damaged by 27%)

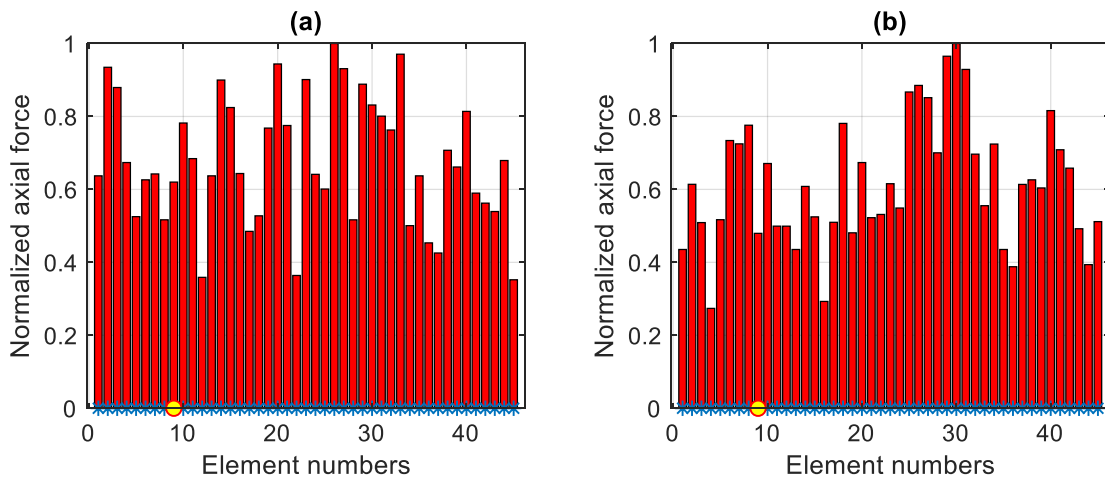


Figure 70: Case 5 using measured acceleration and including: (a) Two modes (b) Three modes

Case 6:

In the sixth case, element 33 is damaged by 45%, resulting in a 0.5% change in the fundamental frequency of the structure. The mode shapes for the undamaged and the damaged states are shown

in Figure 71. The damaged element was successfully identified in this case, as shown in Figure 72. The results in Figure 72 (a) show a small axial force for element 44, which is expected due to the vertical force balance at joint 23. This was also discussed in cases 2 and 3 in the numerical investigation. Elements 11 and 21, which are connected to elements 33 and 44, also show relatively small axial forces (see Figure 72 (b)).

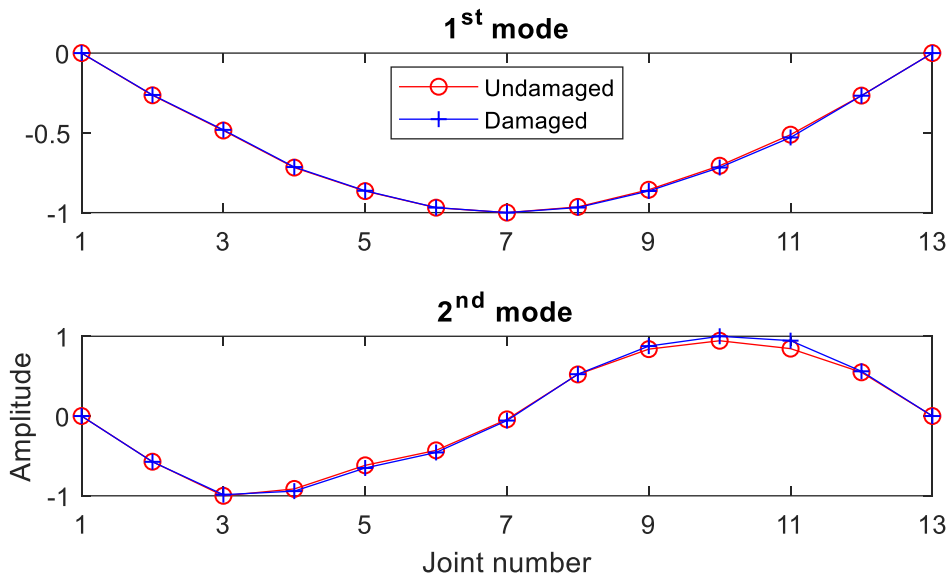


Figure 71: Mode shapes for case 6 from measured acceleration (element 33 is damaged by 45%)

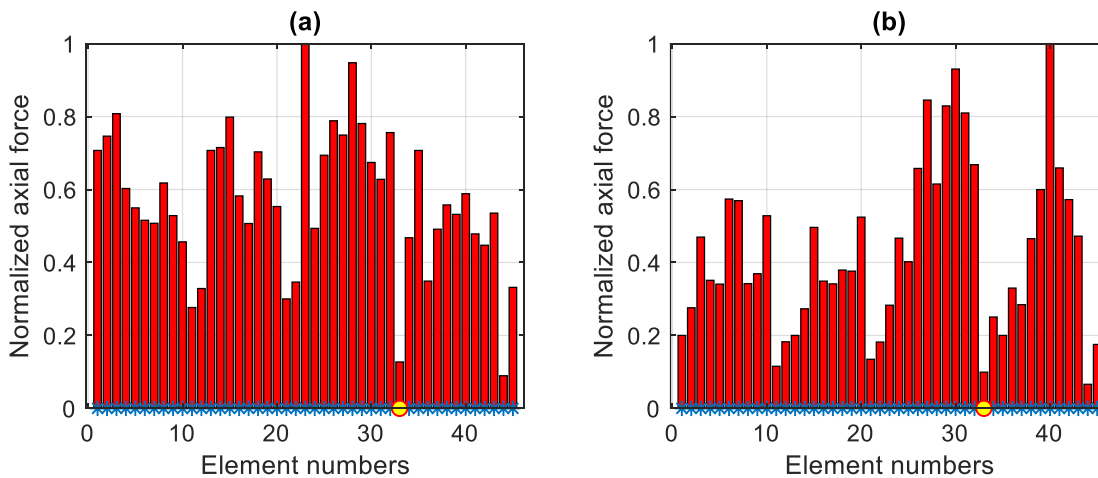


Figure 72: Case 6 using measured acceleration and including: (a) One mode (b) Two modes

Case 7:

In this case, element 7 is damaged by 27%, which results in a 0.8% change in the fundamental frequency. The identified mode shapes before and after the damage are shown in Figure 73. The calculated cumulative stress from the DLVs is shown in Figure 74. The damaged element has relatively high cumulative stresses of more than 0.4, which means the damaged element was not detected in this case. In the following case (case 8), the same element was damaged but with a larger reduction in cross-sectional area, which led to a successful damage identification.

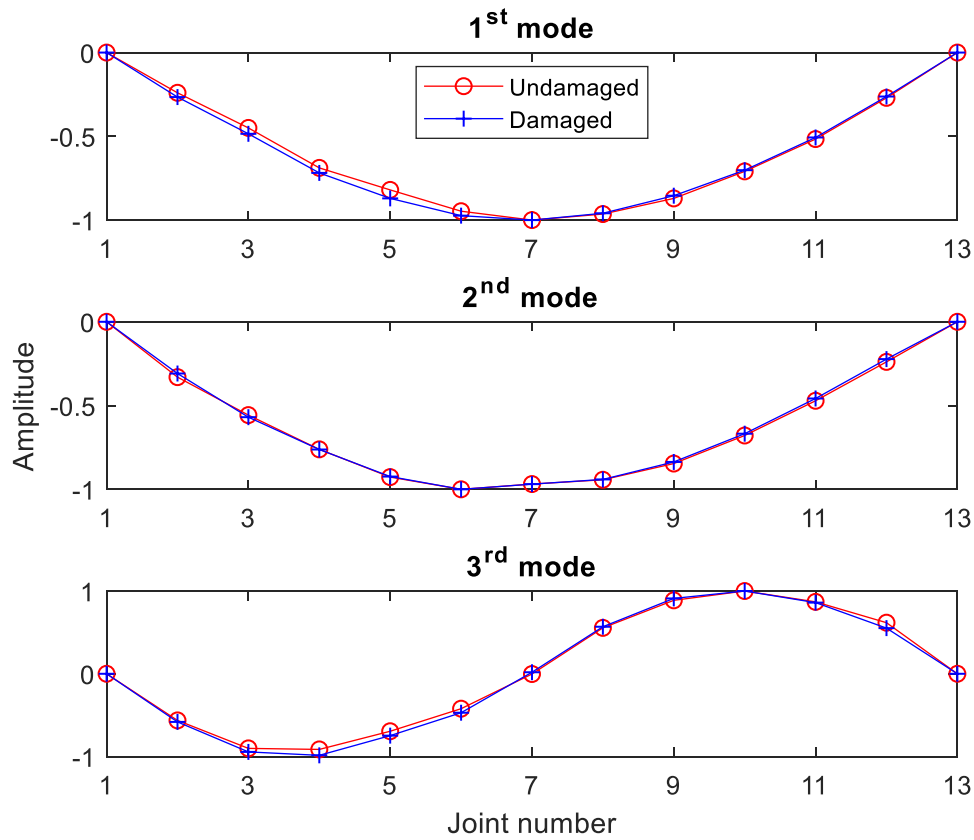


Figure 73: Mode shapes for case 7 from measured acceleration (element 7 is damaged by 27%)

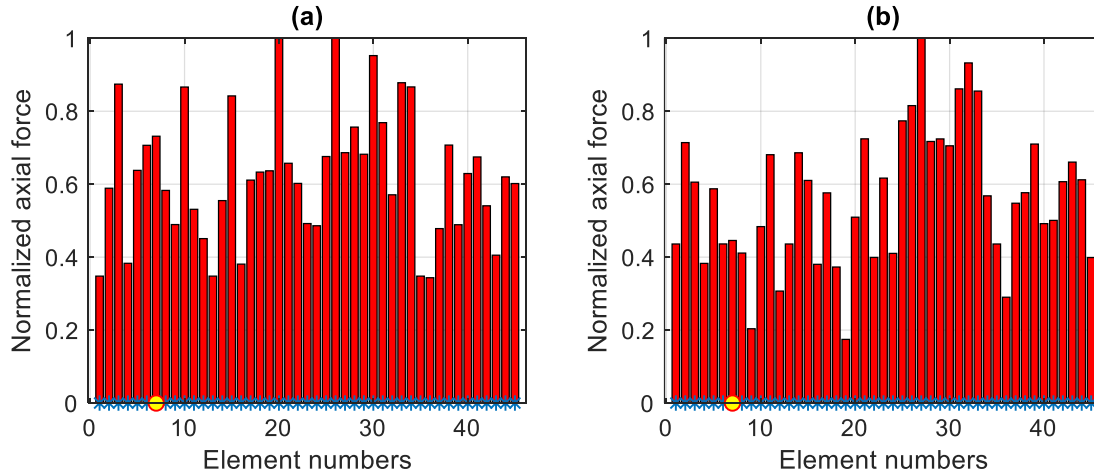


Figure 74: Case 7 using measured acceleration and including: (a) Two modes (b) Three modes

Case 8:

The last case in the experimental investigation reduced the cross-sectional area of element 7 by 45%, which is the same damaged element in case 7 but with a larger reduction in the cross-sectional area. This reduction led to a 2.7% change in the structure’s fundamental frequency, which is the largest change among the four investigated cases. The mode shapes before and after the damage are shown in Figure 75. The damaged element was successfully detected, as shown in Figure 76. When element 7 has a small axial force, it is expected that element 6 will have a small force due to force balance at joint 7.

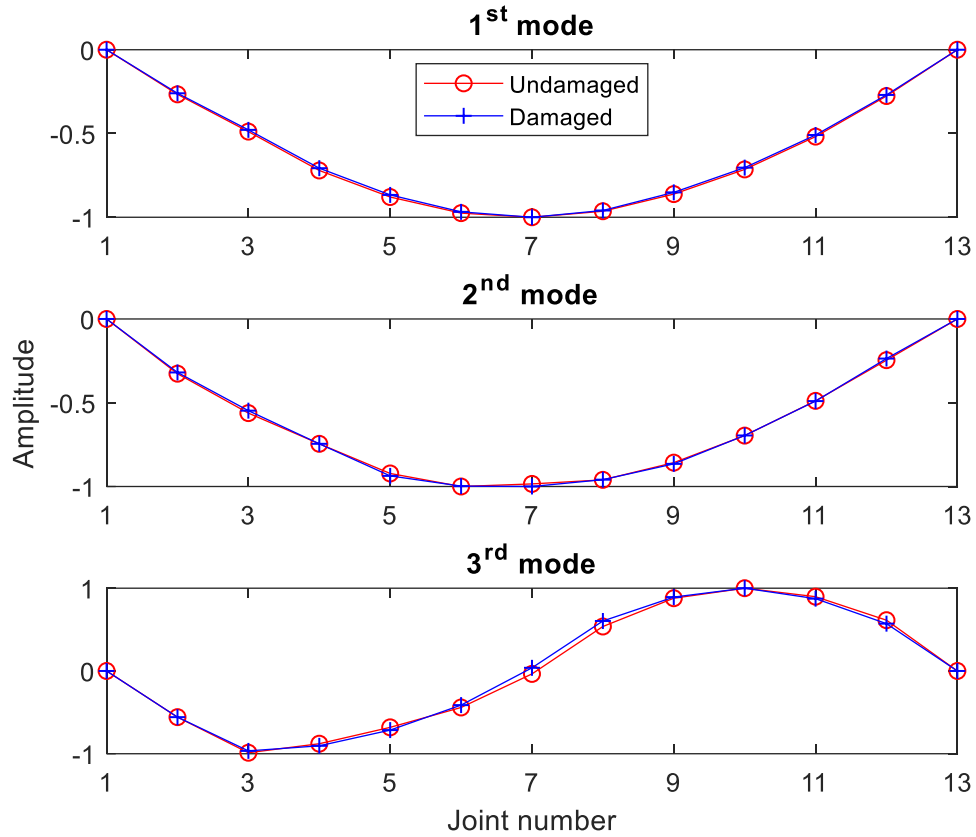


Figure 75: Mode shapes for case 8 from measured acceleration (element 7 is damaged by 45%)

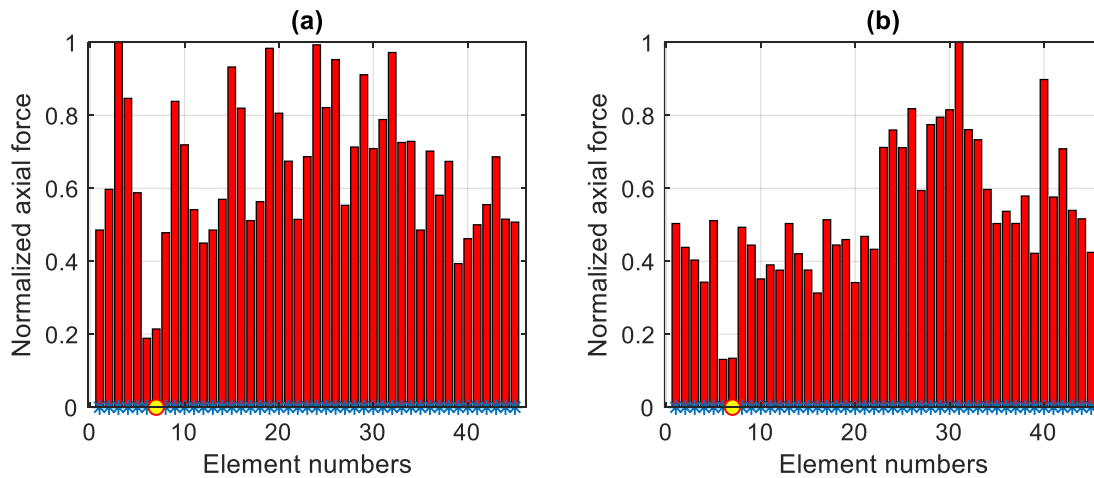


Figure 76: Case 8 using measured acceleration and including: (a) Two modes (b) Three modes

From the four cases in this experimental investigation, it can be seen that damage identification using only a few identified modes is possible when the damage level is relatively significant. However, it is important to recall that the structure used in this study has a higher

stiffness than most real-world bridge structures, discussed in section 4.3.2. As a result, it might be possible to detect less significant damages in a real-world bridge structure. This gives the potential for damage identification using computer vision. Identifying relatively small damage might be challenging in general, but it might be more challenging for computer vision due to its limitations.

5.5. Summary

This chapter discussed the importance of damage identification and provided a general overview of vibration-based damage identification methods. It also showed that the flexibility matrix could be constructed with high accuracy using fewer modes than the stiffness matrix. This feature is the primary motivator of using flexibility-based methods for damage identification.

The goal of this study is to investigate the possibility of using computer vision in damage identification. The presented numerical and experimental investigations in this study considered the limitations of computer vision that are discussed in Chapter 4. The computer vision method can be limited to identify a small number of modes for two reasons. First, the computer vision measure displacement, which is naturally has a lower sensitivity to high modes than acceleration. Second, the sampling rate of consumer-level cameras is significantly less than the sampling rate of accelerometers. These two reasons, separate or combined, can limit the computer vision ability to identify only a few modes. However, the ability of the computer vision method is also affected by several other factors—for example, the natural frequencies and the amount of motion of the structure. Also, the type of used camera can impact the ability of computer vision. In some situations, computer vision can achieve comparable results with the accelerometers. For example, in Chapter 4, the computer vision method was able to identify five modes with great accuracy for the 6-story structure. In other cases, the computer vision might be limited to identify a much fewer number of modes, which is the case for the experimental truss bridge in Chapter 4.

This study also investigated the impact of temporal-aliasing on damage identification, which is typically considered a potential challenge in using computer vision for system identification. The investigated cases showed that including a few aliased modes could improve the accuracy of damage identification. However, including a large number of aliased modes could induce a large error.

The results from the numerical and the experimental investigations using a 3-D truss structure were presented. The numerical and the experimental results showed the possibility of identifying the damage using only a few modes. The experimental investigation of this study used acceleration measurements from accelerometers to localize the damage. The damage could not be localized experimentally using the computer vision method because it only identified the fundamental mode of the truss structure. This limitation is due to the high stiffness of the experimental truss bridge used in this study compared to most of the real-world bridge structures, discussed in section 4.3.2. However, the ability to use a few modes to identify damage still gives the potential to use computer vision in damage identification for real-world structures.

CHAPTER 6: CONCLUSIONS AND FUTURE STUDIES

6.1. Conclusions

This dissertation presented improved strategies for Structural Health Monitoring (SHM) using traditional sensors and computer vision. The proposed strategies are important for the condition assessment of structures. Vibration-based assessment methods rely on measuring the structural response directly (i.e., peak displacements and accelerations) or using the structural response for change characterization (i.e., system and damage identifications). This research investigated three aspects of SHM that are important for response estimation and change characterization using both traditional sensors and computer vision.

The second chapter presented the background and literature review related to this research. This chapter also identified the gaps of knowledge in previous studies. It covered displacement estimation methods using acceleration, strain, and data fusion. In addition, it provided an overview of system identification and damage identification, focusing on computer vision methods.

The third chapter proposed two methods (data fusion A and data fusion B) to estimate the displacement of building structures under non-stationary wind loading. The proposed methods were able to estimate dynamic structural displacements, including a pseudo-static component, using acceleration and strain measurements. In particular, the proposed methods overcame the need for mass-normalized mode shapes to calculate displacements from strains. The two methods were validated using a numerical model of a 20-story moment frame structure with simulated measurement noise. Additionally, the proposed methods were validated experimentally using a small-scale 6-story structure subjected to wind load from two large fans. The estimated displacement from the proposed methods preserved the pseudo-static components. However, the

estimated displacement using only acceleration measurements showed a large error due to the missed pseudo-static components.

The fourth chapter proposed a method for system identification using computer vision. The proposed method overcame the main limitations, such as the need for large motion, special lighting conditions, and high-speed cameras. The mode shape extraction has two options in the proposed method; the first option (Option A) relied on the tracked displacement from the Kanade-Lucas-Tomasi (KLT) method, and the second option (Option B) combined the KLT with the Phase-Based Motion Processing (PBMP) method. The proposed method also included special guidelines for pre-recording and post-processing steps. The proposed framework was validated experimentally using two structures: a small-scale 6-story building and a single-span truss bridge. The results from the proposed framework, for both Options A and B, showed great potential for using computer vision in system identification.

The fifth chapter investigated the possibility of using computer vision for damage identification. This chapter adopted the damage locating vector (DLV) method. The numerical and experimental investigation used the same experimental truss bridge of Chapter 4. Additionally, the investigation accounted for the limitations of computer vision in system identification from Chapter 4. For example, computer vision relies on displacement measurements, which have a lower sensitivity to high modes than acceleration measurements. This lower sensitivity can lead to a lower number of identified modes. The number of identified modes (before and after damage) directly impacts damage identification accuracy. As a result, this chapter considered using a few modes for damage identification to account for the limitation of computer vision. This chapter also investigated the impact of including temporally-aliased modes for damage identification. Based on the investigated cases, the damage identification can benefit from including a few aliased

modes. However, including a large number of aliased modes might induce a large error. The experimental investigation of Chapter 5 localized the damage using the measured response from the accelerometers. The experimental results of this study did not use computer vision to localize damage because of its limitations, where it only identified the fundamental mode of the truss bridge. However, the ability to use a few modes to identify damage (using accelerometers) still gives the potential to use computer vision in damage identification for real-world structures, especially for cases with relatively significant damage levels.

6.2. Future Studies

This research provided improved strategies for SHM using traditional sensors and using computer vision. The proposed research addressed a few of the existing limitations and challenges. However, several others still require further investigation and improvement. These limitations and the direction for future studies are discussed below.

The proposed method for system identification using computer vision showed the great potential for reaching comparable results to those obtained from accelerometers. The proposed method used a consumer-level camera not specifically designed to monitor the structural response. Consumer-level cameras specifications have changed and improved quickly with many emerging features. As a result, the recommended guidelines for their use might require regular updates to account for these changes. In addition, the proposed method is currently limited to post-processing. Further investigation and adjustments are likely needed to use the proposed method in long-term automated monitoring.

The damage identification study showed some potential for using computer vision in damage identification. This study numerically investigated the impact of temporally-aliased modes on damage identification. The numerical results showed the potential of including some aliased

modes in damage identification. An experimental investigation of this issue is still needed to confirm the findings from the numerical investigation. Additionally, the experimental investigation of this study did not use computer vision measurements due to the high fundamental frequency (>10 Hz) of the truss bridge. However, this study used experimentally measured responses from the accelerometers. Additional experimental investigation using a real-world structure or a representative experimental structure is needed to validate the ability to use computer vision in damage identification.

REFERENCES

1. Abdelrazaq, A., *Validating the Structural Behavior and Response of Burj Khalifa: Synopsis of the Full Scale Structural Health Monitoring Programs*. International Journal of High-Rise Buildings, 2012. **1**(1): p. 37-51.
2. Agdas, D., J.A. Rice, J.R. Martinez, and I.R. Lasa, *Comparison of Visual Inspection and Structural-Health Monitoring as Bridge Condition Assessment Methods*. Journal of Performance of Constructed Facilities, 2016. **30**(3): p. 04015049(1)-04015049(10).
3. Aktan, A., K. Lee, C. Chuntavan, and T. Aksel. *Modal Testing for Structural Identification and Condition Assessment of Constructed Facilities*. in Proceedings-SPIE the International Society for Optical Engineering. 1994. p. 462-462.
4. Allemang, R.J. and D.L. Brown. *A Correlation Coefficient for Modal Vector Analysis*. in Proceedings of the 1st international modal analysis conference. 1982. SEM Orlando. p. 110-116.
5. Almarshad, A. *Building Drift Estimation Using Acceleration and Strain Measurements*. The University of Kansas, Lawrence, Kansas, USA. Master Thesis, 2017
6. Alvandi, A. and C. Cremona, *Assessment of Vibration-Based Damage Identification Techniques*. Journal of Sound and Vibration, 2006. **292**(1-2): p. 179-202.
7. Annamdas, V.G.M., S. Bhalla, and C.K. Soh, *Applications of Structural Health Monitoring Technology in Asia*. Structural Health Monitoring, 2017. **16**(3): p. 324-346.
8. ASCE7-16, *Minimum Design Loads and Associated Criteria for Buildings and Other Structures*. 2017, Reston, VA: American Society of Civil Engineers.

9. Barrish Jr, R.A., K.A. Grimmelsman, and A.E. Aktan. *Instrumented Monitoring of the Commodore Barry Bridge*. in *Nondestructive evaluation of highways, utilities, and pipelines IV*. 2000. International Society for Optics and Photonics. p. 112-126.
10. Baruch, M. and I.Y. Bar Itzhack, *Optimal Weighted Orttiogonalization of Measured Modes*. American Institute of Aeronautics and Astronautics Journal, 1978. **16**(4): p. 346-351.
11. Basseville, M. and I.V. Nikiforov, *Detection of Abrupt Changes: Theory and Application*. Vol. 104. 1993: Prentice Hall Englewood Cliffs.
12. Bendat, J.S. and A.G. Piersol, *Engineering Applications of Correlation and Spectral Analysis*. New York, Wiley-Interscience. 1980.
13. Bernal, D., *Load Vectors for Damage Localization*. Journal of Engineering Mechanics, 2002. **128**(1): p. 7-14.
14. Bernal, D., *Modal Scaling from Known Mass Perturbations*. Journal of Engineering Mechanics, 2004. **130**(9): p. 1083-1088.
15. Boggs, D. and A. Lepage, *Wind Tunnel Methods*. Special Publication, 2006. **240**: p. 125-142.
16. Boore, D.M., *Analog-to-Digital Conversion as a Source of Drifts in Displacements Derived from Digital Recordings of Ground Acceleration*. Bulletin of the Seismological Society of America, 2003. **93**(5): p. 2017-2024.
17. Boore, D.M., *Effect of Baseline Corrections on Displacements and Response Spectra for Several Recordings of the 1999 Chi-Chi, Taiwan, Earthquake*. Bulletin of the Seismological Society of America, 2001. **91**(5): p. 1199-1211.

18. Brincker, R. and P. Andersen. *A Way of Getting Scaled Mode Shapes in Output Only Modal Testing*. in Proceedings 21st International Modal Analysis Conference, Kissimmee, FL. 2003.
19. Brincker, R., J. Rodrigues, P. Andersen, and S.V.S. Aps, *Scaling the Mode Shapes of a Building Model by Mass Changes*. Proceeding of the 22nd IMAC, 2004: p. 119-126.
20. Brincker, R., L. Zhang, and P. Andersen, *Modal Identification of Output-Only Systems Using Frequency Domain Decomposition*. Smart Materials and Structures, 2001. **10**(3): p. 441.
21. Browning, J., B. Warden, A. Matamoros, and A. Lepage, *Global and Local Seismic Drift Estimates for Rc Frames*. Engineering Structures, 2008. **30**(5): p. 1262-1271.
22. Brownjohn, J.M., A. De Stefano, Y.-L. Xu, H. Wenzel, and A.E. Aktan, *Vibration-Based Monitoring of Civil Infrastructure: Challenges and Successes*. Journal of Civil Structural Health Monitoring, 2011. **1**(3-4): p. 79-95.
23. Caetano, E., S. Silva, and J. Bateira, *A Vision System for Vibration Monitoring of Civil Engineering Structures*. Experimental Techniques, 2011. **35**(4): p. 74-82.
24. Carden, E.P. and P. Fanning, *Vibration Based Condition Monitoring: A Review*. Structural health monitoring, 2004. **3**(4): p. 355-377.
25. Chaudhary, M.T.A., M. Abe, Y. Fujino, and J. Yoshida, *System Identification of Two Base-Isolated Bridges Using Seismic Records*. Journal of Structural Engineering, 2000. **126**(10): p. 1187-1195.
26. Chen, J.C. and J.A. Garba, *On-Orbit Damage Assessment for Large Space Structures*. AIAA Journal, 1988. **26**(9): p. 1119-1126.

27. Chen, J.G., T.M. Adams, H. Sun, E.S. Bell, and O. Büyüköztürk, *Camera-Based Vibration Measurement of the World War I Memorial Bridge in Portsmouth, New Hampshire*. Journal of Structural Engineering, 2018. **144**(11): p. 04018207.
28. Cho, S., C.-B. Yun, and S.-H. Sim, *Displacement Estimation of Bridge Structures Using Data Fusion of Acceleration and Strain Measurement Incorporating Finite Element Model*. Smart Structures and Systems, 2015. **15**(3-4): p. 645-663.
29. Coppotelli, G., *On the Estimate of the Frfs from Operational Data*. Mechanical Systems and Signal Processing, 2009. **23**(2): p. 288-299.
30. Cornwell, P., S.W. Doebling, and C.R. Farrar, *Application of the Strain Energy Damage Detection Method to Plate-Like Structures*. Journal of Sound and Vibration, 1999. **224**(2): p. 359-374.
31. CSI, *Sap2000 (Version 18) Integrated Solution for Structural Analysis and Design—CSI Analysis Reference Manual*. Computers and Structures, Inc, 2015.
32. Davenport, A., *How Can We Simplify and Generalize Wind Loads?* Journal of Wind Engineering and Industrial Aerodynamics, 1995. **54**: p. 657-669.
33. Doebling, S.W., *Minimum-Rank Optimal Update of Elemental Stiffness Parameters for Structural Damage Identification*. AIAA Journal, 1996. **34**(12): p. 2615-2621.
34. Doebling, S.W., C.R. Farrar, and M.B. Prime, *A Summary Review of Vibration-Based Damage Identification Methods*. Shock and Vibration Digest, 1998. **30**(2): p. 91-105.
35. Doebling, S.W., L.D. Peterson, and K.F. Alvin, *Experimental Determination of Local Structural Stiffness by Disassembly of Measured Flexibility Matrices*. Transactions-American Society of Mechanical Engineers Journal of Vibration And Acoustics, 1998. **120**: p. 949-957.

36. Dong, C.-Z. and F.N. Catbas, *A Review of Computer Vision–Based Structural Health Monitoring at Local and Global Levels*. Structural Health Monitoring, 2020: p. 1475921720935585.
37. Dragovich, J.J. and A. Lepage, *Fde Index for Goodness - of - Fit between Measured and Calculated Response Signals*. Earthquake Engineering and Structural Dynamics, 2009. **38**(15): p. 1751-1758.
38. Fan, W. and P. Qiao, *Vibration-Based Damage Identification Methods: A Review and Comparative Study*. Structural Health Monitoring, 2011. **10**(1): p. 83-111.
39. Farrar, C., S. Doebling, and T. Duffey. *Vibration-Based Damage Detection*. in SD2000, Structural Dynamics Forum. 1999. p. 11-17.
40. Farrar, C.R. and D.A. Jauregui, *Comparative Study of Damage Identification Algorithms Applied to a Bridge: I. Experiment*. Smart Materials and Structures, 1998. **7**(5): p. 704.
41. Farrar, C.R. and K. Worden, *An Introduction to Structural Health Monitoring*. Philosophical Transactions of the Royal Society A: Mathematical, Physical and Engineering Sciences, 2007. **365**(1851): p. 303-315.
42. Federal Emergency Management Agency, U.S., *Prestandard and Commentary for the Seismic Rehabilitation of Buildings*. 2008, Revised Feb. 2008. Washington, DC: FEMA, 2008.
43. Felber, A.J. *Development of a Hybrid Bridge Evaluation System*. University of British Columbia, Vancouver, Canada. , PhD Thesis, 1993
44. Foss, G. and E. Haugse. *Using Modal Test Results to Develop Strain to Displacement Transformations*. in Proceedings of the 13th international modal analysis conference. 1995. p. 112.

45. Fox, C. *The Location of Defects in Structures-a Comparison of the Use of Natural Frequency and Mode Shape Data*. in the 10th International Modal Analysis Conference. 1992. p. 522-528.
46. Friswell, M. and J.E. Mottershead, *Finite Element Model Updating in Structural Dynamics*. Vol. 38. 1995: Springer Science and Business Media.
47. Fu, Z.-F. and J. He, *Modal Analysis*. 2001: Elsevier.
48. G.V. Berg and G.W. Housner, *Integrated Velocity and Displacement of Strong Earthquake Ground Motion*. Bulletin of the Seismological Society of America, 1961. **51**(2): p. 175-189.
49. Gao, Y. and B.F. Spencer Jr, *Structural Health Monitoring Strategies for Smart Sensor Networks*. 2008, Newmark Structural Engineering Laboratory. University of Illinois at Urbana-Champaign.
50. Gindy, M., H.H. Nassif, and J. Velde, *Bridge Displacement Estimates from Measured Acceleration Records*. Transportation Research Record, 2007. **2028**(1): p. 136-145.
51. Guan, S., J.A. Bridge, C. Li, and N.J. DeMello, *Smart Radar Sensor Network for Bridge Displacement Monitoring*. Journal of Bridge Engineering, 2018. **23**(12): p. 04018102.
52. Guo, Y., D.K. Kwon, and A. Kareem, *Near-Real-Time Hybrid System Identification Framework for Civil Structures with Application to Burj Khalifa*. Journal of Structural Engineering, 2016. **142**(2): p. 04015132.
53. Harmanci, Y.E., U. Gülan, M. Holzner, and E. Chatzi, *A Novel Approach for 3d-Structural Identification through Video Recording: Magnified Tracking*. Sensors, 2019. **19**(5): p. 1229.

54. Housner, G., L.A. Bergman, T.K. Caughey, A.G. Chassiakos, R.O. Claus, S.F. Masri, R.E. Skelton, T. Soong, B. Spencer, and J.T. Yao, *Structural Control: Past, Present, and Future*. Journal of Engineering Mechanics, 1997. **123**(9): p. 897-971.
55. Housner, G.W., *Ground Displacement Computed from Strong-Motion Accelerograms*. Bulletin of the Seismological Society of America, 1947. **37**(4): p. 299-305.
56. Housner, G.W., L.A. Bergman, T.K. Caughey, A.G. Chassiakos, R.O. Claus, S.F. Masri, R.E. Skelton, T. Soong, B. Spencer, and J.T. Yao, *Structural Control: Past, Present, and Future*. Journal of Engineering Mechanics, 1997. **123**(9): p. 897-971.
57. Huang, G. *Probabilistic Analysis of Load Effects on Tall Buildings under Stationary and Nonstationary Extreme Winds*. 2008
58. Irvine, T., *Effective Modal Mass and Modal Participation Factors*. 2015.
59. Iwan, W.D., M.A. Moser, and C.-Y. Peng, *Some Observations on Strong-Motion Earthquake Measurement Using a Digital Accelerograph*. Bulletin of the Seismological Society of America, 1985. **75**(5): p. 1225-1246.
60. Jo, H., S.H. Sim, A. Tatkowski, B. Spencer, and M.E. Nelson, *Feasibility of Displacement Monitoring Using Low - Cost Gps Receivers*. Structural Control and Health Monitoring, 2013. **20**(9): p. 1240-1254.
61. Juang, J.N. and R.S. Pappa, *An Eigensystem Realization Algorithm for Modal Parameter Identification and Model Reduction*. Journal of Guidance, Control, and Dynamics, 1985. **8**(5): p. 620-627.
62. Kabe, A.M., *Stiffness Matrix Adjustment Using Mode Data*. AIAA Journal, 1985. **23**(9): p. 1431-1436.

63. Kaloop, M.R., E. Elbeltagi, J.W. Hu, and A. Elrefai, *Recent Advances of Structures Monitoring and Evaluation Using Gps-Time Series Monitoring Systems: A Review*. ISPRS International Journal of Geo-Information, 2017. **6**(12): p. 382.
64. Kang, L.-H., D.-K. Kim, and J.-H. Han, *Estimation of Dynamic Structural Displacements Using Fiber Bragg Grating Strain Sensors*. Journal of sound and vibration, 2007. **305**(3): p. 534-542.
65. Kareem, A., L. Hu, Y. Guo, and D.-K. Kwon, *Generalized Wind Loading Chain: Time-Frequency Modeling Framework for Nonstationary Wind Effects on Structures*. Journal of Structural Engineering, 2019. **145**(10): p. 04019092.
66. Kawashima, K., G.A. MacRae, J.-i. Hoshikuma, and K. Nagaya, *Residual Displacement Response Spectrum*. Journal of Structural Engineering, 1998. **124**(5): p. 523-530.
67. Kong, X. and J. Li, *Vision - Based Fatigue Crack Detection of Steel Structures Using Video Feature Tracking*. Computer - Aided Civil and Infrastructure Engineering, 2018. **33**(9): p. 783-799.
68. Kranjc, T., J. Slavič, and M. Boltežar, *The Mass Normalization of the Displacement and Strain Mode Shapes in a Strain Experimental Modal Analysis Using the Mass-Change Strategy*. Journal of Sound and Vibration, 2013. **332**(26): p. 6968-6981.
69. Lee, H.S., Y.H. Hong, and H.W. Park, *Design of an FIR Filter for the Displacement Reconstruction Using Measured Acceleration in Low-Frequency Dominant Structures*. International Journal for Numerical Methods in Engineering, 2010. **82**(4): p. 403-434.
70. Lee, J.J. and M. Shinozuka, *A Vision-Based System for Remote Sensing of Bridge Displacement*. Nondestructive Testing and Evaluation International, 2006. **39**(5): p. 425-431.

71. Lepage, A. *A Method for Drift-Control in Earthquake-Resistant Design of Rc Building Structures*. University of Illinois at Urbana-Champaign, 1997
72. Li, J. *Monitoring, Modeling, and Hybrid Simulation—an Integrated Bayesian-Based Approach to High-Fidelity Fragility Analysis*. University of Illinois at Urbana-Champaign, 2013
73. López-Aenlle, M., P. Fernández, R. Brincker, and A. Fernández-Canteli, *Erratum to “Scaling-Factor Estimation Using an Optimized Mass-Change Strategy”*[*Mech. Syst. Signal Process.* 24 (5)(2010) 1260–1273]. *Mechanical Systems and Signal Processing*, 2010. **24**(8): p. 3061-3074.
74. López Aenlle, M., R. Brincker, and A.C. Fernández Canteli, *Some Methods to Determine Scaled Mode Shapes in Natural Input Modal Analysis*. 2005.
75. Lucas, B.D. and T. Kanade, *An Iterative Image Registration Technique with an Application to Stereo Vision*. 1981.
76. Lynch, J.P., C.R. Farrar, and J.E. Michaels, *Structural Health Monitoring: Technological Advances to Practical Implementations [Scanning the Issue]*. *Proceedings of the IEEE*, 2016. **104**(8): p. 1508-1512.
77. Mayes, R., *Error Localization Using Mode Shapes: An Application to a Two Link Robot Arm*. 1991, Sandia National Labs., Albuquerque, NM (United States).
78. Moore, M., B.M. Phares, B. Graybeal, D. Rolander, G. Washer, and J. Wiss, *Reliability of Visual Inspection for Highway Bridges, Volume I*. 2001, Turner-Fairbank Highway Research Center.

79. Moreu, F., H. Jo, J. Li, R.E. Kim, S. Cho, A. Kimmle, S. Scola, H. Le, B. Spencer Jr, and J.M. LaFave, *Dynamic Assessment of Timber Railroad Bridges Using Displacements*. Journal of Bridge Engineering, 2015. **20**(10): p. 04014114.
80. Moschas, F., A. Avallone, V. Saltogianni, and S.C. Stiros, *Strong Motion Displacement Waveforms Using 10 - Hz Precise Point Positioning Gps: An Assessment Based on Free Oscillation Experiments*. Earthquake Engineering and Structural Dynamics, 2014. **43**(12): p. 1853-1866.
81. Moschas, F. and S. Stiros, *Measurement of the Dynamic Displacements and of the Modal Frequencies of a Short-Span Pedestrian Bridge Using Gps and an Accelerometer*. Engineering Structures, 2011. **33**(1): p. 10-17.
82. Nagayama, T. and B.F. Spencer Jr, *Structural Health Monitoring Using Smart Sensors*. 2007, Newmark Structural Engineering Laboratory. University of Illinois at Urbana
83. Nakamura, S.-i., *Gps Measurement of Wind-Induced Suspension Bridge Girder Displacements*. Journal of Structural Engineering, 2000. **126**(12): p. 1413-1419.
84. Ni, Y., Y. Xia, W. Liao, and J. Ko, *Technology Innovation in Developing the Structural Health Monitoring System for Guangzhou New Tv Tower*. Structural Control and Health Monitoring: The Official Journal of the International Association for Structural Control and Monitoring and of the European Association for the Control of Structures, 2009. **16**(1): p. 73-98.
85. Ojalvo, I. and D. Pilon. *Diagnostics for Geometrically Locating Structural Math Model Errors from Modal Test Data*. in 29th Structures, Structural Dynamics and Materials Conference. 1988. p. 2358.

86. Overschee, V.P. and D.B. Moor, *Subspace Identification for Linear Systems: Theory—Implementation—Applications*. 1996: Springer Science and Business Media.
87. Pandey, A. and M. Biswas, *Damage Detection in Structures Using Changes in Flexibility*. Journal of sound and vibration, 1994. **169**(1): p. 3-17.
88. Pandey, A., M. Biswas, and M. Samman, *Damage Detection from Changes in Curvature Mode Shapes*. Journal of sound and vibration, 1991. **145**(2): p. 321-332.
89. Pappa, R.S., K.B. Elliott, and A. Schenk, *Consistent-Mode Indicator for the Eigensystem Realization Algorithm*. Journal of Guidance, Control, and Dynamics, 1993. **16**(5): p. 852-858.
90. Park, J.W., S.H. Sim, and H.J. Jung, *Displacement Estimation Using Multimetric Data Fusion*. IEEE/ASME Transactions on Mechatronics, 2013. **18**(6): p. 1675-1682.
91. Park, K.-T., S.-H. Kim, H.-S. Park, and K.-W. Lee, *The Determination of Bridge Displacement Using Measured Acceleration*. Engineering Structures, 2005. **27**(3): p. 371-378.
92. Parloo, E., P. Verboven, P. Guillaume, and M. Van Overmeire, *Sensitivity-Based Operational Mode Shape Normalisation*. Mechanical systems and signal processing, 2002. **16**(5): p. 757-767.
93. Patsias, S. and W. Staszewskiy, *Damage Detection Using Optical Measurements and Wavelets*. Structural Health Monitoring, 2002. **1**(1): p. 5-22.
94. Peeters, B., *System Identification and Damage Detection in Civil Engineering*. 2000.
95. Philips Adewuyi, A., Z. Wu, and N. Kammrujaman Serker, *Assessment of Vibration-Based Damage Identification Methods Using Displacement and Distributed Strain Measurements*. Structural Health Monitoring, 2009. **8**(6): p. 443-461.

96. Pines, D. and A.E. Aktan, *Status of Structural Health Monitoring of Long - Span Bridges in the United States*. Progress in Structural Engineering and materials, 2002. **4**(4): p. 372-380.
97. Pisoni, A.C., C. Santolini, D.E. Hauf, and S. Dubowsky. *Displacements in a Vibrating Body by Strain Gage Measurements*. in Proceedings-SPIE the International Society for Optical Engineering. 1995. SPIE INTERNATIONAL SOCIETY FOR OPTICAL. p. 119-119.
98. Priestley, M., *Displacement-Based Seismic Assessment of Existing Reinforced Concrete Buildings*. Bulletin of the New Zealand Society for Earthquake Engineering, 1996. **29**(4): p. 256-272.
99. Ratcliffe, C.P., *Damage Detection Using a Modified Laplacian Operator on Mode Shape Data*. Journal of Sound and Vibration, 1997. **204**(3): p. 505-517.
100. Ruiz - García, J. and E. Miranda, *Residual Displacement Ratios for Assessment of Existing Structures*. Earthquake Engineering and Structural Dynamics, 2006. **35**(3): p. 315-336.
101. Rytter, A. *Vibrational Based Inspection of Civil Engineering Structures*. Dept. of Building Technology and Structural Engineering, Aalborg University, 1993
102. Salawu, O., *Detection of Structural Damage through Changes in Frequency: A Review*. Engineering structures, 1997. **19**(9): p. 718-723.
103. Shi, J. and C. Tomasi. *Good Features to Track*. In 1994 Proceedings of IEEE conference on computer vision and pattern recognition. 1994. IEEE. p. 593-600.
104. Shi, Z., S. Law, and L.M. Zhang, *Structural Damage Detection from Modal Strain Energy Change*. Journal of Engineering Mechanics, 2000. **126**(12): p. 1216-1223.

105. Simoncelli, E.P. and W.T. Freeman. *The Steerable Pyramid: A Flexible Architecture for Multi-Scale Derivative Computation*. in Proceedings., International Conference on Image Processing. 1995. IEEE. p. 444-447.
106. Siringoringo, D.M. and Y. Fujino, *Estimating Bridge Fundamental Frequency from Vibration Response of Instrumented Passing Vehicle: Analytical and Experimental Study*. Advances in Structural Engineering, 2012. **15**(3): p. 417-433.
107. Siringoringo, D.M. and Y. Fujino, *System Identification of Suspension Bridge from Ambient Vibration Response*. Engineering Structures, 2008. **30**(2): p. 462-477.
108. Skolnik, D.A. and J.W. Wallace, *Critical Assessment of Interstory Drift Measurements*. Journal of Structural Engineering, 2010. **136**(12): p. 1574-1584.
109. Smyth, A. and M. Wu, *Multi-Rate Kalman Filtering for the Data Fusion of Displacement and Acceleration Response Measurements in Dynamic System Monitoring*. Mechanical Systems and Signal Processing, 2007. **21**(2): p. 706-723.
110. Sohn, H., C.R. Farrar, F.M. Hemez, D.D. Shunk, D.W. Stinemates, B.R. Nadler, and J.J. Czarnecki, *A Review of Structural Health Monitoring Literature: 1996–2001*. Los Alamos National Laboratory, USA, 2003. **1**.
111. Solari, G. and P. De Gaetano, *Dynamic Response of Structures to Thunderstorm Outflows: Response Spectrum Technique Vs Time-Domain Analysis*. Engineering Structures, 2018. **176**: p. 188-207.
112. Spencer Jr, B.F., T. Nagayama, J.A. Rice, and G.A. Agha, *Smart Sensing Technology: A New Paradigm for Structural Health Monitoring*. Proc. 39th Joint Panel Meeting on Wind and Seismic Effects, UJNR, Tsukuba, Japan. , 2007.

113. Stephen, G., J. Brownjohn, and C. Taylor, *Measurements of Static and Dynamic Displacement from Visual Monitoring of the Humber Bridge*. Engineering Structures, 1993. **15**(3): p. 197-208.
114. Stone, J.V., *Blind Source Separation Using Temporal Predictability*. Neural computation, 2001. **13**(7): p. 1559-1574.
115. Su, Y., G. Huang, and Y.-l. Xu, *Derivation of Time-Varying Mean for Non-Stationary Downburst Winds*. Journal of Wind Engineering and Industrial Aerodynamics, 2015. **141**: p. 39-48.
116. Toksoy, T. and A. Aktan, *Bridge-Condition Assessment by Modal Flexibility*. Experimental Mechanics, 1994. **34**(3): p. 271-278.
117. Tomasi, C. and T. Kanade, *Detection and Tracking of Point Features*. School of Computer Science. 1991, Carnegie Mellon University. Pittsburgh.
118. Trifunac, M. and M. Todorovska, *A Note on the Useable Dynamic Range of Accelerographs Recording Translation*. Soil Dynamics and Earthquake Engineering, 2001. **21**(4): p. 275-286.
119. Trifunac, M.D., *Zero Baseline Correction of Strong-Motion Accelerograms*. Bulletin of the Seismological Society of America, 1971. **61**(5): p. 1201-1211.
120. Virant, M. and T. Dracos, *3d Ptv and Its Application on Lagrangian Motion*. Measurement Science and Technology, 1997. **8**(12): p. 1539.
121. Wadhwa, N., M. Rubinstein, F. Durand, and W.T. Freeman, *Phase-Based Video Motion Processing*. ACM Transactions on Graphics (TOG), 2013. **32**(4): p. 80.

122. Wahbeh, A.M., J.P. Caffrey, and S.F. Masri, *A Vision-Based Approach for the Direct Measurement of Displacements in Vibrating Systems*. Smart materials and structures, 2003. **12**(5): p. 785-794.
123. Wang, H., A. Li, and R. Hu, *Comparison of Ambient Vibration Response of the Runyang Suspension Bridge under Skew Winds with Time-Domain Numerical Predictions*. Journal of Bridge Engineering, 2010. **16**(4): p. 513-526.
124. Wang, Z.-C., D. Geng, W.-X. Ren, and H.-T. Liu, *Strain Modes Based Dynamic Displacement Estimation of Beam Structures with Strain Sensors*. Smart Materials and Structures, 2014. **23**(12): p. 125045.
125. West, W.M., *Illustration of the Use of Modal Assurance Criterion to Detect Structural Changes in an Orbiter Test Specimen*. 1986.
126. Wong, K.Y., *Instrumentation and Health Monitoring of Cable - Supported Bridges*. Structural control and health monitoring, 2004. **11**(2): p. 91-124.
127. Wu, H.-Y., M. Rubinstein, E. Shih, J. Gutttag, F. Durand, and W. Freeman, *Eulerian Video Magnification for Revealing Subtle Changes in the World*. 2012.
128. Yan, Y., L. Cheng, Z. Wu, and L. Yam, *Development in Vibration-Based Structural Damage Detection Technique*. Mechanical systems and signal processing, 2007. **21**(5): p. 2198-2211.
129. Yang, J., J.B. Li, and G. Lin, *A Simple Approach to Integration of Acceleration Data for Dynamic Soil–Structure Interaction Analysis*. Soil Dynamics and Earthquake Engineering, 2006. **26**(8): p. 725-734.
130. Yang, Y.-B., W.-F. Chen, H.-W. Yu, and C. Chan, *Experimental Study of a Hand-Drawn Cart for Measuring the Bridge Frequencies*. Engineering Structures, 2013. **57**: p. 222-231.

131. Yang, Y.-B., C. Lin, and J. Yau, *Extracting Bridge Frequencies from the Dynamic Response of a Passing Vehicle*. Journal of Sound and Vibration, 2004. **272**(3-5): p. 471-493.
132. Yang, Y.-B., J. Yau, Z. Yao, and Y. Wu, *Vehicle-Bridge Interaction Dynamics: With Applications to High-Speed Railways*. 2004: World Scientific.
133. Yang, Y., C. Dorn, T. Mancini, Z. Talken, G. Kenyon, C. Farrar, and D. Mascareñas, *Blind Identification of Full-Field Vibration Modes from Video Measurements with Phase-Based Video Motion Magnification*. Mechanical Systems and Signal Processing, 2017. **85**: p. 567-590.
134. Yang, Y. and C. Lin, *Vehicle–Bridge Interaction Dynamics and Potential Applications*. Journal of sound and vibration, 2005. **284**(1-2): p. 205-226.
135. Zhang, Q., B. Yang, T. Liu, H. Li, and J. Lv, *Structural Health Monitoring of Shanghai Tower Considering Time-Dependent Effects*. Int J High Rise Build, 2015. **4**(1): p. 39-44.
136. Zhao, X., H. Liu, Y. Yu, X. Xu, W. Hu, M. Li, and J. Ou, *Bridge Displacement Monitoring Method Based on Laser Projection-Sensing Technology*. Sensors, 2015. **15**(4): p. 8444-8463.